Aalto University & Luleå University of Technology

Magnetic Moment Characterization for Small Satellites

Alejandro Sans Monguiló

School of Electrical Engineering

Thesis submitted for examination for the degree of Master of Science in Technology.
Otaniemi, Espoo 27.9.2021

Supervisor

Prof. Jaan Praks (Aalto University)
Prof. René Laufer (Luleå University of Technology)

Advisor

Dr. Bagus Adiwiluhung Riwanto

Aalto University
School of Electrical Engineering

Aalto University
School of Electrical Engineering

Aalto University, P.O. BOX 11000, 00076 AALTO
www.aalto.fi
Abstract of the master's thesis

Author Alejandro Sans Monguiló

Title Magnetic Moment Characterization for Small Satellites

Degree programme Space Science and Technology

Major Space Robotics and Automation **Code of major** ELEC3047

Supervisor Prof. Jaan Praks (Aalto University)
Prof. René Laufer (Luleå University of Technology)

Advisor Dr. Bagus Adiwiluhung Riwanto

Date 27.9.2021 **Number of pages** 91 **Language** English

Abstract

Small satellites are gaining popularity in a wide range of applications where attitude systems require high precision performance. One of the main sources of errors, in case of magnetic attitude control systems, is the residual magnetic moment (RMM) of the spacecraft. To keep the RMM low and stable, mitigation methods shall be applied based on the satellite's magnetic dipole moment (MDM) characterization, which shall be measured accurately. For small satellites, the most common technique involves the generation of a field-free region for the magnetic measurements using a test bed. The test bed measurement setup is normally mechanical, where measurements from the device under test (DUT) are very tedious. Optical magnetic test beds (OMTB) are being developed for MDM characterization providing simpler set ups and faster measurements than mechanical test beds.

In this work, accuracy of OMTB of Aalto University has been evaluated by measuring three permanent magnets in two configurations. The measurements show a relationship between the estimation accuracy and the DUT's marker area seen by the camera. Moreover, it was observed that the field-free region generated by Helmholtz coil cage can generate false data points. Based on these observations, the detection of the marker's positions have been evaluated using the view area (VA) and the pointing angle (PA). The analysis shows that there is a consistent pattern depending on the combination of the VA and PA. Hence, the method of data acquisition was improved in order to prioritize the markers which position allow better accuracy. The achieved improvement of MDM estimation results is 2 %, and the test bed's overall error evaluated is a 13 % in MDM position estimation and 23 % in MDM magnitude estimation. The improved OMTB was used to characterize the MDM of four magnetic attitude coils of Foresail-1 satellite. The measurements results are consistent with design parameters, showing three dipole configuration in all coils with a MDM magnitude order of 10^{-2} A $\cdot$ m^2.

Keywords small satellite, CubeSat, optical magnetic test bed, magnetic dipole moment characterization, residual magnetic moment, permanent magnet verification, magnetic measurement, Foresail-1, Helmholtz cage

Preface

I would like to thank all the people that help me becoming the person I am today. I want to thank Jaan Praks for his supervision and guidance of this thesis, and to Bagus A. Riwanto for his patience and help in the laboratory. Also, to Pasi Ylä-Oijala who reviewed my work and gave a helpful point of view.

Moreover, I would like to thank my friends here in Finland, for being there when I needed it, and in general to my friends in the SpaceMaster round 15, for the great times. Lastly, to my family who has been always supportive. Specially to my dad, who would have felt proud and liked to be my side this day.

Thank you all,

Otaniemi, 27.9.2021

Alejandro Sans Monguiló

Contents

List of Figures

List of Tables

List of Algorithms

Abbreviations and acronyms

ADCS	attitude, determination and control system
DUT	device under test
ENA	energetic neutral atom
EPS	electrical power system
EQM	engineering qualification model
FOV	field of view
MDM	magnetic dipole moment
MF	magnetic field
NI	national instruments
LVLH	local-vertical/local-horizontal
OBC	on-board computer
OMTB	optical magnetic test bed
PA	pointing angle
PATE	particle telescope
PB	plasma brake
PLA	polylactic acid
PSO	particle swarm optimization
RMM	residual magnetic moment
S/C	spacecraft
VA	view area

Symbols

Latin letters

A	camera visual's area
a	marker's area
A_{px}	camera visual's area in pixels
a_{px}	marker's area in pixels
$\mathbf{A}$	direction cosine matrix
$\mathbf{A_n}$	rotation matrix in the orthogonal axis corresponding to "n"
B	magnetic field flux density
B_r	residual flux density
FOV_h	horizontal angle field of view of the camera
FOV_v	vertical angle field of view of the camera
m	magnetic dipole moment
m_X	magnetic dipole moment of magnet "X"
PA_h	pointing angle from the horizontal plane
PA_v	pointing angle from the vertical plane
$\mathring{\mathrm{q}}$	unit quaternion
s	scalar
T_m	magnetic torque
V_x	volume of "x"
v	vector v
v_n	component "n" of vector v
VA_{px}	view area measured from areas in pixels
w	calculated weighting value

Greek letters

α	angle axis rotation of the unit vector of rotation
θ	roll angle
μ_0	magnetic permeability
π	number pi
Φ	rotation in the orthogonal axis
ϕ	pitch angle
ψ	yaw angle

Others

$A \cdot B$	dot product of vectors A and B
$A \times B$	cross product of vectors A and B
$\|\|v\|\|$	module of vector v
$\hat{\text{v}}$	unit vector v

1 Introduction

1.1 Overview

Over the last decade, the number of applications for small satellites, nano-satellites like CubeSats, has increased exponentially from Earth Observation (EO) to assistance in deep-space missions in the Solar System, mainly due to their lower cost and quicker development [1].

In order for the spacecraft (S/C) to meet its mission objectives, among other important subsystems, the attitude, determination and control subsystem (ADCS) provides and controls the satellite's pointing and accuracy; thus, its orientation. To determine the orientation, ADCS is composed by several sensors like gyroscopes, magnetometers, sun sensors, among other types; which will then dictate ACDS actuators' manipulation such as magnetic torques, reaction wheels, etc [2]. In case of small satellites like CubeSats, it is difficult to accomplish high-precision pointing and stability due to disturbance torques caused by the S/C's residual magnetic moment (RMM). The characterization of the satellite's RMM is really important when designing the subsystems and their material in order to minimize the effect on the S/C and its functions [3].

Therefore, the characterization of the magnetic dipole moment (MDM) for satellites should be considered in order to mitigate the disturbance due to the RMM [4]. The MDM can be determined using several methods depending on the satellite's or subsystem's dimensions, magnetic environment, etc.; some of them can be found in the appendix B of [5]. Most of the techniques used for the MDM estimation involve a mechanical magnetic test bed in which the device under test (DUT) is rotating in one or more axes and surrounded relative to one or several magnetometers, normally inside of a magnetically neutral field. There are several studies using these techniques, or similar ones [3] [6] [7] [8] [9] [10] [11]. Other methods for MDM analysis can be found in [12] [13]. Moreover, new technology is being developed using optical systems. This new technology incorporates a visual system for MDM measurements which test bed, in this work, is referred as an optical magnetic test bed (OMTB). Some studies in this field can be found in [14] and [2], for instance.

In the case of small satellites, mechanical and optical test beds are suitable to characterize its magnetic dipoles. However, mechanical test beds normally involve complex mechanical systems in functionality, design or dimensions. Apart from this added complexity, the position of the DUT and the magnetometers must be known at all moments, which can be tedious even if the process is automated.

On the other hand, it is worthy to point out that OMTBs do not require such a complex system and are easier to set up and measure since the relative pose of the DUT and the magnetometer is not needed at all times due to their machine-vision detection. Thanks to this, the measurement is easier to implement and can take less than an hour to complete. Note that for both test beds a neutral magnetic field (MF) environment is required [3] [14].

This thesis focuses on the machine-vision-assisted magnetic test bed, or OMTB, of Aalto University, validating the novel system for magnetic cleanliness analysis

by measuring components of the Foresail-1 satellite. Thus, it is worth introducing Foresail-1 satellite mission purposes and general overview. Foresail-1 mission consists of a 3-Unit (3U) CubeSat with two scientific and one technological goals. The technological goal demonstrates a de-orbiting technology for a non-propellant small satellite. Regarding the two scientific goals, one of them focuses on measuring solar energetic neutral atoms (ENAs), and the second goal, on measuring the energy and flux dependent pitch angle spectra of precipitating radiation belt particles. For the mission to be successful, Foresail-1's payload includes a PArticle TElescope (PATE) and a Plasma Brake (PB). Among other subsystems in the S/C's platform, the avionics stack comprises the Electrical Power System (EPS), On-Board Computer (OBC) and ADCS. The payloads and subsystems, fitted in a standard 3U CubeSat structure, can be seen in Figure 1 [15].

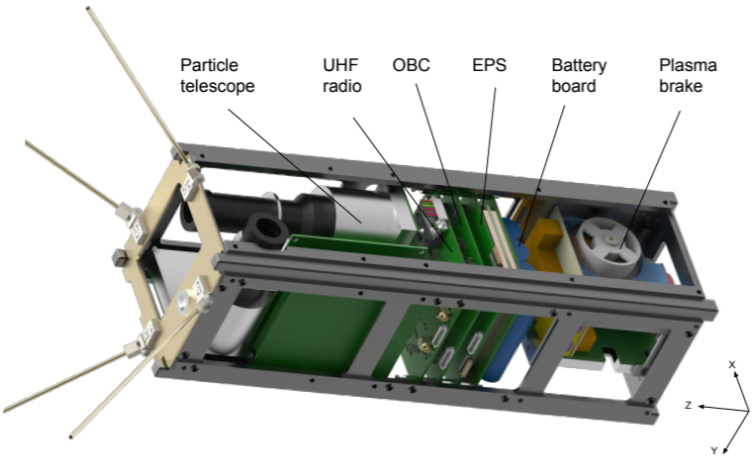

Figure 1: Foresail-1's structure without shielding and subsystem location [15]

1.2 Scope and structure

As it has been stated earlier, the scope of the thesis comprises the determination of the accuracy of the OMTB at Aalto University, including test bed's improvement in performance, and identification of the MDM of Foresail-1 satellite's components. Hence, the goal of the thesis is to assess the accuracy and error of the machine-vision-assisted test bed setup for S/C magnetic characterization and possible further improvement, in order to characterize the MDM of the components of small satellites; Foresail-1 in this case.

In order to achieve the above mentioned goal, the thesis is structured as follows. Firstly, Section 1 introduces the thesis' topic and briefly the Foresail-1 mission, including the organisation of this thesis. Section 2 explains the current MDM background and the basic theory needed for this thesis. Followed by Section 3 which presents the above mentioned OMTB setup, including physical and software components as well as the measurement's procedure. Section 4 introduces the limiting

factors of the OMTB and measurements of three permanent magnets, including the creation of new variables needed for the analysis. Then, Section 5 presents an error analysis based on the previous measurements and the modification of the data acquisition of the test bed based on that analysis. In Section 6, new measurements are performed using the modified system, results of the comparison between the previous and new three-magnet measurements as well as Foresail-1 components' measurements are provided and evaluated. Lastly, Section 7 concludes the thesis with a final evaluation based on the information provided in the thesis, followed by the bibliography section.

2 Magnetic dipole measurement

In order to determine the magnetic accuracy of the setup and further evaluation of the MDM, it is important to understand some key theoretical concepts. Therefore, this chapter introduces the topics needed to understand the work presented in this thesis. This includes the theoretical concepts and methods used for characterizing the magnetic moment of a S/C. This chapter is structured as follows. Section 2.1 introduces key concepts related to attitude representation. Then, Section 2.2 presents how optical recognition works, including some applications and definitions. In Section 2.3, the term CubeSat and the subsystem in charge of the attitude of the S/C are explained. Section 2.4 and Section 2.5 are related to the MDM, the magnetic torque is introduced in the first one, while the techniques for the MDM characterization are presented in the second one.

2.1 Attitude representation

In order to get a reference on how the attitude of an object is represented, this section presents and defines key concepts which will be used throughout the thesis work.

Firstly, pose is defined as the combination of position, the location of the object in space, and orientation, or attitude. A vector can be defined as a single number (scalar) with a direction, which can be described in terms of its components based on the coordinate system. A coordinate frame, or a Cartesian coordinate system, is represented by orthogonal axes which intersect at the origin (normally represented as x, y and z axes). As stated above, a vector can be represented by unit vectors parallel to the axes of the frame [19]. Figure 2 displays different coordinate systems, from left to right: geocentric-equatorial, Local-Vertical/Local-Horizontal (LVLH) orbit and body frames [20]. The attitude of a satellite relative to the inertial reference frame (geocentric-equatorial system in Figure 2) can be specified with the direction cosine matrix, $\mathbf{A}$. This matrix is described using three vectors for each axis (x, y, and z) with three components each vector, as seen in Equation 1. This matrix can be used to describe a vector of the body coordinate frame into the inertial reference frame and it can be obtained using the expression $\mathbf{A} = \mathbf{A_2}\mathbf{A_1}\mathbf{A_3}$. The matrix multiplication order must be from right to left, a 3-1-2 rotation. Matrices $\mathbf{A_3}$, $\mathbf{A_1}$, and $\mathbf{A_2}$ are expressed in Equation 2, Equation 3, and Equation 4 [21], where a rotation of Φ is performed in each orthogonal axis.

$$\mathbf{A} = \begin{bmatrix} x_1 & x_2 & x_3 \\ y_1 & y_2 & y_3 \\ z_1 & z_2 & z_3 \end{bmatrix} \quad (1) \qquad \mathbf{A_3} = \begin{bmatrix} cos\Phi & sin\Phi & 0 \\ -sin\Phi & cos\Phi & 0 \\ 0 & 0 & 1 \end{bmatrix} \quad (2)$$

$$\mathbf{A_1} = \begin{bmatrix} 1 & 0 & 0 \\ 0 & cos\Phi & sin\Phi \\ 0 & -sin\Phi & cos\Phi \end{bmatrix} \quad (3) \qquad \mathbf{A_2} = \begin{bmatrix} cos\Phi & 0 & -sin\Phi \\ 0 & 1 & 0 \\ sin\Phi & 0 & cos\Phi \end{bmatrix} \quad (4)$$

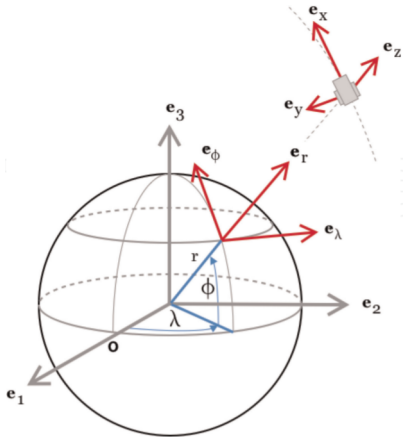

Figure 2: From left to right: geocentric-equatorial, LVLH-orbit and body frames [21]

In this brief introduction to the topic, two attitude representations are explained, quaternion vectors and Euler angles representations. Other representations can be found in [20].

Quaternion representation

A quaternion is defined as a hypercomplex number, an extension of a complex number, and it is represented by a scalar (s) plus a vector (v) as [19]

$$\mathrm{q} = s + v = s + v_1 i + v_2 j + v_3\, k, \tag{5}$$

which can be denoted as $\mathrm{q} = s < v_1, v_2, v_3 >$. Note that i, j, and k represent the unit vectors for each of the orthogonal axes, x, y, and z axes, respectively. For rotations, unit-quaternions can be considered as a rotation of α around the unit vector $\hat{\mathrm{v}}$. A unit-quaternion can be denoted by $\mathring{\mathrm{q}}$ which module is equal to one: $\mathring{\mathrm{q}} = ||\mathrm{q}|| = s^2 + v_1^2 + v_2^2 + v_3^2 = 1$. Rotations are related to unit-quaternions as $\mathring{\mathrm{q}} = cos\frac{\alpha}{2} < \hat{\mathrm{v}}\ sin\frac{\alpha}{2} >$, which is similar to the axis angle representation. More information can be found in [19]. The direction cosine matrix can be written in terms of quaternions as shown in Equation 6 [21]. Quaternion representation is normally preferred, since it solves some of the singularities and difficulties other representations have, like the Euler angles representation.

$$\mathbf{A} = \begin{bmatrix} v_1^2 - v_2^2 - v_3^2 + s^2 & 2(v_1 v_2 + v_3 s) & 2(v_1 v_3 - v_2 s) \\ 2(v_1 v_2 - v_3 s) & -v_1^2 + v_2^2 - v_3^2 + s^2 & 2(v_2 v_3 + v_1 s) \\ 2(v_1 v_3 + v_2 s) & 2(v_2 v_3 - v_1 s) & -v_1^2 - v_2^2 + v_3^2 + s^2 \end{bmatrix} \tag{6}$$

Euler angles representation

Another way of representing the attitude of an object, a satellite for instance, is by using Euler angles. This representation is based on three rotations on each of the three axes, instead of the earlier mentioned single axis rotation representation. These Euler angles, or rotations, are also known as pitch, yaw and roll rotations in x, y and

z axes, respectively. These rotations can be denoted as ψ for pitch, ϕ for yaw, and θ for roll. It is important to point out that the final rotated frame depends on the order of the rotations, as illustrated in Figure 3. Hence, the sequence of the rotations must be clear for a specific representation. For instance, if the order of rotation is 3-1-2: first in the z axis, then the x axis and finally the y axis, the direction cosine matrix can be written as shown in Equation 7 [21].

$$\mathbf{A} = \begin{bmatrix} cos\psi cos\phi - sin\theta sin\psi sin\phi & cos\psi sin\phi + sin\theta sin\psi cos\phi & -cos\theta sin\psi \\ -cos\theta sin\phi & cos\theta cos\phi & sin\theta \\ sin\psi cos\phi + sin\theta cos\psi sin\phi & sin\psi sin\phi - sin\theta cos\psi cos\phi & cos\theta cos\psi \end{bmatrix} \tag{7}$$

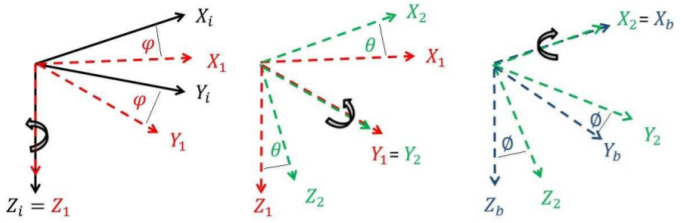

Figure 3: Euler angles sequence rotation, 3-1-2 [22]

Note that the software used in the magnetic measurements of this thesis uses both quaternions and three-axis rotations representations when estimating the MDM. In the analysis of Section 5.1, Euler angles are used to describe the orientation of the markers.

2.2 Optical recognition

In order to detect the pose of the DUT, markers are detected using computer vision. Optical recognition can be considered as the determination of a certain pattern or data from an image that is obtained from an artificial visual system. Based on *Perry West* [23], *machine vision* is defined as "the automated collection and analysis of images to acquire the wanted data for use in controlling a process or an activity". From this definition, the *images* are processed by a computer, thus they are always digitized first. In other words, the visual image becomes a matrix of pixels. In case of a grey-scale image, each pixel gives information only about the quantity of light, as shown in Figure 4, whereas in case of a 3D images also information of the distance is collected [24] [25]. Then, in order to analyse this information, the processor compares the previously established models of the observed world with the information given by the image [25].

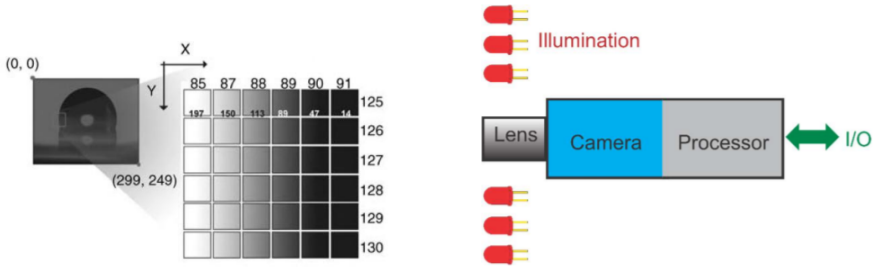

(a) (b)

Figure 4: Grey-scale image [24] (a), and smart camera configuration [23] (b)

The *collection and analysis* concepts from the definition of machine vision are related on how the images are taken and how the post-process is done in order to obtain the desired data from the picture. To take the images, different configurations of vision systems are available, mostly involving a camera and a processor [23]. When the camera and processor are combined, as displayed in Figure 4, the configuration is known as a smart camera. Regarding the analysis of desired data, as above mentioned, some previously known features are compared with the picture's information [26].

Machine vision can be used for different functions such as gauging, tracking, recognition, verification, etc. In this thesis, the OMTB involves the function of recognition which can be defined as the determination of an object's identity by its characteristics, e.g. size, shape, etc. For a proper recognition, noise ratio, dynamic range, contrast, etc. and some other details from the picture are important. Besides, camera's lens and sensors would also play a key role for a better data acquisition and recognition [23].

2.3 CubeSats and ADCS

In the last decades, CubeSats have become more and more popular in several applications such as science missions and testing of technologies like those regarding astronomy or space weather objectives, mostly by educational institutions [1]. Satellites can be classified based on their application, weight and dimensions. Based on their mass, small satellites weight approximately up to 300 kg [27]. Inside this category, nanosatellites range from 1 to 10 kg, and CubeSats fall in this subcategory. The designation of CubeSat is used for a specific type of nanosatellites. A standard CubeSat "unit", or 1U, is a 10x10x10 cm cube that weights around 1 kg. These units can form larger sizes of CubeSats like 2U, 3U and 6U. Thanks to the standardization of their weight and dimensions, the cost of developing a CubeSat can be considered low compared to other types of satellites [1] [27].

Once in orbit, there are several types of disturbances that can affect the satellite's attitude like gravity gradient torque, shape of the Earth, solar radiation pressure, magnetic disturbance torques, etc. The ADCS is in charge of determining and controlling the orientation of the S/C to reach the space mission goals. To control the satellite, ADCS is equipped with sensors and actuators. Examples of the used sensors include sun sensors, magnetometers, star-trackers, and earth sensors. The

function of the sensors is to keep track where and in which orientation the S/C is, so that the attitude can be corrected if needed. Some examples of the used actuators in a ADCS are magnetorquers, momentum wheels, reaction wheels, or thrusters. More details of the ADCS can be found in [28].

2.4 Magnetic torque

Magnetic torques can cause disturbances when a satellite is orbiting. The three main sources of magnetic torque disturbances are the S/C magnetic moment, Eddy currents and the hysteresis. The last two can be considered negligible if the magnetic design of the satellite's material, construction, subsystems is clean. Thus, the RMM is considered the main source of magnetic disturbance [28]. Taking into account the RMM, which is the residual S/C's dipole moment, the total torque can be expressed as

$$T_m = m \times B, \tag{8}$$

where the magnetic torque, T_m, is generated by the dipole moment of the satellite, m in $\mathrm{A} \cdot \mathrm{m}^2$, and the magnetic field of the object's environment, B in Tesla. In order to reduce this disturbance, the RMM shall be mitigated by calculating the MDM of the S/C. This thesis focuses on the calculation of the MDM, in other words, on the magnetic characterization of the DUT.

2.5 Magnetic characterization techniques

As stated above, the RMM compensation increases the accuracy in the orientation and pointing of the S/C. The MDM shall be estimated properly in order to cancel the magnetic torque disturbance [4]. Therefore, magnetic cleanliness analysis of the satellite is useful to reach a low and stable RMM [7]. Magnetic cleanliness programs usually involve how the S/C is designed in order to avoid any undesirable magnetic torque produced by the materials, construction, etc. which can generate other local MFs [3]. As stated above, in order to maintain a tolerable RMM and be able to mitigate it, the MDM characterization should be measured accurately. Different techniques for MDM analysis are presented in [5], and briefly in [29]. These techniques include:

1 Direct torque measurements, using coilless systems

2 Direct torque measurements, in a controlled field

3 Pulse resonance technique

4 Ambient field mapping

5 Mapping inside a field-free region

The description and explanation of the first four methods can be found in [5]. This thesis focuses on the MDM measurements using the fifth method, which has been commonly used for magnetic characterization of satellites. The required field-free region is produced by a 3-axis Helmholtz cage in this thesis. For large satellites, the production of a large enough zero-MF environment for the measurement is expensive and difficult. Therefore, smaller subsystems and parts of the large S/C can be measured instead. In the case of small satellites, this method is commonly used since a smaller field-free region for small subsystems, or CubeSats, is more feasible to generate with a less-complex system [5].

Using mapping in a zero-MF region for small satellites or components, a 3-axis Helmholtz cage is normally used for creating the field-free region required. The process of the measurement or mapping varies depending on how the readings are taken. This method can be used in a mechanical magnetic measurement, where the DUT is rotated in one or more axis surrounded by one or several magnetometers, as illustrated in Figure 5. For each new pose of the DUT, the relative pose between the DUT and the magnetometer(s) must be known during the entire measurement. Since the measurement has to consider all relative poses of the DUT and magnetometer(s), it can be tedious if the process is not automated. Note that the automation of this process might involve a costly and complex system to rotate the DUT. Depending on the application, the equipment needed might differ from one mechanical test bed to another [30] [3] [8].

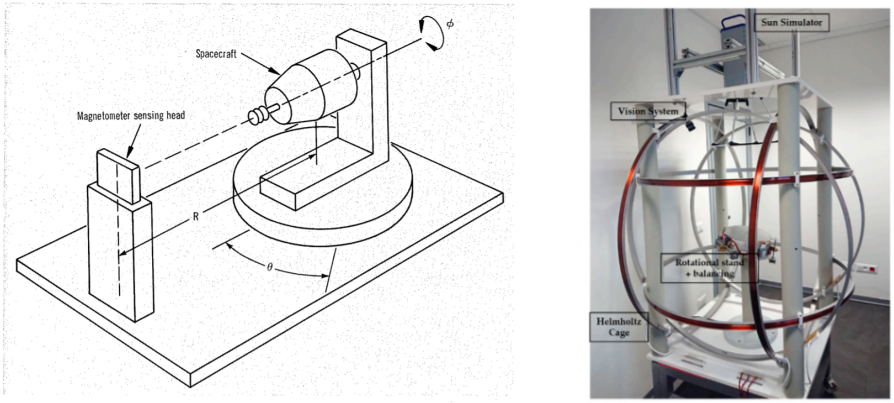

(a) Mechanical test bed [5] (b) Optical test bed [14]

Figure 5: Magnetic test beds for MDM characterization of satellites

Another way of taking the measurements which is applied recently is using machine vision placed in the optical test bed, as it can be seen in Figure 5. This technique is used in OMTBs in which a vision system is recognising the poses of the DUT and magnetometer(s) by recognising optical patterns placed on them. The visual recognition system algorithm can vary depending on the pattern or system used to recognize the object(s); markers with a determine pattern can be used, for example. This approach does not involve complex equipment, the DUT can be placed in an air-bearing platform and the magnetometer(s) in a fixed position. More details about this technique using optical test beds can be found in [2] [14].

3 Description of the optical magnetic test bed

In this section, the OMTB set up is presented and described for each of its components, as well as the procedure involved in taking a measurement using the machine-vision-assisted test bed at Aalto University. This information is needed in order to have a good understanding on what is the system composed of and how the measurements are carried out. Regarding the organisation of this section, Sections 3.1 and 3.2 present an overview the whole system and components of the OMTB, including the software needed for the magnetic measurements. Section 3.3 describes how the measurements are taken, explaining each step needed.

3.1 Physical setup

Regarding the physical test setup, all components considered are listed below. All of them have a role within the system, these roles are explained in the following lines for each of the components. The OMTB setup consists of:

1 3-axis Helmholtz coils cage

2 Magnetometer

3 DUT

4 ArUco markers

5 Camera and support

6 Background isolation paper

7 Control software

The Helmholtz coils is configured with three pairs of coils in Helmholtz configuration, that is a three-axis Helmholtz coil cage. This configuration is named after Hermann von Helmholtz, a German physicist. The device is used to create an approximate uniform MF in between the pair of coils, when a current is flowing in the same direction in each coil [16]. The coils in this setup are used to generate a MF which cancels Earth's MF in all three axes. This is done to create a nearly zero MF inside the coils, in the order of tens of nano-Tesla (nT), and be able to measure residual magnetic properties of the DUT.

This device is controlled via the Helmholtz coil control software from Bartington Instruments. For this purpose, other components connect the magnetometer and the coils are used: a CU1 Helmholtz coil system control unit, a PA1 power amplifier and, sometimes, a CU2 closed loop module with a sensor. This last component is used to cancel the MF inside the coils in an easier and faster way than manually. However, CU2 module is canceling the field in the order of tens to hundreds of nT depending on the axis for this OMTB setup. Hence, a better cancellation can be reached manually, which is explained in Section 4.

The magnetometer used for the measurements is a three-axis MF sensor from Bartington Instruments, Mag-13, which provides high precision measurements of alternating and static MFs. More details of the sensor are given in [17]. The device is fixed inside the Helmholtz coils in a central wooden platform which places the magnetometer within the camera's field of view (FOV). The readings from the magnetometer will be processed by a MATLAB script which plots the measured MF in the DUT coordinate frame.

The DUT refers to the component that is being tested with the setup. The output of the system provides the magnetic properties data of the DUT, so it can be processed for its MDM analysis. The DUTs can vary in shape and weight, and different DUTs will be presented in the following sections. Following the components list, the ArUco markers are placed in both the magnetometer and the DUT, where the number and location differ for one DUT to another depending on the DUT's geometry. Each of the markers placed on the DUT has its own pattern so it can be distinguished perfectly from each other. The markers are provided by the official website [18] [32], and they all shall have the same dimensions for the magnetic measurement.

Related to the detection of the markers, the camera used is a Jevois - A33 smart video camera [18], which detects any visible ArUco markers inside its FOV. It also extracts the orientation of each marker based on instructions given by the script to be explained in Section 3.2. The video camera is fixed in a tripod to measure steadily and to regulate the angle, distance and height. A small DUT can make some of the magnetic measurements easier to perform: the camera might not need the support since it can be held with one hand and the DUT can be rotated with the other one.

Lastly, the background isolation paper prevents the external environment to confuse camera's detection. In some cases, the camera can detect combinations of objects or shadows as ArUco markers although these markers do not exist. In this way, the interference with the physical ambient is minimized so the camera is perfectly able to detect and extract the correct information from the markers defined in the MATLAB script [32].

The following figure shows a general overview of the setup's configuration. In Figure 6, the camera is fixed in a long configuration and it is explained in Section 4. All measurements in this thesis have been performed with the camera fixed in one of the configurations introduced in Section 4.

3.2 Data-processing software and programs

In this section, the software and programs used to take the measurements with the above setup are presented. The main data-processing software is MATLAB which different scripts and functions take, process and analyse the information from the raw data given by the camera and the magnetometer.

Therefore, several MATLAB scripts are used in order to get all the needed information. One of these scripts takes the main measurement, the second one removes the ambient MF from the magnetometer and the third one estimates the position and magnetic properties of the measured data. It is worthy to point out

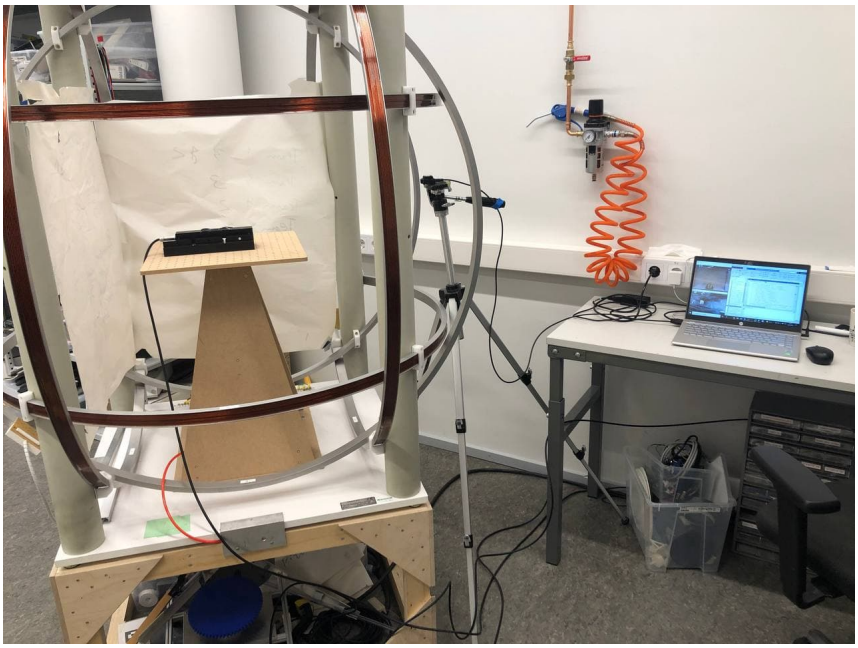

Figure 6: OMTB setup for MDM measurements

that all of these scripts use specifically created functions to plot the magnetic dipole vectors' position and characteristics, for example, or to use heuristics for different applications such as fusing several marker data. The details of the modifications of some algorithms and scripts for the purposes of this thesis will be given in the following sections. More details on the creation, function and application of these scripts and algorithms can be found in Bagus Riwanto's work [2].

For Mag-13 to be controlled, Bartington Software is used, as illustrated in Figure 7 and Figure 8. Bartington screens display several options for using the magnetometer which is connected to the computer through the National Instruments (NI) components described in Section 3.1.

In Figure 7, once the type of magnetometer is chosen (BH1300-3-C in our case) from the up-right corner display, the three values underneath need to be tuned for each axis which are multiplied by the first most left value, 0.1 in this case. Also, the DUT "PSU" value, shown in Figure 7, should be between 12 - 17 V. In this thesis, 15 V has been selected for all the measurements, and using a DC signal the x, y, and z axes have been turned on from the signal and output option columns, as illustrated in Figure 7. The values shown in Figure 8 correspond with the readings from the magnetometer for each axis. These values are chosen to be displayed in Tesla.

For taking the information and video feed from the camera, AMCam is the software used to display the camera vision in order to crosscheck and be able to detect the markers' position within its range of view; this can be seen in Figure 9. Meanwhile, another software program, called VC-software, splits the physical port connecting the camera and the computer into two virtual ports. This way AMCam and the MATLAB script can use the data from the camera at the same time.

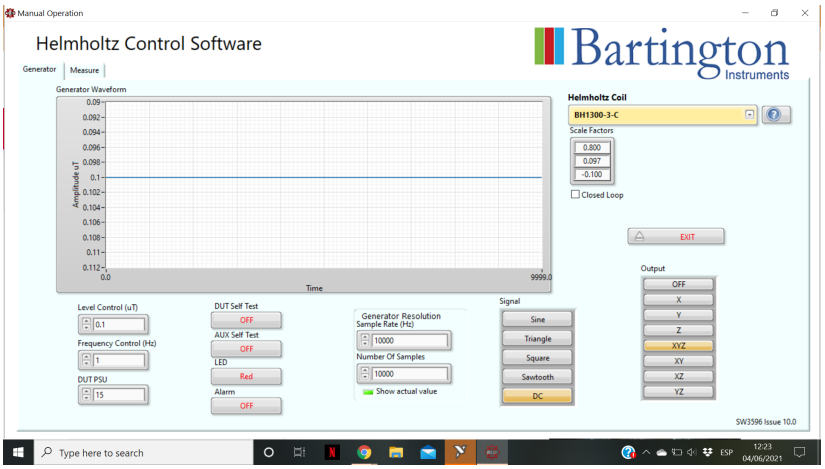

Figure 7: Bartington software - homepage I

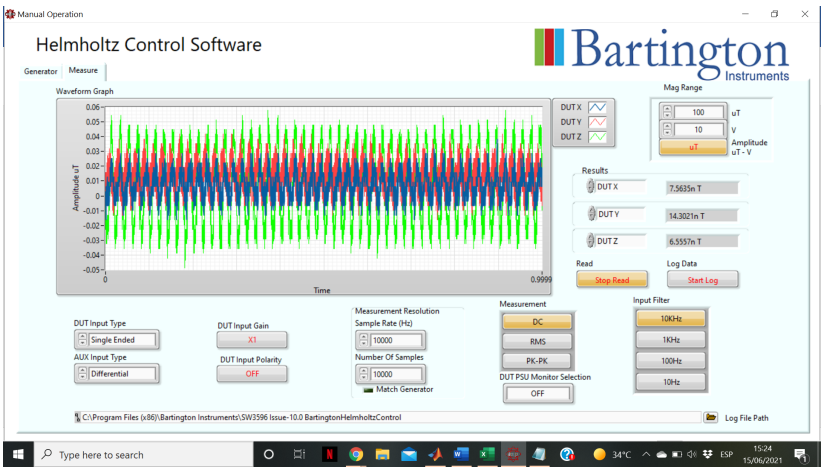

Figure 8: Bartington software - homepage II

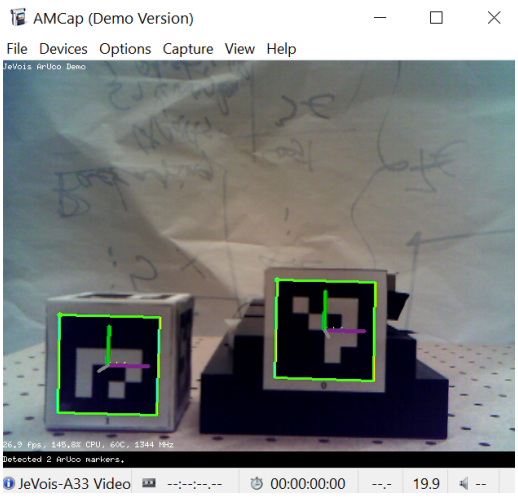

Figure 9: Video feed using AMCap, DUT on the left and magnetometer on the right

3.3 Magnetic measurement workflow

In this section, the process of taking a measurement is described in order to have a general overview of how the whole procedure is performed. Thus, the general steps are explained and the following order:

1 Preparation of the DUT and camera, and turning on the Helmholtz coils

2 Cancellation of the MF inside the Helmholtz coil cage

3 Take notes of the current MF environment before measuring

4 Take the actual measurement using the DUT

5 Take notes of the current MF environment after measuring

6 Preparation data and values for post-processing

7 Removing the ambient MF

8 Estimation of the MDM's position and magnitude

9 Analysis of the results and follow-up

Firstly, the Helmholtz coils' PA1 Power Amplifier is turned on to be warmed up for the measurement, which takes around 15 minutes. Meanwhile, the DUT and camera has to be prepared for the measurement. The camera is fixed with a tripod in an specific place for a burst of collecting data, its position normally does not change during the whole measurement. However, the camera's position can change if a better detection is required. When preparing the DUT, this normally involves placing the DUT in a structure which supports the device and have visible markers on the surface. For verifying the OMTB, a 50-mm polylactic acid (PLA) cube is used as the structure for three permanent magnets placed carefully underneath one of the total six markers. For further magnetic tests, the DUT can be a chosen component(s) inside of a harness with the markers. Any extra information needed for the measurement is also registered for a later use, such as: position, properties, input current or other observations about the measurement. Before starting the next steps, the magnetometer is fixed in a wooden structure inside the coils and the markers' pose is checked.

Secondly, Earth's MF and other disturbances need to be cancelled inside the coils. In order to do this, several values for each axis are tested using the Bartington Control software where the readings using those values should be in the order of tens of nT. This tuning process considers three values in order to obtain a near-null MF that is crucial for a correct measurement for each axis. Since the final data is estimating magnetic properties, they can be altered considerably if the MF is not properly cancelled. Note that the DUT is placed outside the coils where it does not disturb the ambient MF and the tuning process.

After tuning, the current reading from Bartington software shall be noted for the further analysis of the measurement. Since the MF will never be exactly zero,

these non-zero values will be used to remove the ambient MF from the final data and to check if this MF has changed after the measurement; a screenshot and use of the values in MATLAB is used for this step. Bartington Software shall stop the readings at this moment, so the MATLAB measuring script can collect and use the magnetometer's readings.

In the fourth step, the measurement is performed by running the MATLAB script which collects the data from both the camera and the magnetometer. The camera is detecting the markers of the magnetometer and the DUT in several positions and distances. The magnetometer is fixed and the DUT is rotated and moved slowly around the magnetometer and inside the FOV of the camera. Data points are taken, usually between 500 and 1000 measured points, until most or all area is covered with readings. MATLAB script is plotting the MF vector and position while taking the readings, so that preferred positions or areas that are not covered can be spotted easily and adapt the DUT pose if needed. When the measuring script is finished and all the wanted poses are measured, the MATLAB work space is saved for future analysis and the DUT is placed in its original position where it does not perturb the ambient MF.

Then, the ambient MF after the measurement is noted from the Bartington software as it was done before the measurement. All the values will be used in a MATLAB script which will remove the ambient MF of the measurement. At this moment, the variation in the MF before and after the test can be seen. These values are affected by several factors which will be discussed in Section 4.1. The sixth step includes adding the values of the MF environment from before and after the test, and adding any other data that is needed for the MATLAB script to run.

In the seventh step, the ambient MF is removed from the measurement by adding the values noted in the steps three and five, which will be averaged and removed from each measured pose. This will result in a non-biased data which can be used for the estimation in the eighth step.

At the eighth step, the position and magnitude of the MDM are estimated for each axis and the final strength. A plot that shows the position(s) and strength(s) of the magnetic dipole(s) in the DUT coordinate frame is generated. For this script, the data should not be affected by the ambient MF for a more reliable result. The estimation results are produced by a script which uses a Particle Swarm Optimization (PSO) method. In this script, the assumed number of dipoles is needed for the PSO in order to generate the estimation of the measurement. After several iterations and lowering down the best fit value, the final estimation results are displayed in a plot. More details about the development of the PSO can be found in [2] [30].

The last step involves an analysis of the estimation and comparison with the specification or expected values. The position and magnetic properties of the MDM(s) are checked in order to see how good the results are. A follow-up is considered for improving the next set of measurements, and also to check if there are any non-expected results or something went wrong when performing the magnetic measurement.

4 Optical magnetic test bed: behaviour analysis

In order to identify the accuracy of the setup, it is necessary to identify the factors involved and analyse different scenarios based on those factors. Thus, this section performs measurements in several scenarios to understand how the system behaves. Based on this behaviour, an analysis to determine a more accurate magnetic moment is considered for future measurements. This section is organised as follows. Section 4.1 identifies which factors are relevant for accuracy and error analysis. Section 4.2 presents the measurements gathered in different scenarios. Section 4.3 describes the system behaviour and reviews the results for its future use and improvement.

4.1 Magnetometer, environment and camera detection

In this section, key aspects of the measurement performance are point out for a further improvement and analysis of the OMTB. The main factors affecting the accuracy of the results are in the following list. Each one of these limiting factors are presented:

1 Base sensitivity of the magnetometer

2 Environment where the magnetometer and cage are placed

3 Camera's detection for the position and orientation of each marker

The sensitivity of the magnetometer can reach the order of hundreds pico-Tesla (pT), which is desired. Nevertheless, the usual order that is obtained for the compensation values in each axis is around tens nT, which is considered to be accurate enough for performing the measurement. Note that the step between the magnetometer's readings is not continuous and can vary from pT to nT. Normally, the values do not jump significantly in the range of nT, but they do if there is a change in the external environment in the laboratory.

For generating a field-free region inside the Helmholtz cage, two approaches can be done: using a closed loop sensor, or manually tuning the values; as mentioned in Section 3.3. In Table 1, the comparison between these two approaches can be seen. Based on the experimental data, the manual tuning method was found to be the best one, since it focuses on getting the closest near-to-zero value by tuning the scale factors accordingly. Note that this approach might be the best one at the moment, but it also takes much more time than the closed loop sensor approach, which tunes the compensation values internally and gives the readings right away. For each measurement, these values need to be re-checked and tuned again if needed. The column "Not yet used" displays how these readings can vary over time from the last tuning. Note that the unit micro-Tesla is denoted as uT in Table 1.

The second aspect refers to the external factors affecting the ambient MF inside the Helmholtz cage, which affect the readings from the magnetometer. It is important to point out that the cage is placed in a changing environment, concerning the magnetic properties of the components that are in the OMTB's surroundings, and this

Values	Axis	Not yet used	Closed loop	Manually
Scale factors	x	last value used	1	best tuned value
	y	last value used	1	best tuned value
	z	last value used	1	best tuned value
Output readings	x	100 nT - 10 uT	10 – 50 nT	10 - 50 nT
	y	100 nT - 10 uT	50 – 200 nT	10 - 50 nT
	z	100 nT - 10 uT	200 – 500 nT	10 - 50 nT

Table 1: Comparison between output readings for a closed loop and manual tuning

environment should remain as much stable as possible when performing measurement. The possible external factors surrounding the Helmholtz cage that can compromise the measurement are, for instance, people with laptops and other possible magnetic objects like chairs, cables, or other machines in the laboratory. All of these external variations are kept as still as possible during the measurement, so the overall magnetic environment seen by the magnetometer is not affected greatly. These disturbances in the ambient MF are between tens to hundreds of nT depending on the external factor properties and distance to the magnetometer.

Taking the above mentioned into consideration, the values of the ambient MF before and after the measurements are loaded into a MATLAB script using Algorithm 1. This algorithm is used to remove the ambient MF from the MF readings of the data acquired in the measurement. In this way, the estimation and further analysis can be considered more reliably and accurately.

Algorithm 1 Ambient MF remover algorithm

load *measurement_data*

{**Before- and after-measuring Bartington software's values, in nT:**}
$ambient\_before = mean([\, x_{01}\, y_{01}\, z_{01};\ x_{02}\, y_{02}\, z_{02};\ x_{03}\, y_{03}\, z_{03};\,], 1)$
$ambient\_after = mean([\, x_{f1}\, y_{f1}\, z_{f1};\ x_{f2}\, y_{f2}\, z_{f2};\ x_{f3}\, y_{f3}\, z_{f3};\,], 1)$
$ambient\_Bartington = [\, ambient\_before;\ ambient\_after;\,]$'

{**Average of the values of the Bartington before and after the test:**}
$ambient\_s = mean(\, ambient\_Bartington,\, 2)$

{**Ambient MF is rotated in DUT frame:**}
$bMAGm\_B = rotateframe(\, conj(qMAGm) * qDUTm,\, ambient\_s')$
$b\_s = b\_s - bMAGm\_B$' {b_s **now is modified**}

Run inverse_MDM script for estimation results

The last factor which limits the accuracy of the OMTB is the camera's detection. The camera needs to be able to obtain the correct pose for each marker. However, all configurations are not easy for the camera to detect properly. The camera's detection can sometimes get confused with other non-existent markers in the image. For solving

this problem, a background isolation paper is used, as explained earlier in Section 3.1. When taking the measurements, it can be seen how in some configurations of the DUT, the marker detected starts blinking or switches the orientation. This behaviour changes depending on the way the marker is facing the camera, and the distance between the marker and the camera. Table 2 shows a strong relationship between how the marker is detected and its distance to the camera. The axes of the marker facing the camera are: x-axis towards left horizontally, y-axis upwards vertically and z-axis towards the camera lens. Note that the same size square marker of 37.7 mm was used at all distances. The values are expressed in degrees, except the distance.

Orientation	Distance	No detection	Detection	Hard to detect
+ y-rotation	0.10	30.84 - 43.39	49.01	77.01
	0.15	15.33 - 42.47	48.18	75.36
	0.39	None	19.70	66.46
- y-rotation	0.10	29.55 - 60.87	64.19	78.08
	0.15	12.01 - 55.59	59.55	74.52
	0.39	None	12.71	69.78
- x-rotation	0.10	31.24 - 71.73	81.2	85.53
	0.15	18.43 - 72.72	80.54	79.40
	0.39	None	35.13	68.52

Table 2: Types of detection based on distance, in meters, and angles, in degrees

In the next section, different distances between the markers and the camera, and several magnets are tested in order to see how the OMTB behaves. Their measurements are performed taking into consideration the limiting factors as explained in this section.

4.2 Test bed testing and evaluation

In this section, as earlier stated, three permanent dipole magnets have been measured in order to verify the accuracy of the setup by estimating their MDM. The camera has been fixed in two configurations: one closer to the markers, and another further away from the markers. Both estimation results will be compared for each of the magnets to see how the marker-to-camera distance affects the measurement estimations. In Figure 10 and Figure 11, both of these setup configurations can be seen, with a distance of 20 cm and 35 cm approximately, respectively.

Short and long configurations are illustrated in Figure 10 and Figure 11. In addition, the DUT used for these testing measurements can be seen in Figure 12, and the location of the marker in the magnetometer is shown in Figure 13. The DUT is a PLA 3D-printed cube of 50x50x50 mm^3 where all faces are covered by a 37.7 mm x 37.7 mm marker, six markers in total. The following three sections focus on the magnetic measurements of three permanent magnets using the DUT, magnetometer and configurations, illustrated in the figures already mentioned above.

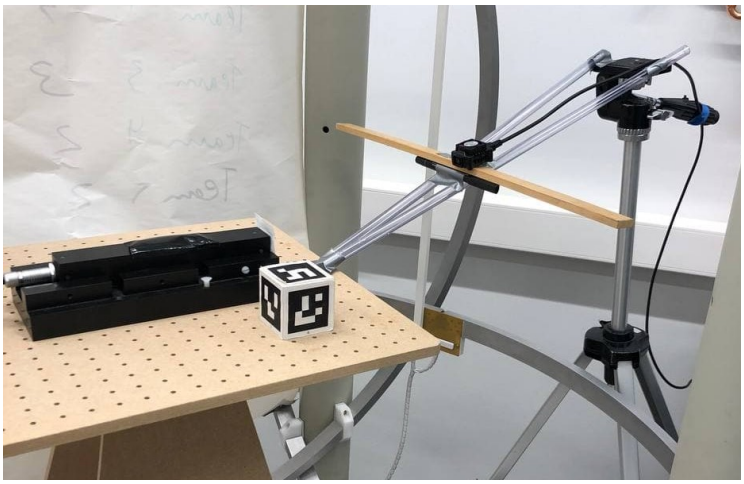

Figure 10: Setup with the camera fixed in a closer configuration from the target

Figure 11: Setup with the camera fixed in a further configuration from the target

4.2.1 Verification: permanent magnet E122

The first magnet used to verify the OMTB system is labeled as E122. The magnitude of the magnetic moment of the magnet E122 is calculated using Equation 9, as

$$m_{E122} = \frac{B_r}{\mu_0} \cdot V_{E122}, \tag{9}$$

where B_r is the residual flux density of the magnet in Tesla, μ_0 is the magnetic permeability in Henries per meter (H/m), and V is the volume of the magnet in m^3. Considering that the magnet E122 is a small cylinder with a height and diameter of

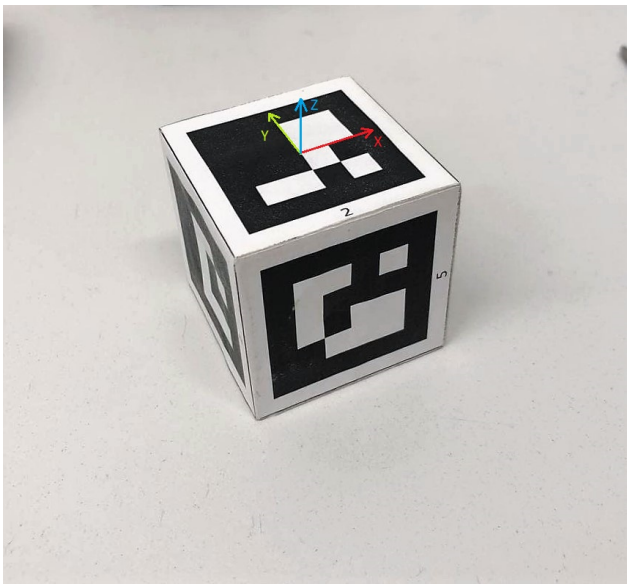

Figure 12: DUT used for the dipole magnets: PLA cube with 6 markers

Figure 13: Magnetometer used for the measurements: Mag-13, with one marker

1.7 mm, the magnetic moment of the magnet E122 is

$$m_{E122} = \frac{1430 \cdot 10^{-3}}{1.2566 \cdot 10^{-6}} \cdot \pi \cdot (\frac{1.7 \cdot 10^{-3}}{2})^2 \cdot 1.7 \cdot 10^{-3} = 0.0039\, A\, \mathrm{m}^2 \qquad (10)$$

Once the magnetic moment of the magnet E122 has been determined, the magnet is placed in the DUT. The magnet's location chosen is underneath the center of marker 6 in a cylindrical 8 mm deep hole. The dimensions of the DUT and magnet are known, 50 mm x 50 mm x 50 mm. Taking this into account, the position of the magnet can be deduced knowing the origin is in the center of marker 1. The location of the magnet E122 in the DUT can be seen in Figure 14. Table 3 lists the values of the position and characteristics of the permanent magnet E122.

Figure 14: Location of E122 permanent magnet on the DUT

Magnet E122

Characteristic	Value	Unit
Name label	E122	
Position x-axis	0.0000	m
Position y-axis	0.0179	
Position z-axis	−0.0230	
MDM x-axis	0.0000	$A \cdot m^2$
MDM y-axis	±0.0039	
MDM z-axis	0.0000	
MDM magnitude	0.0039	

Table 3: Magnet E122's features and position in the DUT

Once the MF inside the Helmholtz cage and the setup is ready, the two measurements can be performed using a long-distance and short-distance configuration. For both configurations, the procedure explained in Section 3.3 is followed. Note that the ambient MF at the beginning and at the end of the test has been considered in order to remove it using Algorithm 1 in Section 4.1. After the removal, the estimation of the MDM is performed, as explained in Section 3.3, and the plots of the estimated MDM in the DUT frame are generated.

The first magnetic measurement of the magnet E122 uses the long configuration. After the measurement procedure, the estimation of the MDM can be seen in Figure 15; a close-up figure of the same plot is displayed in Figure 16. The second magnetic measurement using the short configuration is then performed. The estimation of the MDM in the second measurement is shown in Figure 17 and a close-up is displayed in Figure 18. In Table 4, the values estimated for the two configurations are presented next to the actual values, also referred as specification values of the magnet E122.

As it can be seen in the estimation plots, the MF lines are as expected, where only one dipole with small magnitude appears. A comparison between the two configurations and the magnet's specification values is presented in Table 4. This table also provides information about a value named fGBest. The fGBest represents

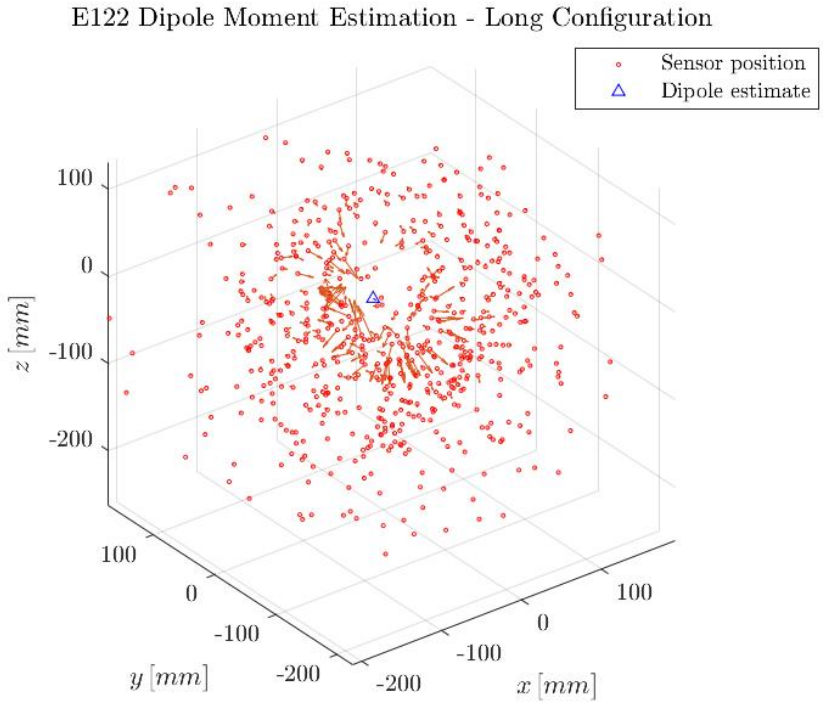

Figure 15: Magnet E122 MDM estimation in a long configuration setup

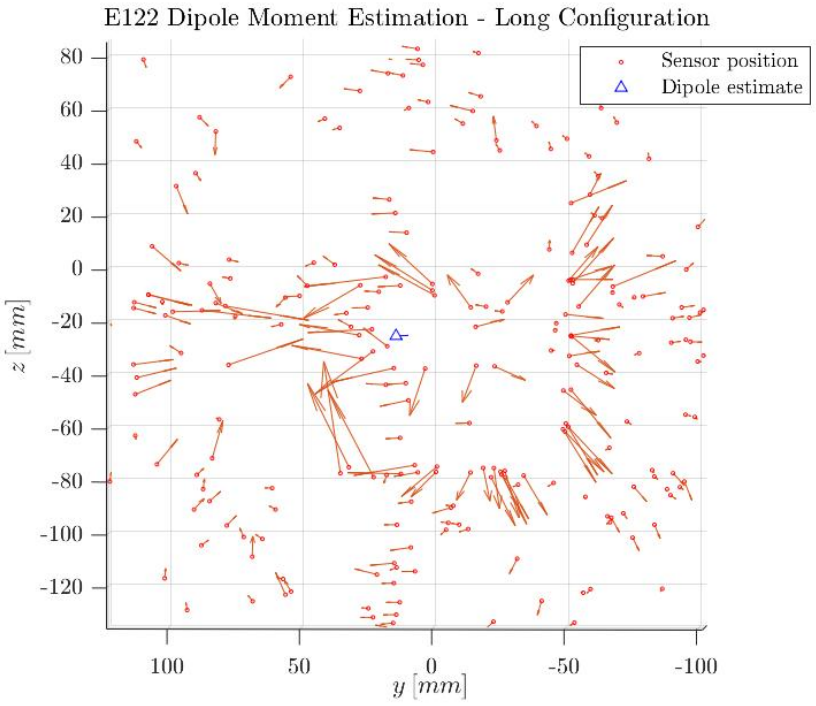

Figure 16: Close-up MDM estimation of Figure 15

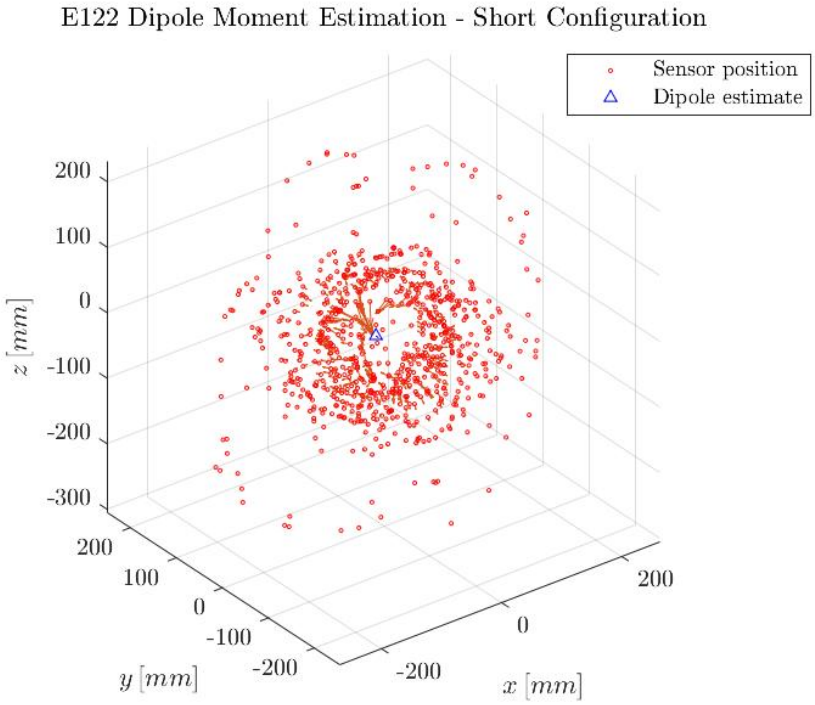

Figure 17: Magnet E122 MDM estimation in a short configuration setup

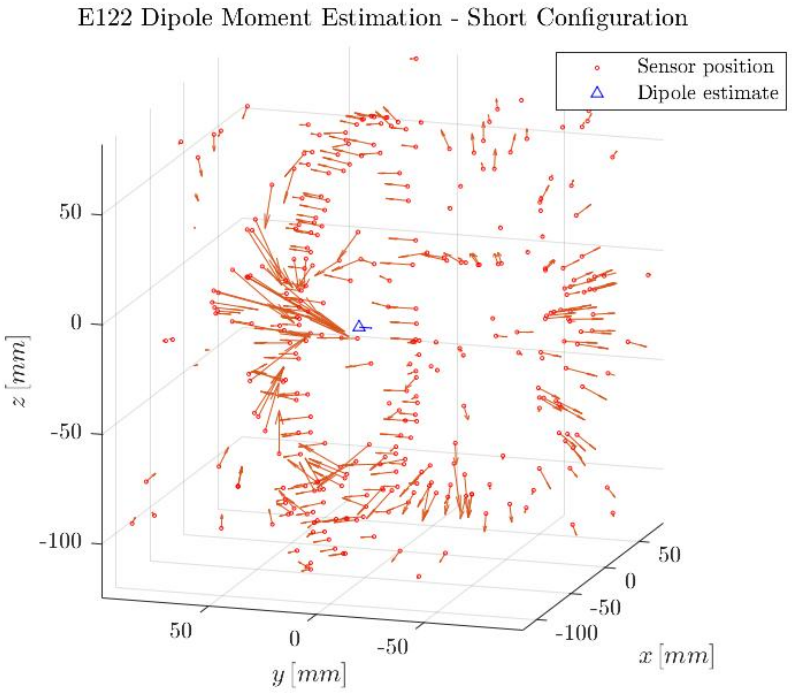

Figure 18: Close-up MDM estimation of Figure 17

how well the estimated MDM is fitted compared to the measured MF in each data point. More details can be found in [2].

Characteristic	**Actual**	**Long conf.**	**Short conf.**	**Unit**
fGBest	-	1.2580	0.3211	
Position x-axis	0.0000	−0.0018	0.0012	m
Position y-axis	0.0179	0.0143	0.0186	
Position z-axis	−0.0230	−0.0256	−0.0237	
MDM x-axis	0.0000	0.0004	−0.0006	$A \cdot m^2$
MDM y-axis	±0.0039	−0.0045	−0.0061	
MDM z-axis	0.0000	0.0002	0.0002	
MDM magnitude	0.0039	0.0045	0.0062	

Table 4: Actual vs estimation values for magnet E122 - long vs short configurations

Regarding the comparison in Table 4, the fGBest value is lower in the short configuration, and the position results are similar in both configurations. For the magnetic moment results, the component with the strongest moment is displayed as expected, in the y-axis. Based on the estimation and specification values, the calculated percentage errors for the long configuration are 16.369 % in dipole position and 15.996 % in MDM estimation. A 5.483 % in dipole position and 57.76 % in magnetic dipole estimation are obtained for the short configuration. Considering the magnitude of the MDM, the long configuration produces the least error compared to the specification value. But this last aspect can be also be due to the limitations of the real environment. In general, the short configuration presents better estimation results.

4.2.2 Verification: permanent magnet E317

Next, a stronger magnet has been chosen for testing: the magnet E317. Testing a stronger magnet can be useful to validate that the OMTB is able to estimate different types of dipole moments. The magnitude of the magnetic moment is calculated based on the same equation, Equation 9, using the new dimensions of the magnet E317. The magnet E317 is a 5 mm x 5 mm x 2 mm cube, which volume is different from the previous magnet. The other parameters of the equation, B_r and μ_0 remain the same. The calculation of the magnitude of the magnetic moment of the magnet E317 is presented in Equation 11,

$$m_{E317} = \frac{1430 \cdot 10^{-3}}{1.2566 \cdot 10^{-6}} \cdot (5 \cdot 10^{-3} \cdot 5 \cdot 10^{-3} \cdot 2 \cdot 10^{-3}) = 0.0509\, A\, m^2, \qquad (11)$$

where the terms used are in the same units as in the calculation of the magnitude of the magnetic dipole of the magnet E122. Note that the volume in this case is $V_{E317} = 5 \cdot 5 \cdot 2 = 50 \;\; mm^3$ or $5 \cdot 10^{-8} \;\; m^3$.

Once the magnitude of MDM for the magnet E317 has been determined, the magnet's MDM can be validated using the OMTB. The same steps as for the magnet E122 are followed. The location of the magnet E317 is in the center of an 8 mm

deep hole cylinder behind marker 6 of the DUT. The coordinates of the position of the new magnet are different due to the geometry of the magnet. The origin remains the same as for the previous magnet, in the center of marker 1. The location of the magnet can be seen in Figure 19, and the magnet E317's specification values are listed in Table 5.

Figure 19: Location of E317 permanent magnet on the 3D-printed cube

Magnet E317

Characteristic	Value	Unit
Name label	E317	
Position x-axis	-0.0011	m
Position y-axis	0.0180	
Position z-axis	-0.0250	
MDM x-axis	0.0000	$A \cdot m^2$
MDM y-axis	± 0.0509	
MDM z-axis	0.0000	
MDM magnitude	0.0509	

Table 5: Magnet E317's features and position in the DUT

From this point, the same procedure as used for the magnet E122 is performed for the magnet E317. Therefore, the cancellation of the ambient MF inside the cage, the setup using a long and short configuration, the removal of the ambient MF and the estimation of the MDM are performed in the same way. The plots of the estimation are also presented and can be seen in Figures 20 - 23. In addition, Table 6 presents a comparison between the actual values, or specification values, and the estimated ones for the magnet E317.

The magnitude of the MDM and its location are shown in blue in the plots. As it can be seen, the magnitude is bigger than in the previous magnetic measurement. The MDM vector is displayed as expected. The MF lines are coherent with the estimation of the MDM. From the previous measurement, it has been observed that

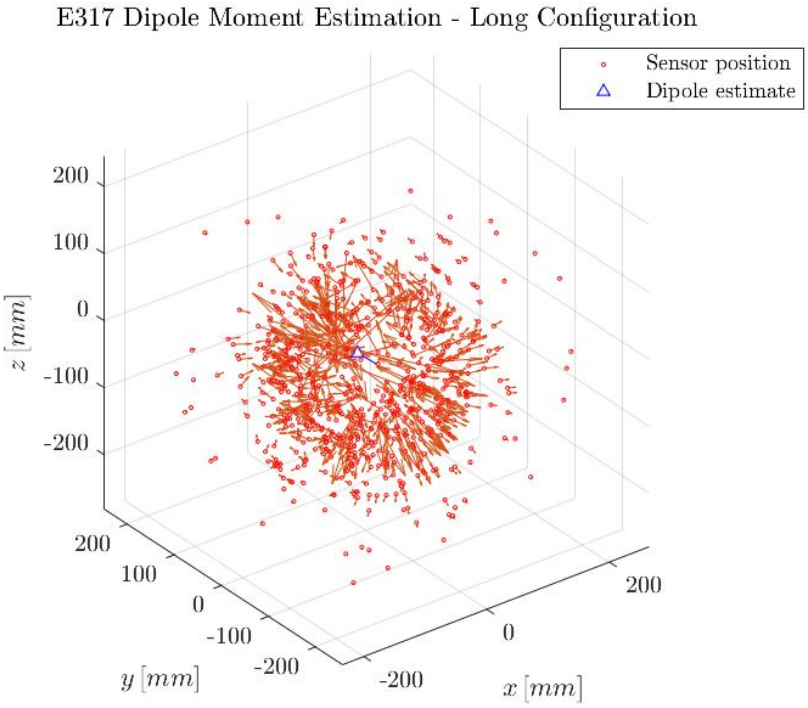

Figure 20: Magnet E317 MDM estimation in a long configuration setup

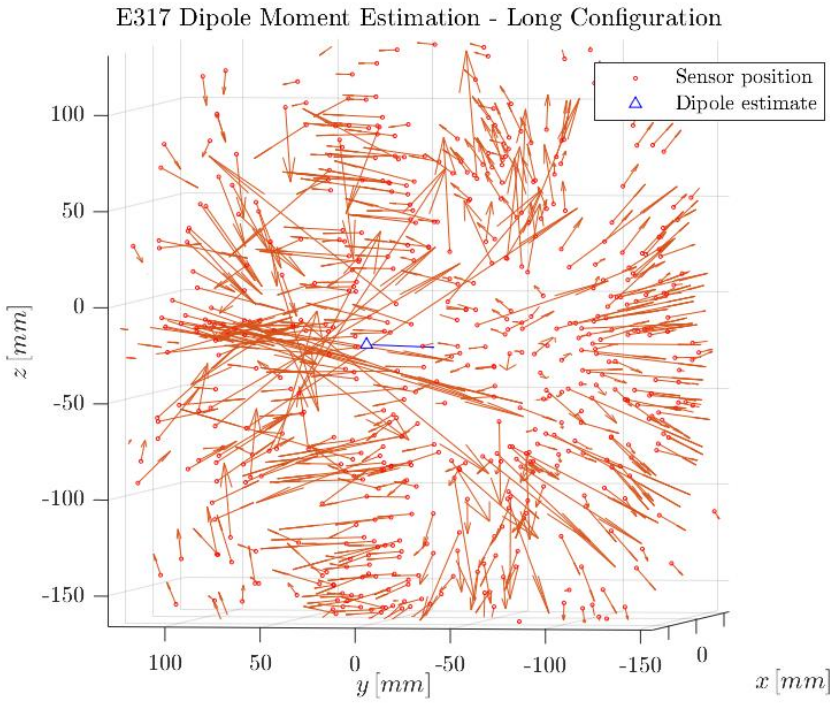

Figure 21: Close-up MDM estimation of Figure 20

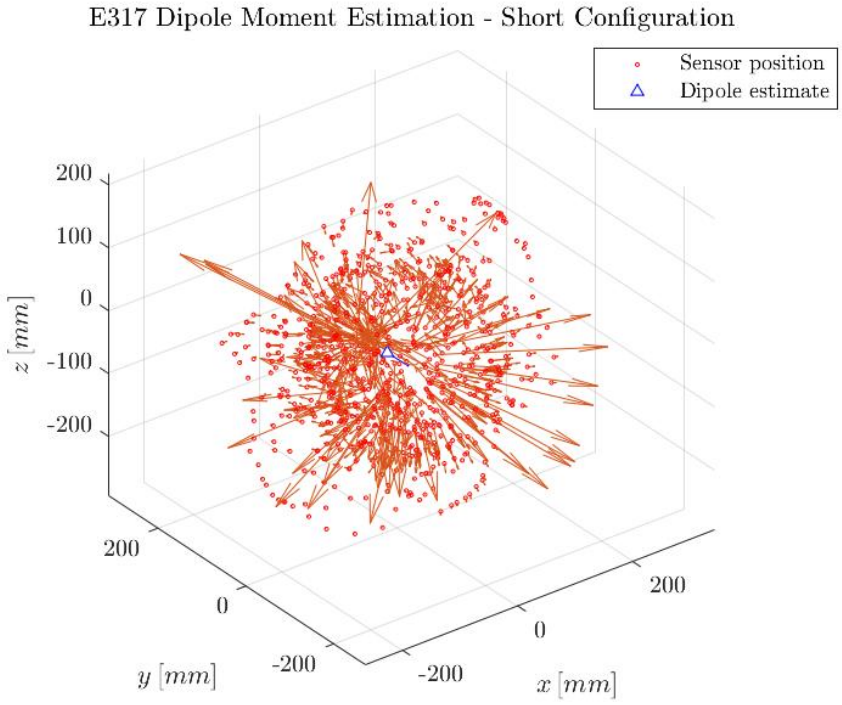

Figure 22: Magnet E317 MDM estimation in a short configuration setup

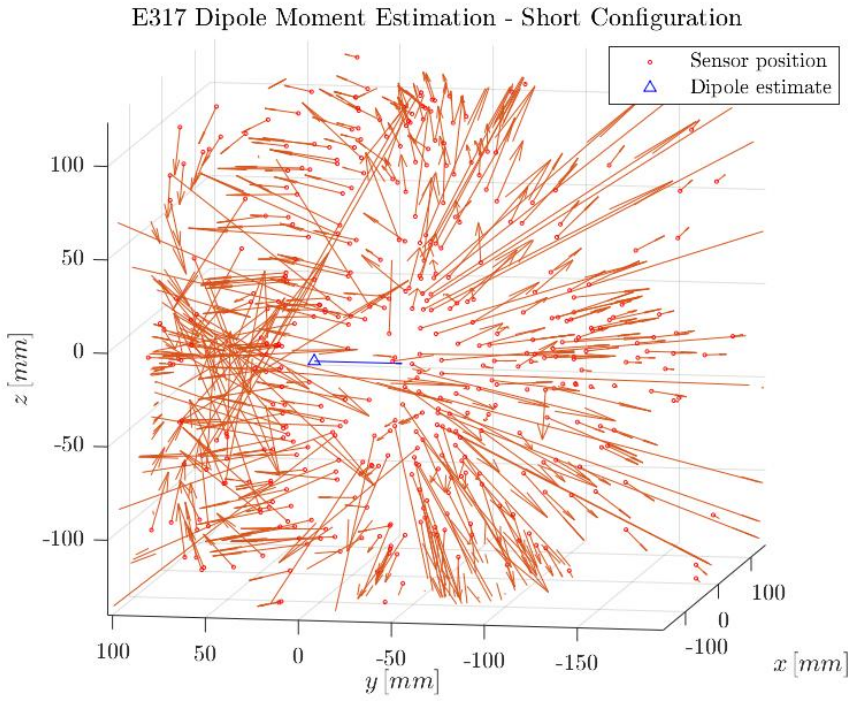

Figure 23: Close-up MDM estimation of Figure 22

more data points are related with a more accurate approximation in the estimated MDM and MF. Hence, these measurements have 720 - 800 data points each, and the measurement of the magnet E122 has around 500 measured points. The values of the position and magnetic properties of the MDM are presented in Table 6 for the magnet E317.

Characteristic	**Actual**	**Long conf.**	**Short conf.**	**Unit**
fGBest	-	1.5875	0.3028	
Position x-axis	−0.0011	0.0007	−0.0023	m
Position y-axis	0.0180	0.0176	0.0205	
Position z-axis	−0.0250	−0.0241	−0.0259	
MDM x-axis	0.0000	0.0039	−0.0013	$A \cdot m^2$
MDM y-axis	±0.0509	−0.0348	−0.0469	
MDM z-axis	0.0000	−0.0013	−0.0002	
MDM magnitude	0.0509	0.0350	0.0469	

Table 6: Actual vs estimation values for magnet E317 - long vs short configurations

As displayed in the table, the short configuration presents better results in general, particularly in the magnitude of the MDM. For the estimated position, both configurations seem to have similar results. However, regarding the magnetic features, the estimation is more accurate in the short configuration. The best method to observe this is by calculating the percentage error for the position and MDM estimation for each of the configurations. For the long configuration errors of 6.622 % in position and 31.171 % in MDM estimation are observed, while for the short configuration the errors are 9.539 % in position and a 7.8345 % in MDM estimation.

4.2.3 Verification: permanent magnet E200

The last permanent magnet considered in this thesis is the magnet E200, the strongest one used for the permanent magnet measurements. The MDM of the magnet E200 is determined in Equation 12, and it has been chosen in order to see how the system behaves with a strong magnet inside the non-saturation region of the magnetometer Mag-13. Using this magnet several attempts have been performed to properly determine its MDM and MF when using the long configuration. During the measurements, the MF could have been disturbed due to changes in the lab environment. In order to perform the measurements, first the theoretical magnitude of the MDM of the magnet E200 is calculated

$$m_{E200} = \frac{1430 \cdot 10^{-3}}{1.2566 \cdot 10^{-6}} \cdot (10 \cdot 10^{-3} \cdot 10 \cdot 10^{-3} \cdot 5 \cdot 10^{-3}) = 0.5093\, A\, m^2, \tag{12}$$

where the magnet E200 is a 10 mm x 10 mm x 5 mm cube. The other two terms in the calculation remain the same. The magnet's position in the DUT is located in the same way as for the other magnets. However, the coordinates vary due to the change in the dimensions of the magnet E200. Figure 24 illustrates the location of

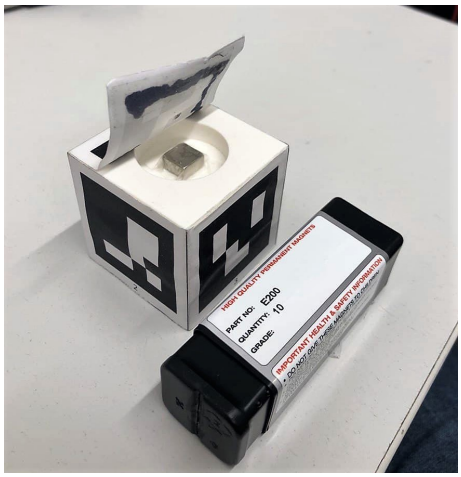

Figure 24: Location of E200 permanent magnet on the 3D-printed Cube

Magnet E200

Characteristic	Value	Unit
Name label	E200	
Position x-axis	0.0000	m
Position y-axis	0.0195	
Position z-axis	−0.0250	
MDM x-axis	0.0000	$A \cdot m^2$
MDM y-axis	±0.5093	
MDM z-axis	0.0000	
MDM magnitude	0.5093	

Table 7: Magnet E200's features and position in the DUT

the magnet in the DUT, and Table 7 displays the specification values for the magnet E200 based on its characteristics and placement.

After all values are collected, the same measurement procedure as for the other two magnets is performed. The magnetic measurements are performed using the two configurations used in the other measurements as well, long and short. Figures 25 - 28 display the estimation plot for the MDM of the magnet E200. Table 8 provides a comparison between the estimation results and the specification values of the magnet measured.

As it can be seen in the plots, the arrows are much bigger compared to the other magnets due to the strength of the magnetic properties of the magnet E200. The MDM estimation, position and magnetic moment characteristics, are displayed in blue in the estimation plots. The shown results are as expected since the magnet E200 is stronger than the other magnets measured. In these estimation plots, the MF lines are more difficult to distinguish due to the bigger arrows and the large amount of data points, around 700 - 800 points measured.

Besides, note that the MDM directions are opposite in the long and short configurations. The direction of the MDM is different because the magnet was

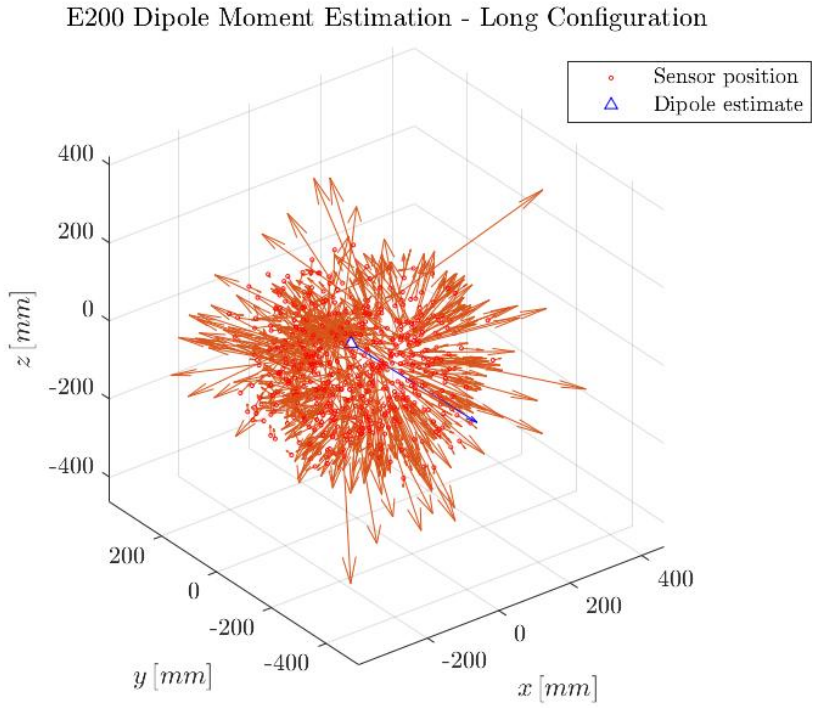

Figure 25: Magnet E200 MDM estimation in a long configuration setup

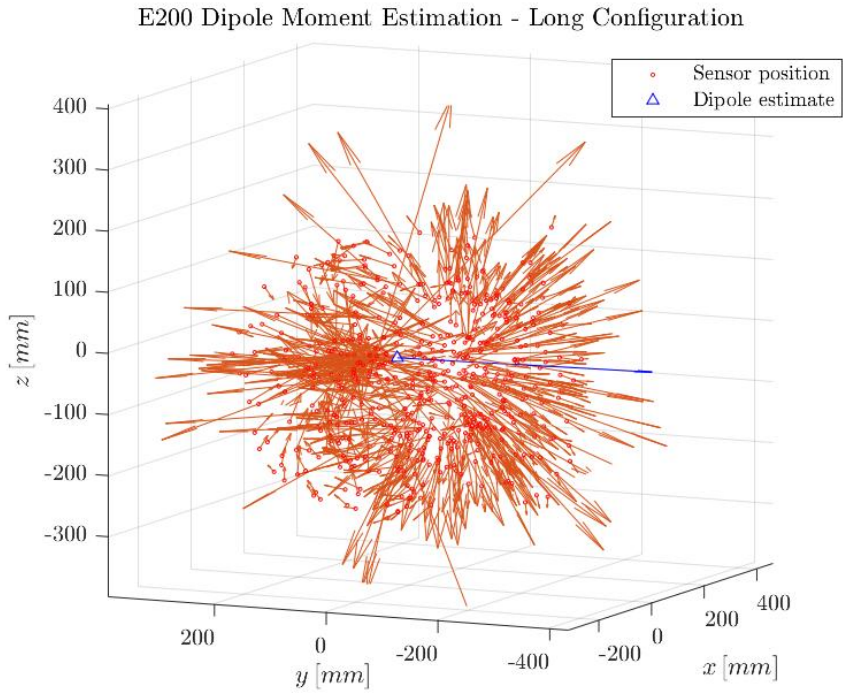

Figure 26: Close-up MDM estimation of Figure 25

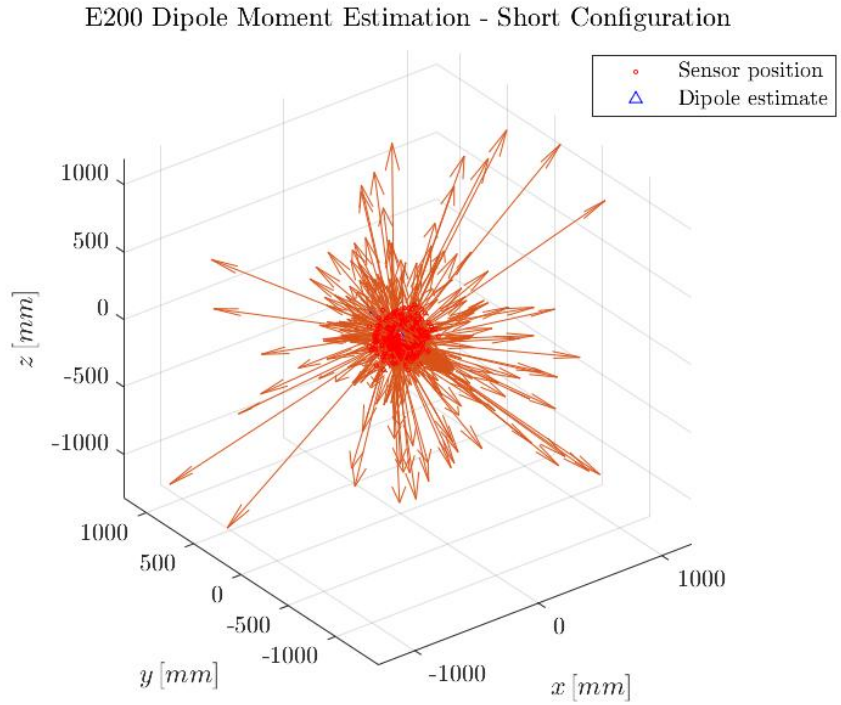

Figure 27: Magnet E200 MDM estimation in a short configuration setup

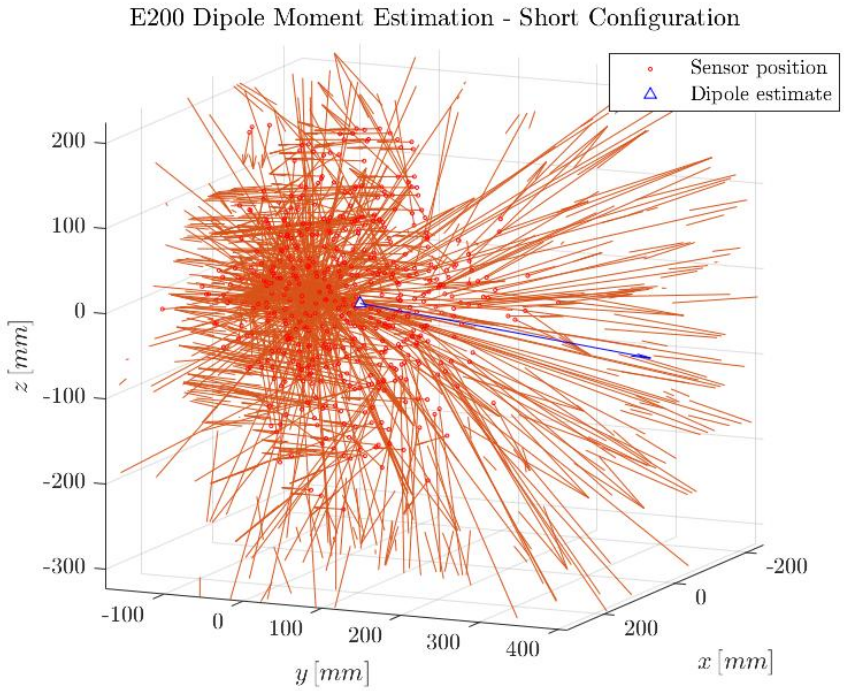

Figure 28: Close-up MDM estimation of Figure 27

flipped in the second measurement. For the long configuration, several measurements needed to be performed in order to have a correct estimation. The orientation of the magnet E200 was flipped in the DUT when repeating some of the testings. Table 8 displays the estimated values and compare them to their actual values.

Characteristic	**Actual**	**Long conf.**	**Short conf.**	**Unit**
fGBest	-	0.6524	0.6075	
Position x-axis	0.0000	0.0000	0.0041	m
Position y-axis	0.0195	0.02111	0.0152	
Position z-axis	−0.0250	−0.0269	−0.0263	
MDM x-axis	0.0000	0.0019	−0.0627	$A \cdot m^2$
MDM y-axis	±0.5093	−0.4564	0.3986	
MDM z-axis	0.0000	0.0064	−0.0210	
MDM magnitude	0.5093	0.4565	0.4041	

Table 8: Actual vs estimation values for magnet E200 - long vs short configurations

By studying Table 8, both fGBest are pretty similar. Even though the short configuration has closer results to the specification values, the estimation results for the long configuration are more accurate. Based on these results, the percentage errors are 7.864 % in position and 10.37 % in MDM estimation, for the long configuration. For the short configuration, a 19.25 % in position and a 20.663 % in MDM estimation are obtained. By comparing the results, in this case better results can be observed in the long configuration.

4.2.4 Summary: permanent magnets verification

After evaluating three different permanent magnets, it can be concluded that not only the long and short configurations affect the estimation results but also how well the measurement is performed. Taking these observations into account, for example, the results can be improved if there are less magnetic disturbances from the surroundings; and also, by measuring the DUT poses where the markers are more visible and the rotation is stable. The detection is related to the distance between the camera and the marker, since some poses present difficulties in their detection. Considering all the errors of the measurements, an average percentage error can be calculated for each configuration. A 10.3 % in dipole position and 19.2 % in dipole moment, for the long configuration, while a 11.4 % in dipole position and 28.8 % in dipole moment, for the short configuration, are calculated.

The results are affected by external and limiting factors already considered and presented in Section 4.1. In other words, how well the MF was cancelled and what are the magnetic disturbances in the lab that can also affect the estimation results. Also, the DUT does not move completely steadily when it is rotated in all poses. In order to better understand the system's behaviour new variables need to be created and defined based on these observations. These new variables are introduced in the following section.

4.3 View area and pointing angle

In this section, the concepts of View Area (VA) and Pointing Angle (PA) are presented, as well as a method used to calculate and use them accordingly. As it has been observed in Section 4.2, the estimation of the testing measurements is affected by the distance between the camera and the markers, since the markers are more difficult to detect further away from the camera which could generate wrong pose data points during the measurement.

VA refers to the percentage ratio between the area of the marker over the area of the camera's visual. Therefore, as the marker gets closer to the camera, its VA increases; since there is a larger marker area in the camera's FOV. This is a key concept defined in such way that it can be used for different distances and marker sizes, since the variable VA is independent from them. VA is implemented and calculated as presented in Algorithm 2. Consequently, VA is mathematically defined as follows

$$VA = \frac{a}{A} \cdot 100 = \frac{a_{px}}{A_{px}} \cdot 100 \text{ [in \%]}, \tag{13}$$

where a is the area of the marker in meters, A is the area of the visual in meters, a_{px} is the marker's area in pixels, and A_{px} is the total screen area in pixels. Note that A_{px} is a straightforward calculation by multiplying screen's width with its height in pixels, 640 px x 480 px in this case. When it comes to a_{px}, it is extracted directly from the picture by using an image software which measures the area selected in pixels.

For the VA calculation, based on the raw data from the camera, A and a can be obtained. Firstly, A is calculated based on the FOV, horizontally and vertically as shown in Algorithm 2, and the distance between the camera and the marker. Horizontal FOV is 65 degrees, provided by the Jevois A-33 camera specifications [31], and vertical FOV is calculated based on the horizontal FOV. Secondly, the method used to calculate a needs to be cross-checked with the experimental area, a_{px}, which is compared to the calculated a in Algorithm 2. The algorithm uses the marker's size and the projections of the x-axis and y-axis rotations, given by the detected marker's orientation from the camera.

Regarding the comparison between the VA using a ($VA_{experimental}$) vs using a_{px} (VA_{px}), a correlation between them can be seen. An average ratio which can be named as visual corrector factor is needed in the calculation inside the algorithm of the $VA_{experimental}$ to match the real VA_{px} which is calculated directly from the images. This range of values over the distance can be seen in Figure 29, which can be considered as the visual effect from the camera when calculating the actual area vs the image's area. By taking this into consideration, $VA_{experimental}$'s calculation can be corrected using this ratio which can be named as visual corrector. This visual corrector has been inferred from the comparison of at least 60 % of all the data's a_{px} and a, which can be seen in Figure 29. The factor used as a corrector in the calculation of VA is the mean value of the comparisons; which gives the best output for the calculation. The value of the corrector is 1.5977.

Alternatively, another main concept of this section is the PA (introduction of the Euler angles can be found in Section 2.1. This term can be defined as the angle

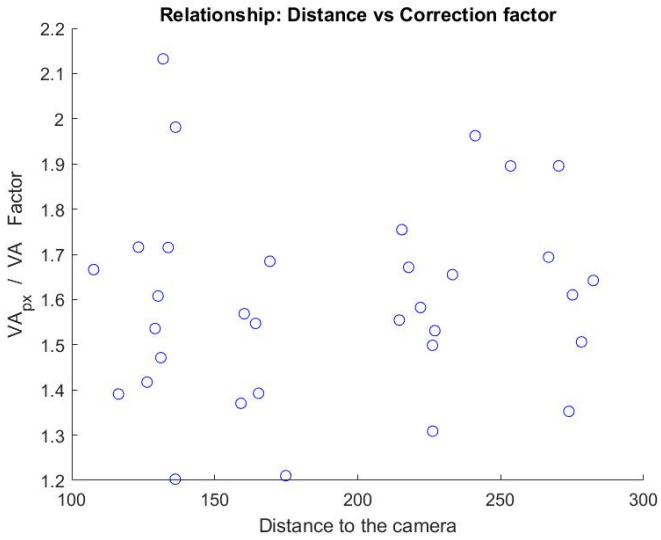

Figure 29: Visual corrector factor VA_{px}/VA at different marker to camera distances

between the z-axes of the camera and the marker. It is zero degrees when the axes are parallel and in opposite direction. In other words, when the marker is fully facing the camera. Hence, based on this definition there can be two options: PA_h, which is the angle between the marker's z-axis and the *horizontal* plane where the camera's z-axis is placed; and PA_v, which is the angle formed by the vertical plane where the camera's z-axis is located and the marker's z-axis. By using these two angles, the z-axis of the marker, its pointing angle, is completely defined since the rotation in the z axis does not provide any extra information of the orientation of the marker.

Consequently, these two variables are combined into a single one which can be called combined PA, or simply PA. This variable is defined as the axis angle provided by PA_h (x-axis rotation) and PA_v (y-axis rotation). The axis angle is calculated based on all three rotations in the x, y and z axes. The z-axis rotation, or roll angle, has been evaluated in Table 9 to check if it can affect the other two rotations. If the roll angle does not affect the other ones, this angle can be considered zero when calculating the axis angle. Therefore, the PA would only be described by the x and y rotations. The z-axis rotation effect on the other two axis rotations should be zero theoretically. In order to check this behaviour, three configurations have been tested with different PA_h and PA_v combinations and an approximate zero roll angle. Then, keeping the x rotation, yaw, and the y rotation, pitch, while changing the roll rotation in order to see if there is any change in the other axes.

Note that all angles provided by Table 9 are in degrees. Based on the results of Table 9, the effect of the roll angle over the pitch and yaw angles can be considered negligible. No effect can be seen on the PA when changing only the roll angle. Hence, when determining the axis angle for the combined PA, the roll angle can be set as null. The algorithm used in MATLAB for calculating the VA and PA variables is presented in Algorithm 2. In Section 5.1, several combinations of VAs and PAs are tested in order to evaluate the accuracy of the camera's detection.

	Pitch (x rotation)	Yaw (y rotation)	Roll (z rotation)
Test 1	71.8327	0.5327	**-0.5953**
	72.1580	0.5884	**89.5449**
Test 2	1.1028	-45.7368	**0.5534**
	1.3262	-47.8058	**90.7879**
Test 3	76.2891	-13.2024	**-39.5001**
	76.2173	-12.0251	**49.63987**

Table 9: Roll effect on pitch and yaw angles in degrees for three different configurations

Algorithm 2 VA and PA calculation

Initialize: screen width and height, Horizontal FOV (FOV_H) and visual corrector
Extract: distance (z component position) and quaternion
Convert $euler\_angles = quat2eul(quaternion,'XYZ') * 180/pi$

PA calculation:
$PA\_h = 180 - abs(euler\_angles(1))$
$PA\_v = abs(euler\_angles(2))$
$PA\_axang = quat2axang(eul2quat([PA\_h\ PA\_v\ 0]) * pi/180)$

if $quaternion(1:end) == 0$
    $PA = NaN$
else
    $PA = PA\_axang(4) * 180/pi$
end

VA calculation:
$FOV\_V = 2 * atand((screen\_height/screen\_width) * (tand(FOV\_H/2)))$

$A = (2 * distance)^2 * tand(FOV\_H/2) * tand(FOV\_V/2)$
$a = marker\_len^2 * cosd(PA\_h) * cosd(PA\_v)$

if $A == 0$
    $VA = NaN$
else
    $VA = 100 * abs(a/A) * visual\_corrector$
end

5 Evaluation of the optical test bed

This section provides a full accuracy analysis of the marker's pose to evaluate specific behaviours in the detection of the camera, as well as adapts this in-depth analysis into the software detection method. These new modifications are presented as algorithms and adapted accordingly into the general setup. Section 5 is structured as follows. Section 5.1 evaluates and analyses the marker's detection error, and Section 5.2 describes the results and how the scripts have been adapted to get a better result.

5.1 Position and orientation analysis

In order to understand how well the detection by the camera is done, several poses of the markers are studied taking into account the concepts of VA and PA. Since the improvement of the OMTB is heavily determined how the detection of the markers is performed. Both the estimation of the position and the magnetic characteristics of the dipole, need a correct detection of the pose of the markers. For this analysis, only two markers are required since the purpose of this analysis is to determine how the camera detects the marker position and orientation in several poses, hence, different VAs and PAs. The markers chosen are the marker 4, acting like the DUT for the MATLAB script, and marker 0 which acts as the magnetometer in the script. The sizes of the markers used in these measurements are 37.7 mm x 37.7 mm.

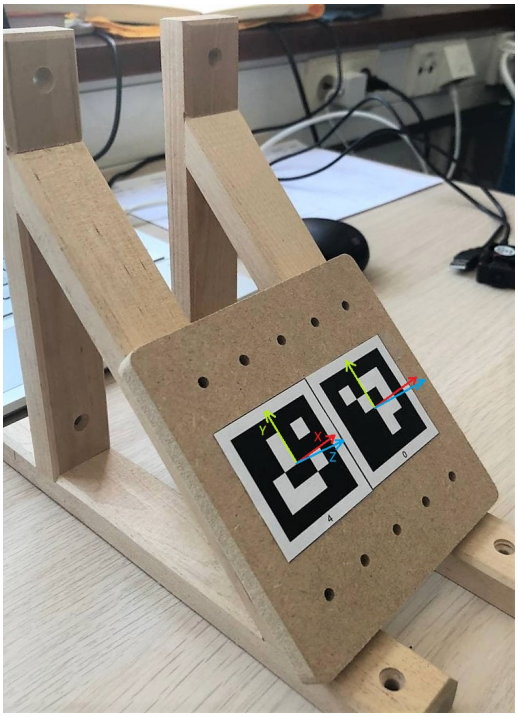

Figure 30: ArUco markers' location for position and orientation analysis

The orientation of the marker 4 is relative to the orientation of marker 0. So, in this case, both markers are placed in a flat surface where this relative orientation

provided by the measuring MATLAB script from the camera's detection should be zero. In this way, the error in the orientation is clearly spotted. For the position evaluation, the deviation and the mean absolute error are calculated based on the detection results. The position detected by the measuring MATLAB script must remain the same in each of the poses studied, since the markers are not changing their relative position to each other.

Since the purpose of this evaluation is the detection of markers, the Helmholtz coils and the MF are not required. Therefore, a modified measuring script has been implemented. All variables and calculations related to the MF has been deleted in this new measuring script. The following measurements are performed for studying how well the pose of the markers is detected and processed by the measuring script. The relative pose of the markers remains the same in all the measurements, and their location in the flat surface can be seen in Figure 30.

The measurements are started with four different distances between the camera and the markers. Each of the four distances is referred as "stop" in the figures. In each stop, the camera detects the pose of the marker 4 relative to the marker 0, and the mean absolute error is gathered. The poses have been chosen using different combinations of PA_h and PA_v. Both variables vary from 0 to 90 degrees, with steps of approximately 22.5 degrees. For example, (PA_h,PA_v) = (0,0), (0,45), (0,90), (45,0), (45,45), (45,90), (90,0), (90,45), and (90,90). Some of these combinations are illustrated from Figure 31 to Figure 33 for different stops. Once an specific combination has been performed at all four distances, all the data is gathered in a table where distance, PA, VA, errors and deviation values are collected. The extraction of the distance, PA, and VA from the marker's detection has been introduced in Section 4.3.

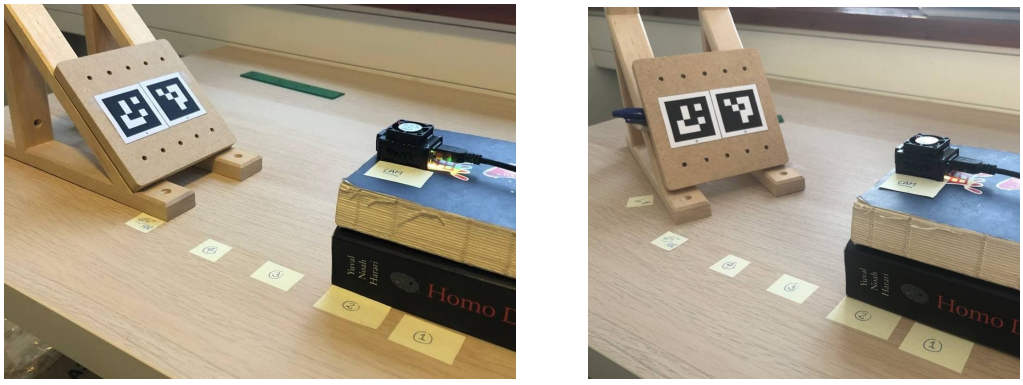

(a) $PA_h = 45$ and $PA_v = 0$ (b) $PA_h = 75$ and $PA_v = 45$

Figure 31: Detection at the second stop in different orientations, angles in degrees

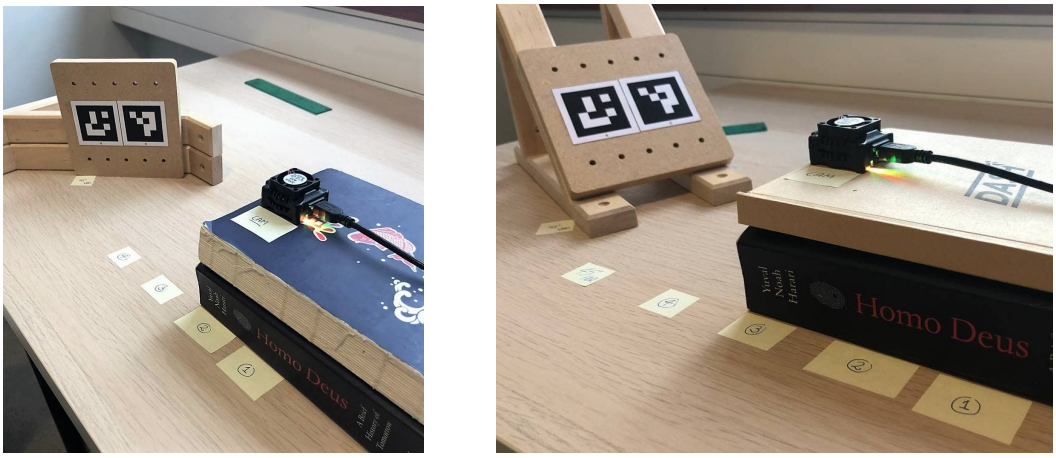

(a) $PA_h = 0$ and $PA_v = 45$ (b) $PA_h = 45$ and $PA_v = 45$

Figure 32: Detection at the second stop (a) and third stop (b) in different orientations, angles in degrees

(a) $PA_h = PA_v = 0$ (b) $PA_h = PA_v = 0$

Figure 33: Detection at the third stop (a) and fourth stop (b) in the same orientation, angles in degrees

The mean absolute error for the position and the orientation of the marker 4, as well as the deviation of the position detection, is calculated using Algorithm 3. The measuring script defines the position and orientation of each of the markers used. Note that the position of both markers is set as [0,0,0] in the measuring script. The orientation remains the same between the two makers, thus it is also defined as [0,0,0]. Since the relative pose remains the same for each measurement, around 35-50 data points with information of the detection of that specific pose are collected. In this

study, the position values detected by the script (p_s) for marker 4 and the relative orientation should match their earlier initialization ([0,0,0]). Hence, the absolute error is directly inferred from the detection, since it should be zero. Note that the orientation is transformed from a quaternion to an axis angle in the script which value should be null. For the deviation in position, the calculations used are clearly stated in Algorithm 3. The deviation shows how precise the position is measured for each pose detected in each measurement. The quaternion and position values are obtained through the modified measuring script. This modification is implemented in the measuring script developed for measurements on this OMTB. The development of the algorithms can be found in [2].

Algorithm 3 Error and deviation calculation

1: **Variables used from measurements:** p_s, qMAGm, qDUTm (*Magnetometer and DUT mean quaternions*)
2:
3: **Mean error position:**
4: error_pos = abs(p_s)
5: ME_px = abs(mean(error_pos(1,:))
6: ME_py = mean(pos_error(2,:))
7: ME_pz = mean(pos_error(3,:))
8: $Mean\_Error\_Position = sqrt(ME\_Px.^2 + ME\_Py.^2 + ME\_Pz.^2)$
9:
10: **Deviation in position:**
11: mean_p_s = [mean(p_s(1,:)); mean(p_s(2,:)); mean(p_s(3,:))]
12: $dev\_sum\_sq = sum((p\_s - mean\_p\_s).^2, 2)$
13: Dev_px = sqrt((dev_sum_sq(1))/(size(p_s,1)-1))
14: Dev_py = sqrt((dev_sum_sq(2))/(size(p_s,1)-1))
15: Dev_pz = sqrt((dev_sum_sq(3))/(size(p_s,1)-1))
16: $Mean\_Deviation\_Position = sqrt(Dev\_Px.^2 + Dev\_Py.^2 + Dev\_Pz.^2)$
17:
18: **Error in orientation in degrees rotated:**
19: qDUT2MAGm = conj(qMAGm)*qDUTm
20: quat_rotationDUT2MAGm = quat2axang(qDUT2MAGm)*180/pi
21: E_rot = abs(quat_rotationDUT2MAGm(4))

Once all measurements and their calculations are made, it is worthy to see how these errors and deviation behave for each of the poses studied. These poses, as it has been stated earlier, are defined by the VA and the PA. Therefore, a heat map has been generated to see the mean absolute error and the deviation changes for different combinations of VAs and PAs. In order to study a wide range of combinations, the heat maps presented in this section consist of more than 200 measurements in different poses with around 35-50 data points each one of them. Several heat maps are presented in Figures 34 - 38. These figures show the mean absolute error and deviation in position, and mean absolute error in the orientation's rotation in terms of PA vs VA or distance. All possible configurations in the maps have been

interpolated with the nearest known configuration data if that particular combination was not measured.

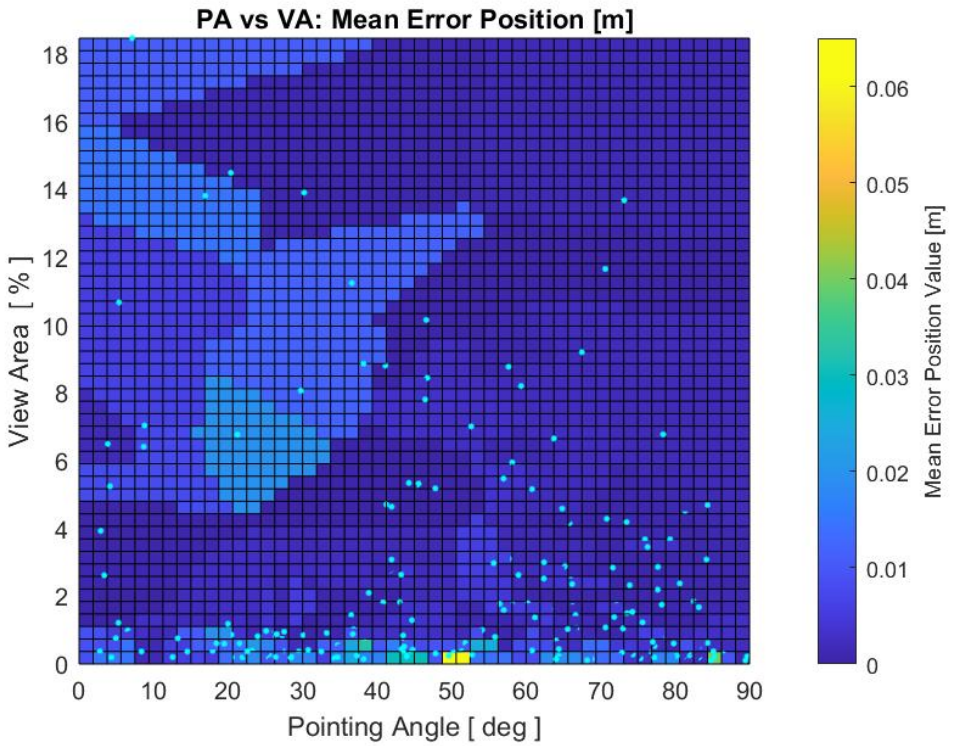

Figure 34: VA vs PA, mean absolute error in position in meters

In Figure 34, the mean absolute error in the detection of the position of the marker 4 is displayed in different colours where the error is zero for a dark blue, and yellow for an error of around 0.07 m. As it can be seen, in most poses the error in the detection is less than 0.015 m, or close to zero. For PAs lower than around 45 degrees and medium to high VAs, the error is less than 0.02 m; and for higher PAs, the mean absolute error remains low for all VAs. It is worth noticing that at the lowest values of the VAs, when the markers are far away from the camera, the detection is not completely accurate. Especially around 50 degrees the error is a lot higher compared with the rest of the plot. In general, this behaviour is expected until some extent. For the markers in a medium-high VA and facing more towards the camera, the mean absolute error is a slightly higher than when the PA starts to be higher than 45 degrees. In general, the error is expected to be higher when the markers are far away from the camera; and so it is in Figure 34, the error is expected to be slightly higher.

The deviation of the position is displayed in Figure 35. The behaviour is similar to the mean absolute error in position. For low to mid values of VA, and low to 40 degrees of PA, the deviation is higher than in other regions. For lower VAs, the deviation is around ± 0.025 m. The highest deviation is in the lowest VA and at a PA of 50 degrees, where the deviation is approximately ± 0.12 m. Note that for PAs lower than 25 degrees and low VAs, the deviation can reach ± 0.04 m. However, in

general, the deviation when detecting the position is low in 85 % of the plot, less than ± 0.015 m.

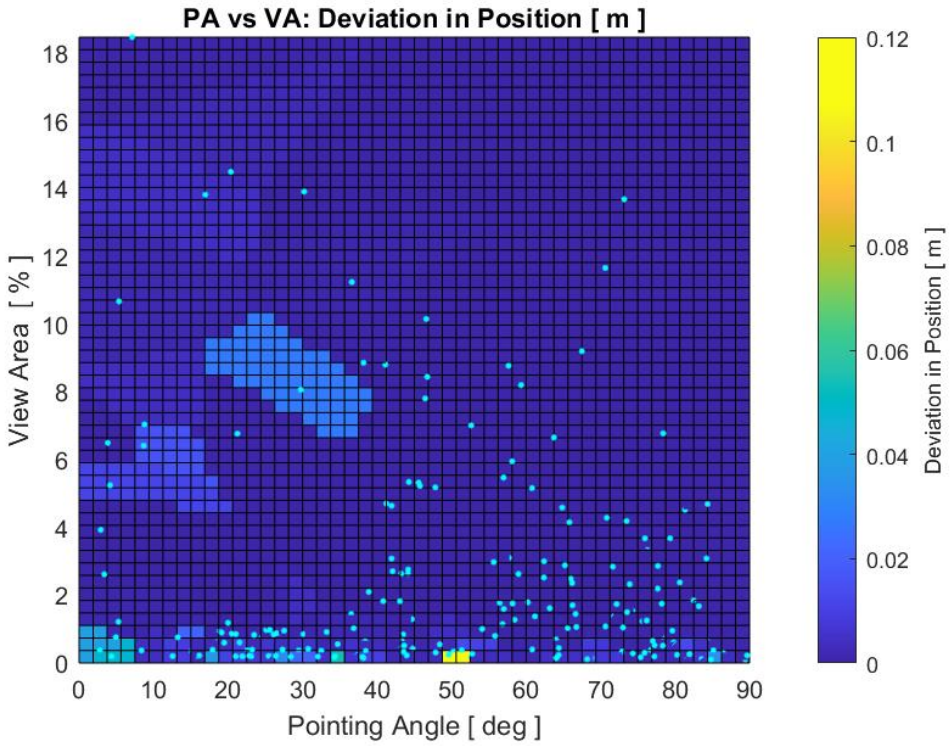

Figure 35: VA vs PA, deviation in position in meters

Another variable studied is the mean absolute error in orientation, as it has been stated earlier. The error in orientation is defined by how much the axis angle has been rotated. If the axis angle remains zero, the axes have not been rotated so the detection is fully correct. In Figure 36, the behaviour is close to the other heat maps presented in Figure 34 and Figure 35. Note that the biggest error occurs also at the low VAs, and between 40 to 55 degrees of PA, where the rotation ranges from 80 to 120 degrees. In the rest of the plot, it can be said that the error is less than 5 degrees approximately; except for zones with low VA and PA lower than 40 degrees where the error reaches around 20 degrees.

For extra information and understanding, heat maps where the variable is distance instead of VA have been generated as well. The distance would change depending on the size of the marker, since for the same distance the detection would be better if the marker is bigger. For this analysis, VA is a more useful and general term for this analysis, since it does not depend on the size of the marker. However, these plots are meant to provide extra information for the evaluation. This change has been applied to both mean absolute errors: in position and in orientation, as it can be observed from Figure 37 and Figure 38. These heat maps can be related to the previous ones with respect to the distance - VA relationship. From the heat maps it can be seen how the middle PA values get worse when increasing the distance between the camera and the marker. It can also be observed that the detection

starts to get worse around 0.65 m of distance. Therefore, the error can be minimized considerably if the measurements are taken at a smaller distance using the 37.7 mm x 37.7 mm markers; or at the same distance, but using bigger markers.

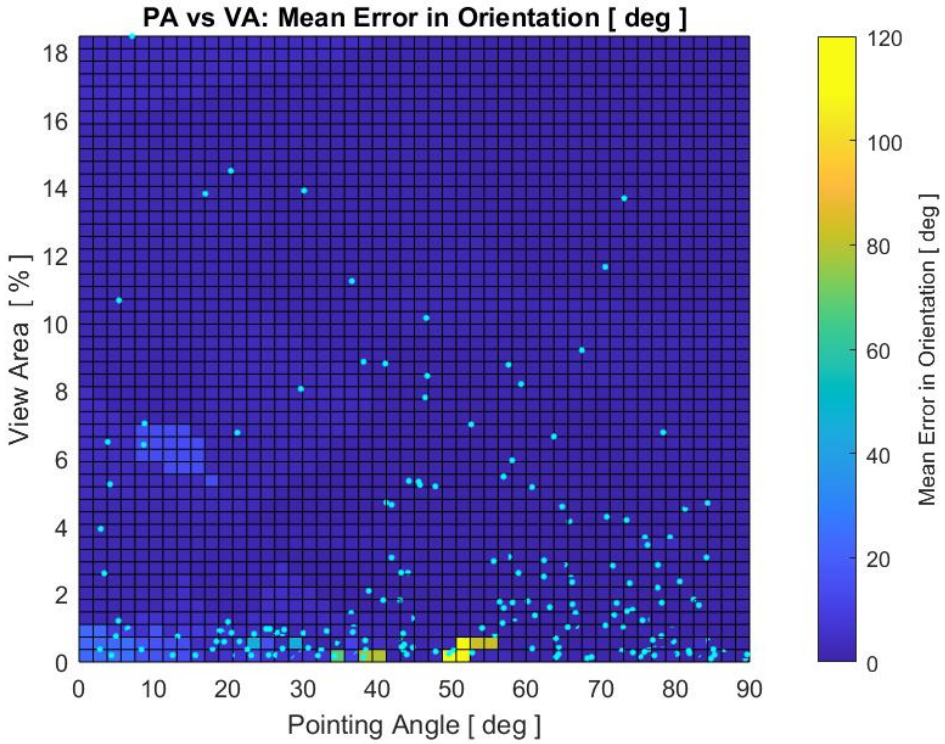

Figure 36: VA vs PA, error in orientation in degrees

5.1.1 Behaviour validation

This subsection is meant to validate the behaviour that can be seen from the error and deviation of the first part of Section 5.1 using markers of 37.7 mm x 37.7 mm. In order to validate the results, a small set of measurements using markers of a bigger size is performed to observe how similar the behaviour is to the one obtained with smaller markers. In this case, the VA variable should behave in the same way as, since it should be independent from the size of the markers. However, the distance where the accuracy gets worse should be larger than the one showed using smaller markers. For this validation analysis, more than 60 measurements have been done using the markers of 58 mm x 58 mm. Figure 39 shows how these new markers are placed in a big flat surface. Note that the markers used are the same, but in bigger size. Markers 0 and 4 are placed and oriented in the same way as in the analysis of the first part of Section 5.1, the only difference is the size of the markers.

In Figure 40, Figure 41, and Figure 42, a similar behaviour compared to the smaller markers can be observed. Note that the level of resolution is different in this case, since these plots are generated using smaller number of measurements. Thus, less data points and more interpolation are used to fill the heat maps. Nevertheless,

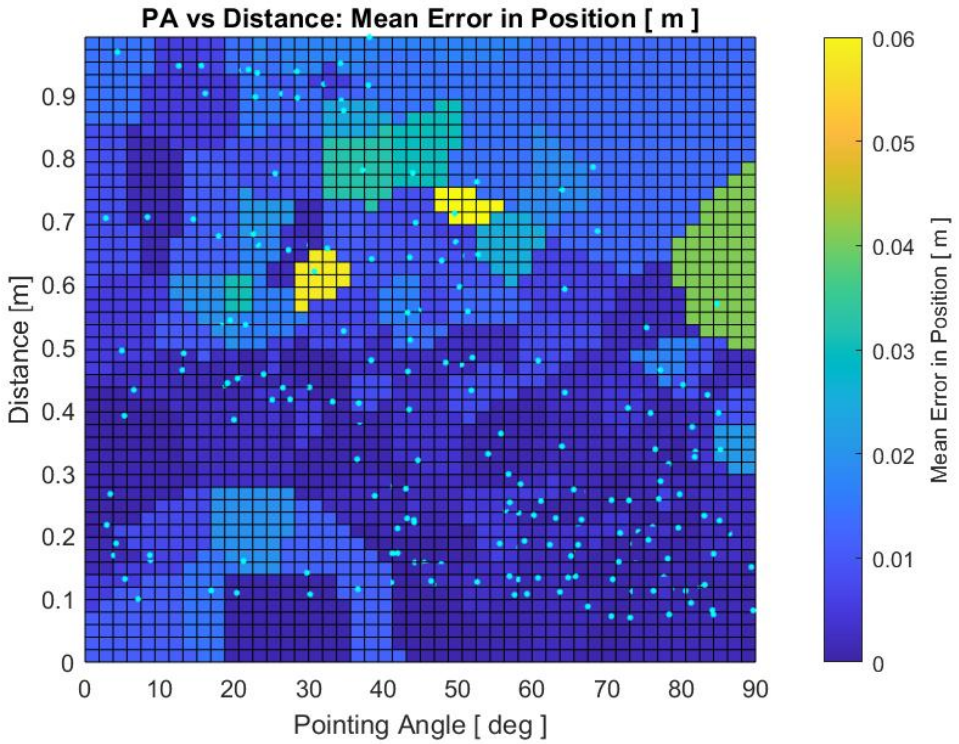

Figure 37: Distance vs PA, error in position in meters

the overall pattern is clearly similar for each one of them. For the mean absolute error in position, PAs lower than 40 degrees display more error, even higher for low VAs. The maximum error 0.08 m is reached at 40 degrees, similarly as the previous analysis. In Figure 41 and Figure 42, as stated above, the heat map pattern are alike compared to the heat maps generated by the smaller markers. Same conclusions for the behaviour in terms of VAs and PAs can be made. Therefore, the behaviour seen in the first part of Section 5.1 can be considered to be validated.

As it can be seen from Figures 43 and 44, the distance where the error increases is around one meter. This is expected since the markers are bigger than in the previous analysis. However, for some high PAs, the error is clearly higher for the distance of 0.6 - 0.8 m. This could be due to the interpolation with few data points. This limited amount of data points might infer a high error for that specific combination of PA and VA, since it is considering the nearest known value to determine this unknown error. If this is the case, some parts of the heat map might display differently. Nevertheless, the maps can be considered reliable for validation. Therefore, it can be said that the behaviour observed in the analysis with smaller markers is validated based on these heat maps as well.

After observing all the results, it can be concluded that the overall behaviour in the mean error in position and orientation, and deviation, is validated and can be taken into account for future magnetic measurements.

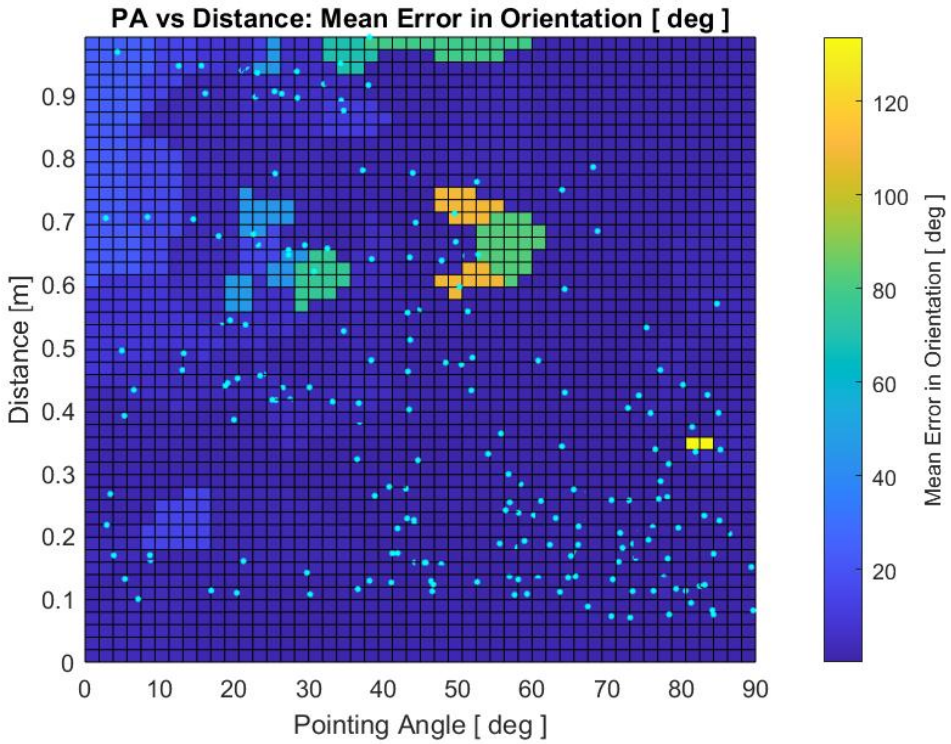

Figure 38: Distance vs PA, error in orientation in degrees

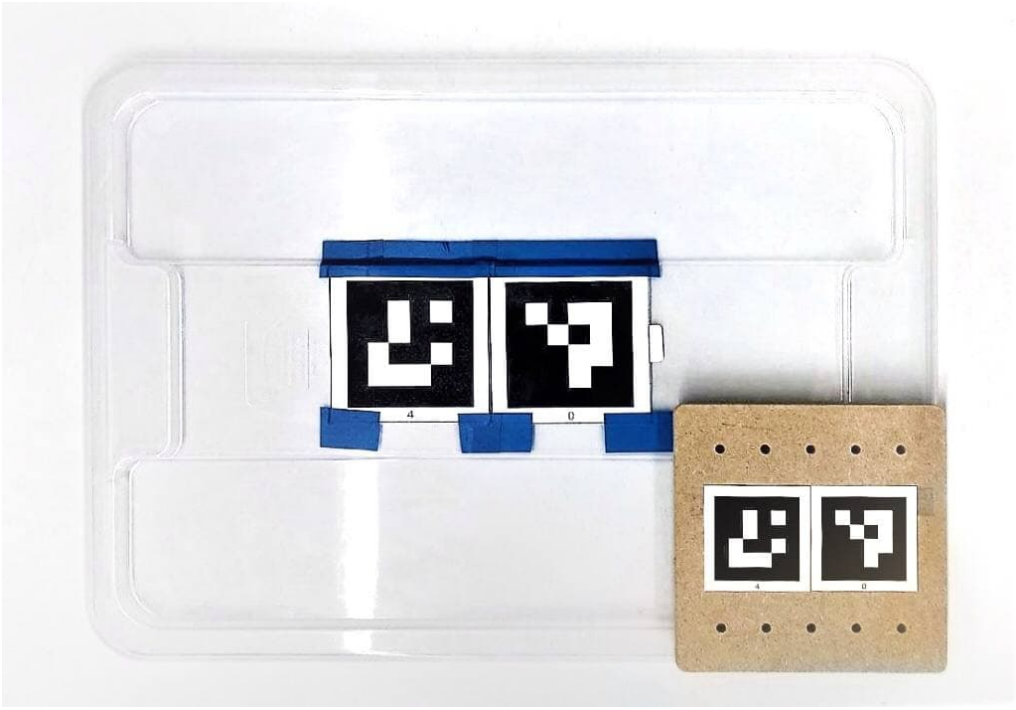

Figure 39: Bigger markers location and comparison with the smaller markers

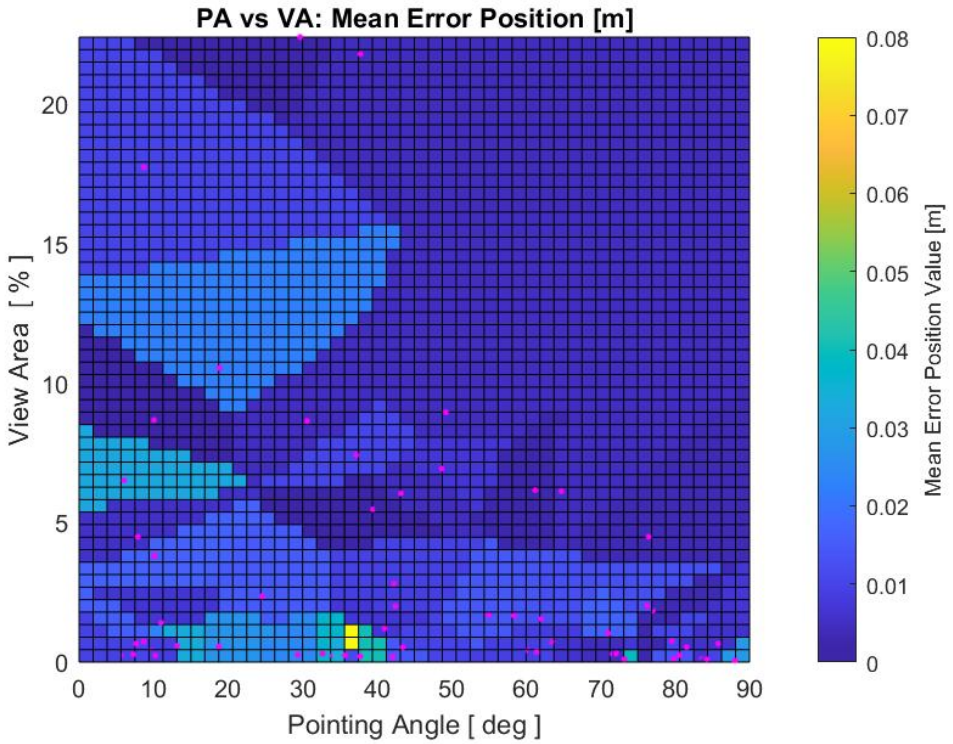

Figure 40: VA vs PA, error in position for validation

5.1.2 General analysis and final evaluation

After the validation, this subsection provides the data points initially used in addition of the new data points from the validation data. Therefore, the data points (using small markers) and the validation data (using bigger markers) can be used to plot a final overall heat map for the variables studied. The light blue points in the following figures represent the initial data, whereas the red-pink points refer to the validation data which is denoted with the addition of _B in its name. Small modifications in the pattern can be observed in Figure 45, Figure 41 and Figure 47; overall behaviour remains the same.

In conclusion, smaller VA detection is harder for the camera and so the accuracy is lower. As the VA increases, the position detection is better for PAs higher than 45 degrees, even though the overall error in the lower PA is not considerably high. For the deviation in position and orientation detection, the error is slightly worse for lower PA and VA; the worst for the lowest VAs values. The general accuracy detection from the camera in this setup is high, except for some poses where the markers are hard to detect. Therefore, in general terms, the camera detects the position with a mean absolute error of 0.05 m which deviates for each burst about ± 0.005 m, and the orientation with a mean absolute error of 5 degrees.

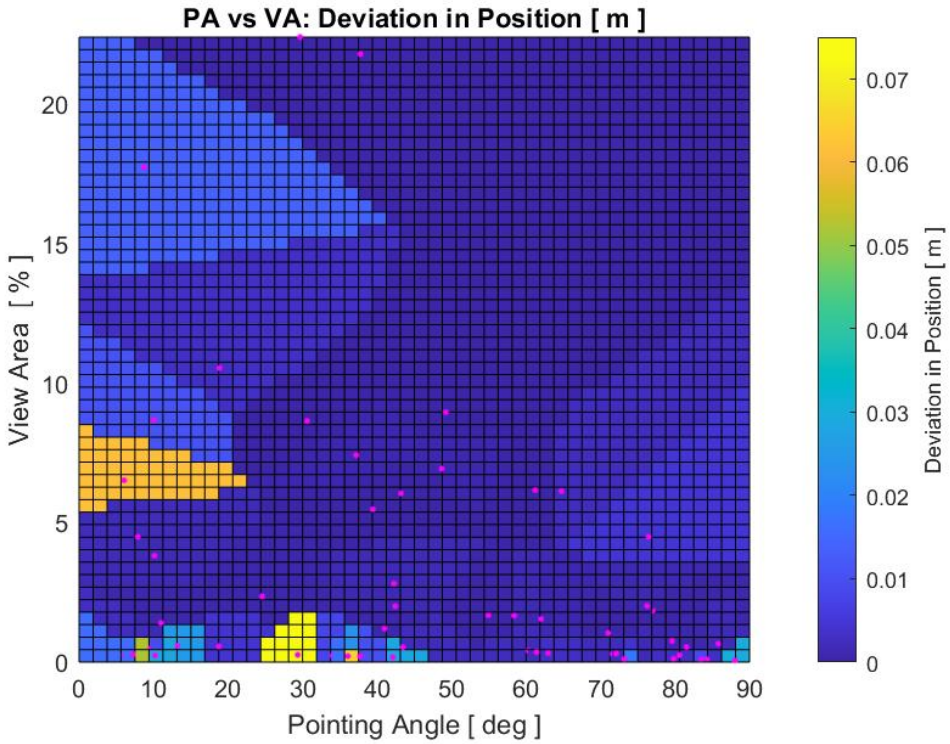

Figure 41: VA vs PA, deviation of the position for validation

5.2 Improvements and modifications

Using the information provided in the analysis of Section 5.1, the table where all measurements are gathered can be used to improve the measuring script in MATLAB. When several markers of the DUT, or the magnetometer, appear within the FOV of the camera at the same time, the script fuses the information given by each marker using a weighting method. This weighting method is based on the orientation of the marker and the camera, which the latter is illustrated in Figure 48. It uses the dot product of the z-axes of the camera and the marker, which are parallel and in opposite direction when the marker is fully facing the camera. Thus, the weighting is assigned based on this negative dot product,

$$w = -z\,axis\_camera \cdot z\,axis\_marker. \tag{14}$$

When the result of this product is 1, the marker is completely facing the camera. On the other hand, when it is 0, the axes are perpendicular and the marker is not detected. For all combinations in between, the weighting would be from 0 to 1. Note that a negative result means that the marker would be facing backwards, as it can be deduced in Figure 48. Hence, in that case, the script discards that marker's information. More details about this weighting method development of the fusemarkers function in the MATLAB script can be found in [2].

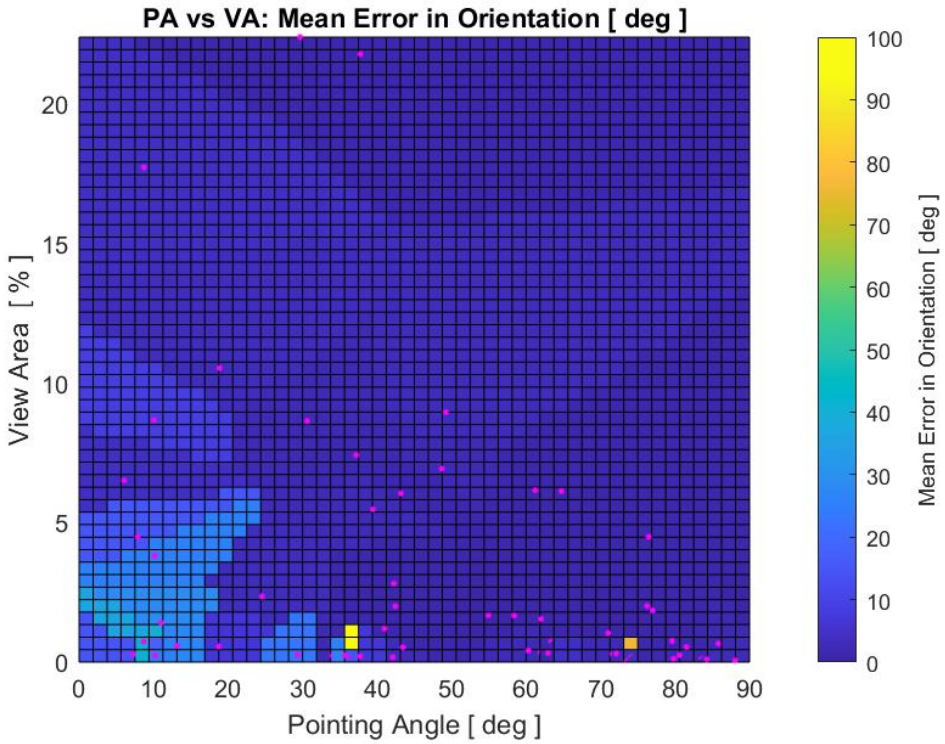

Figure 42: VA vs PA, error in orientation for validation

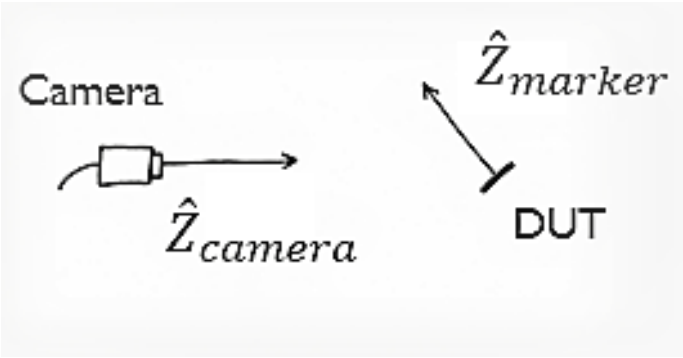

Figure 48: Relationship between the z axes of the camera and the DUT marker

However, after the recent analysis in the accuracy of the system, some poses have less error than the others. Based on the weighting method of the negative dot product, the weighting for the markers does not match the results of the analysis of Section 5.1. Therefore, the heuristics for the multiple marker fusion can be improved using a different weighing method based on the data from the pose analysis of Section 5.1.

A weighting is assigned to each of the markers, one being the highest value corresponding to the lowest error value. Since the accuracy behaviour is different for detecting the position and the orientation, two individual weightings are created for each marker. Thus, the highest weighting for position corresponds to the lowest

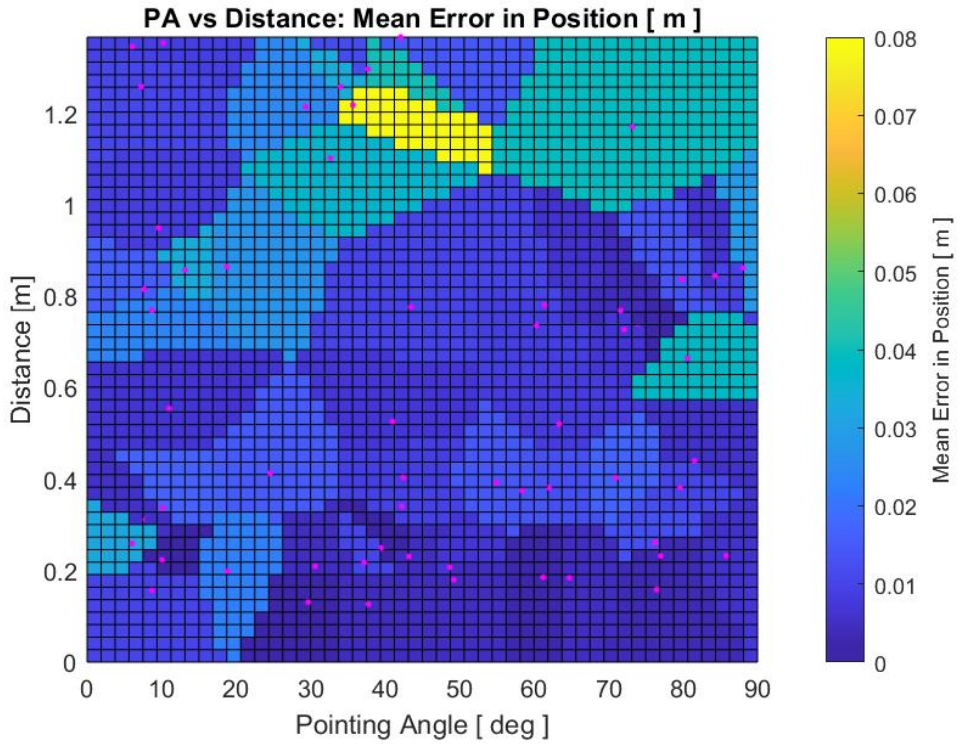

Figure 43: Distance vs PA, error in position using 58 mm x 58 mm markers

mean absolute error value in position; and likewise for the orientation weighting and its mean absolute error. Note that when the marker is not seen and the script does not collect that marker's information, the weighting zero is assigned. Hence, the lowest weighting value that can be assigned to a detected marker is 0.1 corresponding to the highest error shown in the accuracy analysis.

The new weighting method is then used in the modified script assigning the new weights to the markers detected by the camera. Thus, improving the detection of the poses by prioritizing the markers which produce less error. In Algorithm 4, the weighting method is displayed based on the PA and VA extraction and calculation, in order to find the weighting assigned for that specific combination of PA-VA. The implementation includes the calculation of the VA and PA from the camera's detection data as explained in Algorithm 2, and returns the fused multiple marker information. Note that the information provided by the negative dot product is not deleted, so it can be used to discard marker data when the backward-facing error happens.

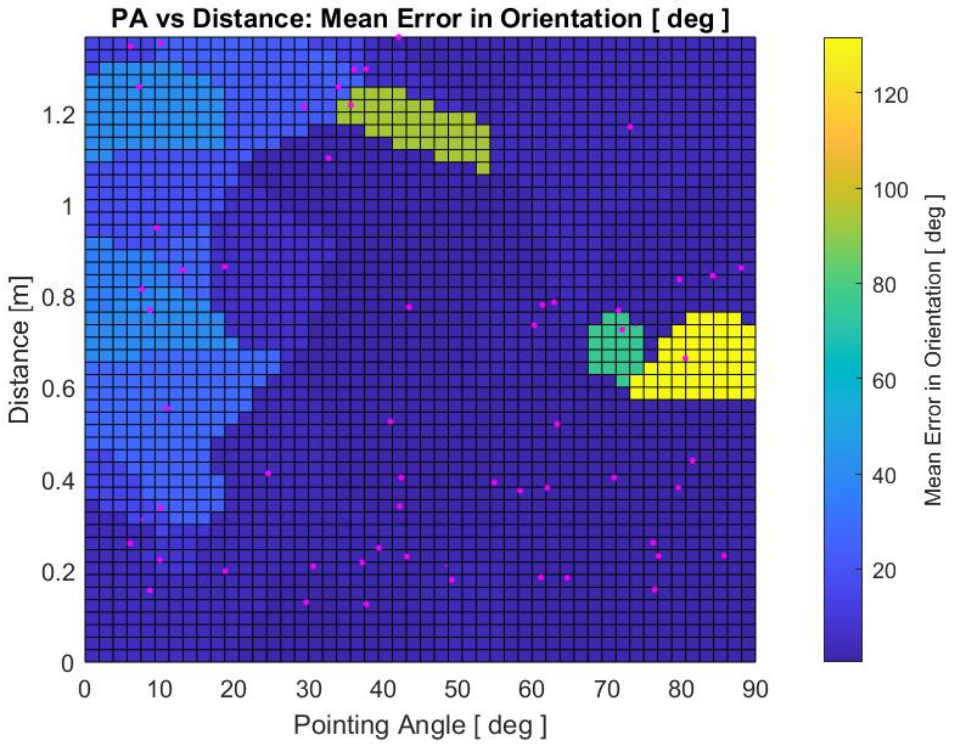

Figure 44: Distance vs PA, error in position using 58 mm x 58 mm markers

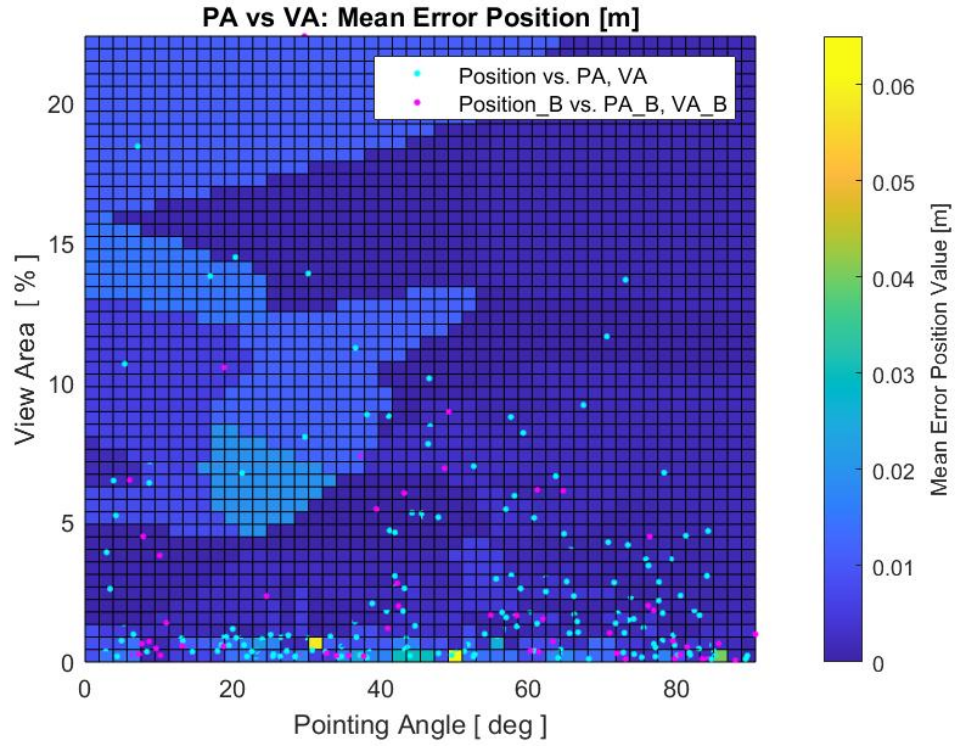

Figure 45: VA vs PA, error in position using data from both marker sizes

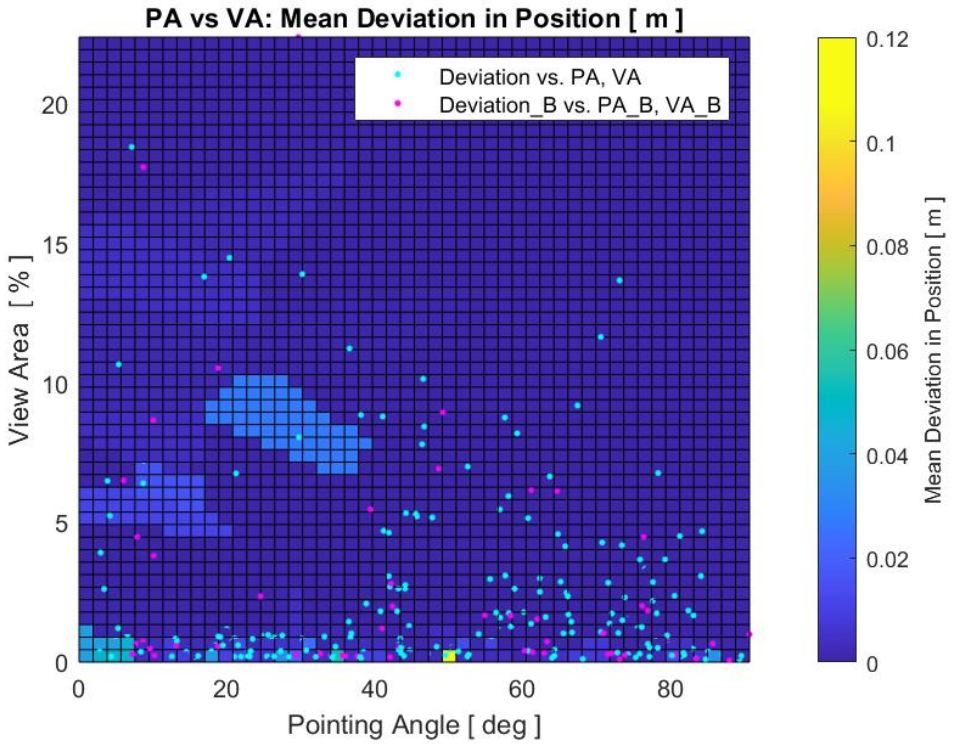

Figure 46: VA vs PA, deviation of the position using data from both marker sizes

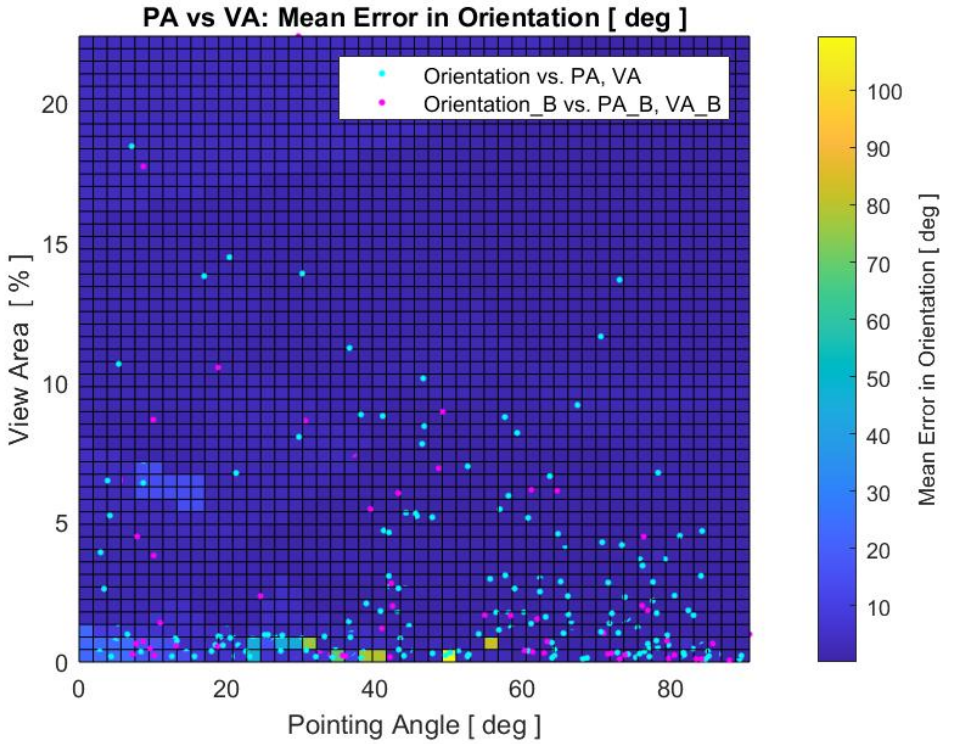

Figure 47: VA vs PA, error in orientation using data from both marker sizes

Algorithm 4 Marker weighting algorithm

```
1: Initialize:  VA = [ ]; PA = [ ]; WeightPos = [ ]; WeightQuat = [ ];
2: Extract: position (pmm) and quaternion (qmm) for each marker detected
3:
4: Calculate VA and PA for each marker:
5: [rows_pmm, ] = size(pmm);
6: for iii = 1 : rows_pmm
7:   [va,pa] = VAPAest(pmm,qmm,iii,marker_length);
8:   VA = [VA; va]; PA = [PA; pa];
9: end
10:
11: Load data table with weightings
12: PQ_weights_DATA = exist('PosQuat_weights','var');
13: if PQ_weights_DATA == 0
14:   load('PosQuat_weights.mat');
15: end
16:
17: Assign new weighting based on the table:
18: for iv = 1:length(VA)
19:   if isnan(VA(iv))
20:     WeightPos = [WeightPos; 0];
21:     WeightQuat = [WeightQuat; 0];
22:   else
23:     [ ,I] = min(sqrt((VA(iv) − PosQuat_weights.VA).^2
24:     +(PA(iv) − PosQuat_weights.PA).^2));
25:
26:     WeightPos = [WeightPos; PosQuat_weights.WeightPosition(I)];
27:     WeightQuat = [WeightQuat; PosQuat_weights.WeightQuaternion(I)];
28:   end
29: end
30: Barckward-facing marker error display:
31: fcDUTmm = rotateframe( conj(qmm(:)),[0 0 1] );
32: walign = -dot( fcDUTmm(:,:), repmat([0 0 1],size(fcDUTmm,1),1), 2 );
33: if any( walign < 0 )
34:   disp('Backward facing marker detected in averaged data.
35:   Discarding one full burst of data.');
36:   trimn = 1; run('TrimMeas_usepackage_pre.m');
37:   clear ii qDUTmm fcDUTmm idfalign trimn
38:   return
39: end
40:
41: Weighting allocation:
42: qmm = qmm.*qoff(1:length(qmm));
43: qm = quaternion( wavg_quaternion_markley( compact(qmm),WeightQuat )' );
44: pmm = pmm - rotateframe(conj(qm),poff(1:size(pmm,1),:));
45: pm = sum(WeightPos.*pmm, 1) / sum(WeightPos);
46:
```

6 Results

In this section results are provided. Adaptations in the code based on the results of the previous section are applied and evaluated in a new set of permanent magnets measurements. A comparison between the new set of measurements and the earlier measurements of Section 4 is also performed in this section. After the evaluation, the test bed is prepared to measure the MDM of the four Engineering Qualification Model (EQM) panels of Foresail-1 using the modified measuring script. Therefore, this chapter is structured as such: Section 6.1 evaluates the new adaptations by verifying the new measurements' results with the ones performed earlier in Section 4; and Section 6.2 presents four measurements of Foresail-1's components using the improved modification, concretely of its four EQM panels.

6.1 Permanent dipole magnets comparison

After the implementation of the new weighting method, explained in Section 5.2, it is worthy to repeat the same dipole permanent magnets measurements in order to see if the modifications made any improvements in the OMTB setup. Therefore, three pairs of new magnetic measurements are performed with the same permanent magnets and location, with the short and long configurations. The magnet's location, the DUT poses, and the camera's placements in each configurations are as similar as possible to the measurements described earlier in Section 4.2. Therefore, a comparison of each of the three magnets is made not only between their own configurations but also between the modified and non-modified script using the weighting method. This latter comparison would be evaluated at the end of Section 6.1.

6.1.1 Validation: permanent magnet E122

The first comparison is performed using the first magnet verified: magnet E122. In this case, the improved script is run with the modifications mentioned in Section 5.2 in order to see if there is an overall improvement in the results. Both configurations are done in the same way as for the measurements in Section 4.2. The location and magnetic properties of the magnet are considered the same as in the previous measurements. In other words, the position and the magnet for its specification values have not been changed for this new set of measurements. The MDM of magnet E122 is given by Equation 10 and its properties are listed in Table 3. Then, the overall comparison of the magnet E122 between the non-modified and modified setups estimation results are compared in Table 10 and Table 11.

Figures 49 - 52 show the estimation of the position and orientation of the magnetic dipole for the magnet E122 in the short and long configurations. As it can be observed from the plots, the estimation is closely related to the estimation plots provided by the non-modified script for the same magnet E122. The MDM vector points in the same direction in all estimation results, the location of the vector is approximately similar and its strength can be considered pretty equal to the previous estimations of the magnet E122 in Section 4.2. Values for these estimations are shown below in Table 10 and Table 11.

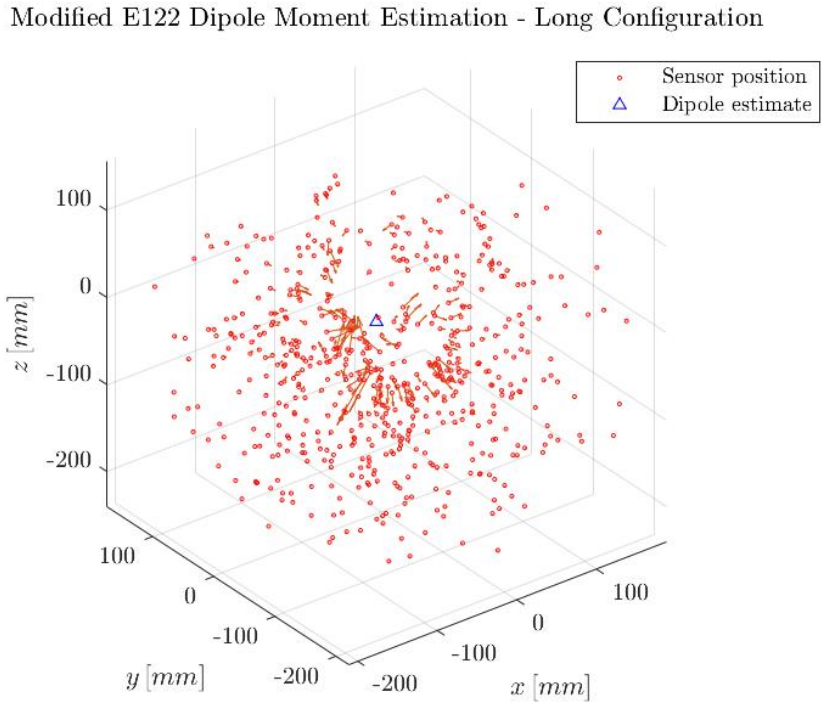

Figure 49: Modified magnet E122 MDM estimation in a long-configuration setup

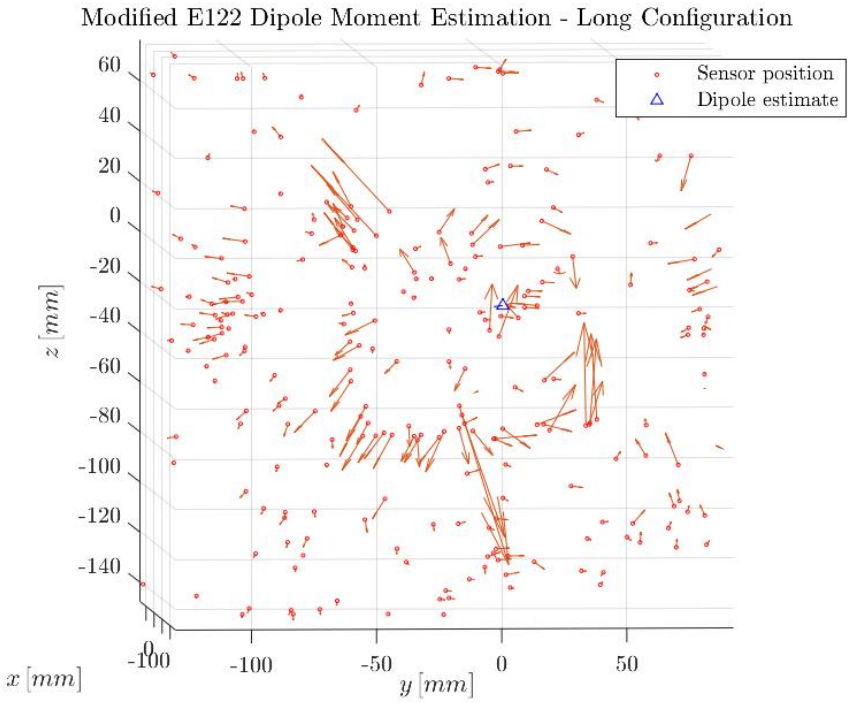

Figure 50: Close-up modified MDM estimation of Figure 49

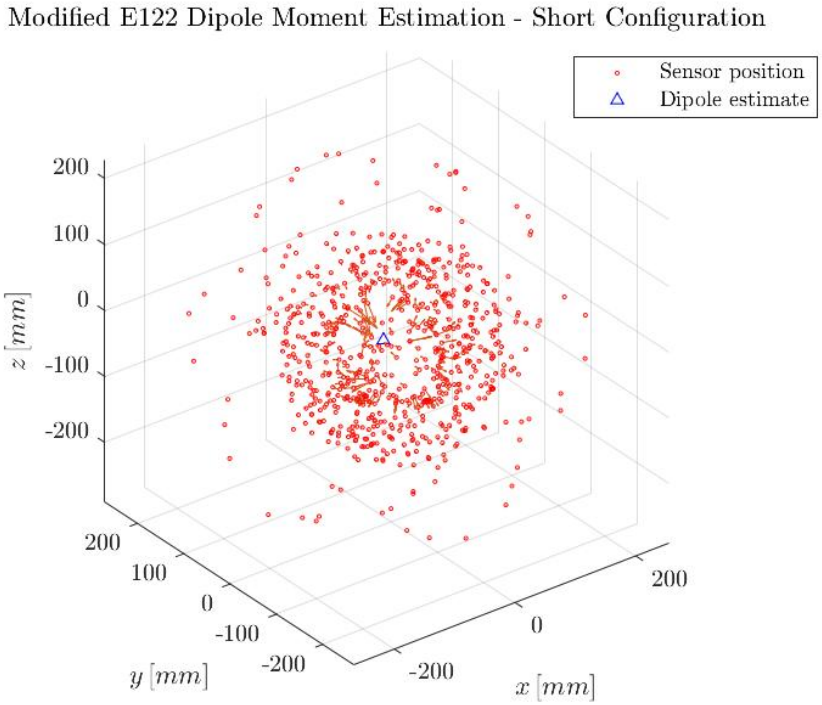

Figure 51: Modified magnet E122 MDM estimation in a short-configuration setup

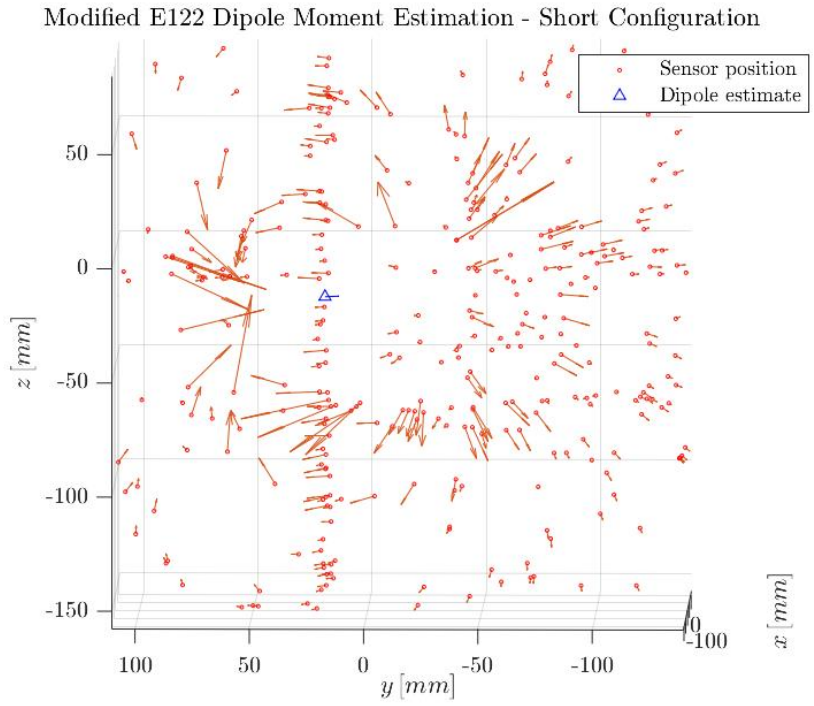

Figure 52: Close-up modified MDM estimation of Figure 51

A comparison of the values between different estimations is displayed in Table 10 and Table 11, for a long and short configurations respectively. For the long configuration, the position in general seems to be better before the modification, except for the x axis. In terms of MDM characteristics, the dipole of the modified measurement is closer to the magnet's specification values. In order to have a clearer picture of the estimation results, the percentage errors are calculated for both configurations. For the long configuration the percentage errors result as follows. A 16.369 % in dipole position and a 15.996 % in MDM magnitude estimation is obtained for the non-modified measurement. Similarly, a 31.640 % in dipole position and a 12.840 % in MDM magnitude estimation is calculated from the modified measurement results. As it can be seen, only the MDM magnitude estimation has been improved for the long configuration.

A similar behaviour is observed for the short configuration, where the non-modified measurement is closer to the specifications values of the magnet E122. For the short configuration, the percentage errors can be calculated as well, using the values given in Table 11. For its non-modified and modified estimations, it can be calculated a 5.483 % in dipole position and a 57.760 % in MDM magnitude estimation; and a 8.688 % in dipole position and a 57.386 % in MDM magnitude estimation, respectively.

Characteristic	**Actual**	**Non-modified**	**Modified**	**Unit**
fGBest	-	1.2580	2.5517	
Position x-axis	0.0000	−0.0018	0.0000	m
Position y-axis	0.0179	0.0143	0.0090	
Position z-axis	−0.0230	−0.0256	−0.0257	
MDM x-axis	0.0000	0.0004	0.0005	$A \cdot m^2$
MDM y-axis	±0.0039	−0.0045	−0.0033	
MDM z-axis	0.0000	0.0002	−0.0004	
MDM magnitude	0.0039	0.0045	0.0034	

Table 10: Magnet E122 comparison results for long-configuration setup

Characteristic	**Actual**	**Non-modified**	**Modified**	**Unit**
fGBest	-	0.3211	0.2797	
Position x-axis	0.0000	0.0012	0.0017	m
Position y-axis	0.0179	0.0186	0.0195	
Position z-axis	−0.0230	−0.0237	−0.0239	
MDM x-axis	0.0000	−0.0006	−0.0005	$A \cdot m^2$
MDM y-axis	±0.0039	−0.0061	−0.0061	
MDM z-axis	0.0000	0.0002	0.0003	
MDM magnitude	0.0039	0.0062	0.0061	

Table 11: Magnet E122 comparison results for short-configuration setup

For these magnet's measurements, it can be said that the error is significantly lower in the short configuration than in the long one except from the estimation of

the position. However, there is no much difference in the results when comparing the modified and non-modified measurement, where the later can be considered closer to the specification values of the magnet E122.

6.1.2 Validation: permanent magnet E317

Similarly, the same procedure is performed for the magnet E317. The location of the magnet E317 in the DUT has not changed compared to the non-modified measurements of Section 4.2. Magnet E317's location components along with the known MDM in each of the three axes are shown in Tables 12 and 13. The following figures, from Figure 53 to Figure 56, show the corresponding estimation results for the location and magnitude of the MDM vector in DUT coordinates.

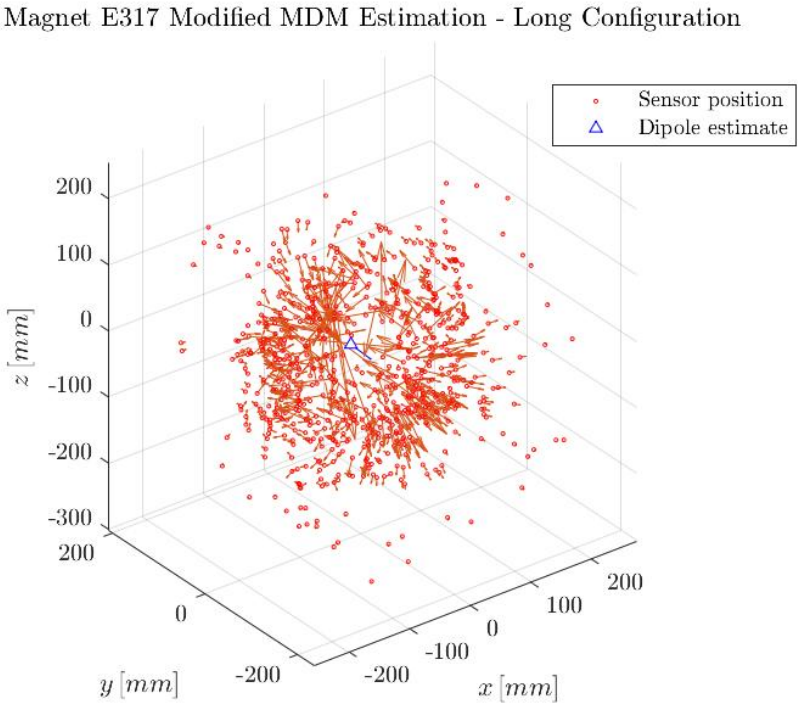

Figure 53: Modified magnet E317 MDM estimation in a long-configuration setup

The aforementioned tables, Table 12 and Table 13, display the values of the results for long and short configurations using the script before and after the modification described in Section 5.2 in order to provide a comparison between them. In this case, for the long configuration, the position is quite similar from one another compared to the specification properties; when it comes to the MDM characteristics, the modified measurement provides a better result based on the actual magnitude of the MDM of magnet E317. For the short configuration, the position, in both non-modified and modified measurements, seems to be also quite similar, where the x axis seem to be more accurate in the non-modified version. The MDM result provided in the modified measurement is clearly closer to the actual value compared to the non-modified one.

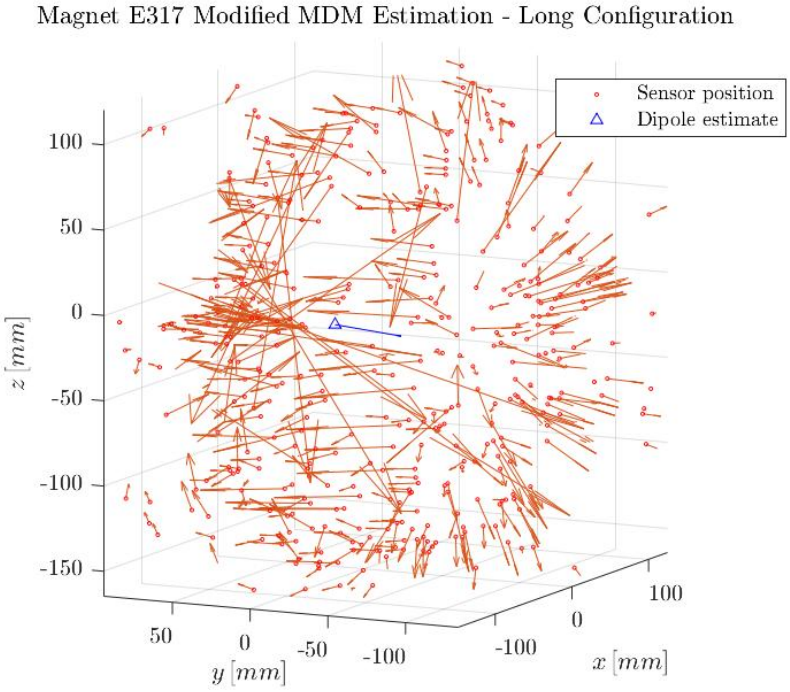

Figure 54: Close-up modified MDM estimation of Figure 53

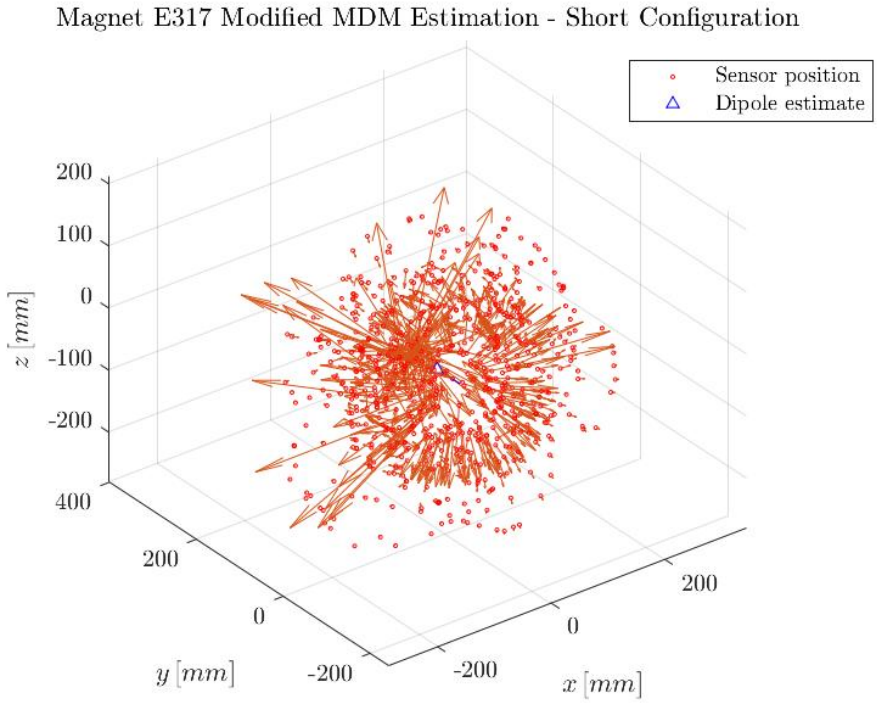

Figure 55: Modified magnet E317 MDM estimation in a short-configuration setup

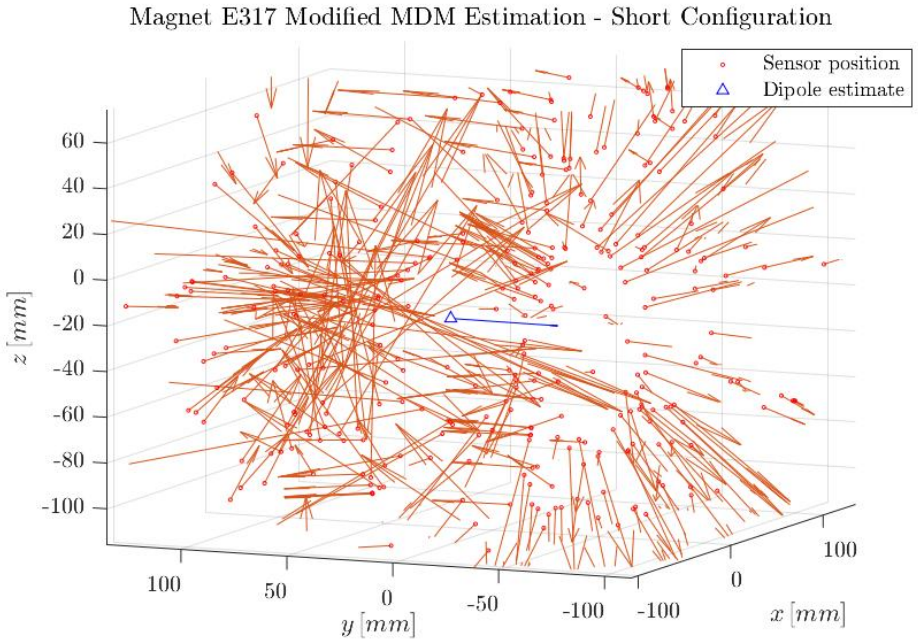

Figure 56: Close-up modified MDM estimation of Figure 55

Characteristic	**Actual**	**Non-modified**	**Modified**	**Unit**
fGBest	-	1.5875	1.3483	
Position x-axis	−0.0011	0.0007	−0.0027	m
Position y-axis	0.0180	0.0176	0.0175	
Position z-axis	−0.0250	−0.0241	−0.0225	
MDM x-axis	0.0000	0.0039	0.0011	$A \cdot m^2$
MDM y-axis	±0.0509	−0.03448	−0.0420	
MDM z-axis	0.0000	−0.0013	−0.0036	
MDM magnitude	0.0509	0.0350	0.0422	

Table 12: Magnet E317 comparison results for long-configuration setup

Characteristic	**Actual**	**Non-modified**	**Modified**	**Unit**
fGBest	-	0.3028	0.2809	
Position x-axis	−0.0011	−0.0023	0.0009	m
Position y-axis	0.0180	0.0205	0.0200	
Position z-axis	−0.0250	−0.0259	−0.0245	
MDM x-axis	0.0000	0.0013	0.0012	$A \cdot m^2$
MDM y-axis	±0.0509	−0.0469	−0.0499	
MDM z-axis	0.0000	−0.0002	−0.0005	
MDM magnitude	0.0509	0.0469	0.0500	

Table 13: Magnet E317 comparison results for short-configuration setup

Based on the information displayed in Table 12 and Table 13 from the measurements of the magnet E317, the percentage errors corresponding for each set of measurements and configurations can be obtained. For the long configuration, its non-modified and modified estimations errors are a 6.622 % in dipole position and a 31.171 % in MDM magnitude estimation; and a 9.708 % in dipole position and a 17.092 % in MDM magnitude estimation, respectively. After evaluating the results, it can be seen that the short configuration provides a more accurate result than the long configuration. When it comes to the modification of the script, both measurements seem to have a similar behaviour in dipole position. In terms of MDM components and magnitude, the modified version is more accurate in both configurations for the magnet E317.

6.1.3 Validation: permanent magnet E200

As a last case, magnet E200 is measured using the modified script. Similarly, the structure of this subsection follows the same procedure as for the magnets E122 and E317, where a comparison in both configurations between the new measurements and the ones described in Section 4.2 is presented as well. The figures from Figure 57 to Figure 60 display the MDM of the magnet E200 in blue. Note that, in this case, the arrows of the MF are considerably bigger compared to the other magnets as the strength of this magnet is the strongest among the measured magnets.

Also, between the short and long configurations the location is the same in the DUT but the orientation of the moment is opposite. This is due to the fact that the magnet was flipped from one measurement to another, since for the long configuration several measurements needed to be undergone. In the results provided for the magnet E200, the dipole vectors is flipped with respect to the short configurations. Nevertheless, the magnet used is the same in both configurations.

The following tables, Table 14 and Table 15, compare the long and short configurations respectively, before and after the modification of the script. Note that the values of the MDM vector and the position of the dipole are displayed, and the orientation of the vector can also be spotted for both configurations. Regarding the long configuration comparison, the estimated position is similar in each case where the non-modified version can be considered slightly closer to the specification values. The MDM characteristics are more accurate in the non-modified version in this case. For the short configuration, the position in both measurements is quite similar where the modified one is closer than the non-modified measurement results in this case. The MDM results can be considered similar, also, the modified measurement is slightly closer to the actual values of the magnet E200,

Overall, the measurements of the magnet E200 are similar in both configurations. Nevertheless, it is worthy to point out also the percentage errors for both configurations and set of measurements. For the long configuration, the percentage errors are obtained. A 7.864 % in dipole position and a 10.37 % in MDM magnitude estimation, for the non-modified measurement, are calculated. In the same way, a 26.880 % in dipole position and a 23.875 % in MDM magnitude estimation, for the modified measurement, are obtained.

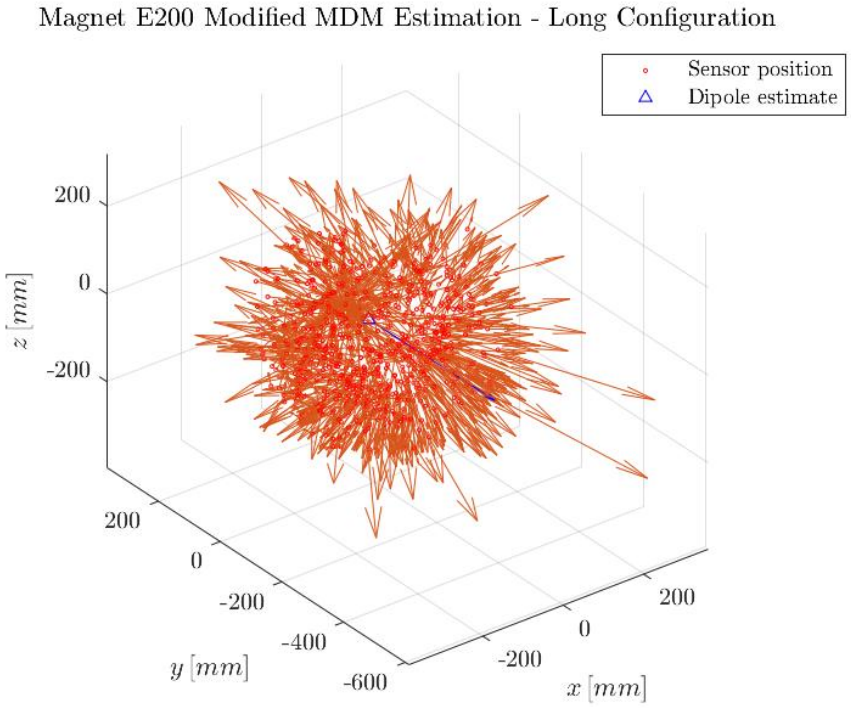

Figure 57: Modified magnet E200 MDM estimation in a long-configuration setup

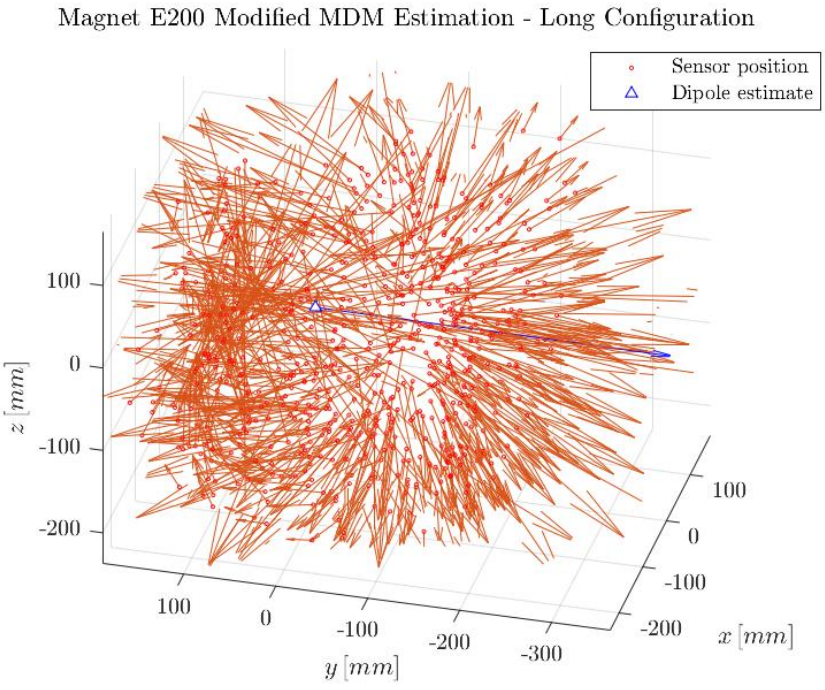

Figure 58: Close-up modified MDM estimation of Figure 57

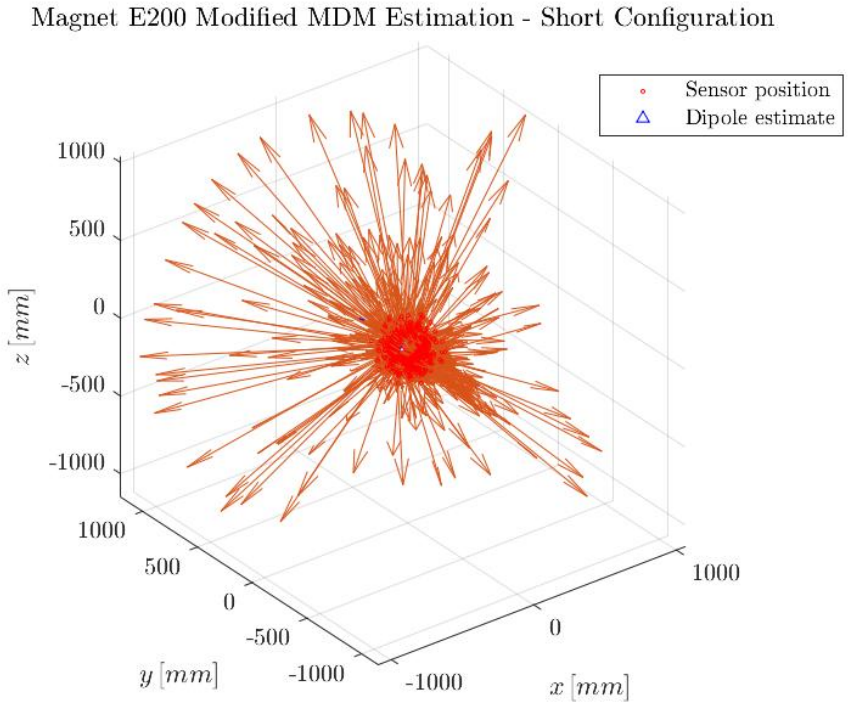

Figure 59: Modified magnet E200 MDM estimation in a short-configuration setup

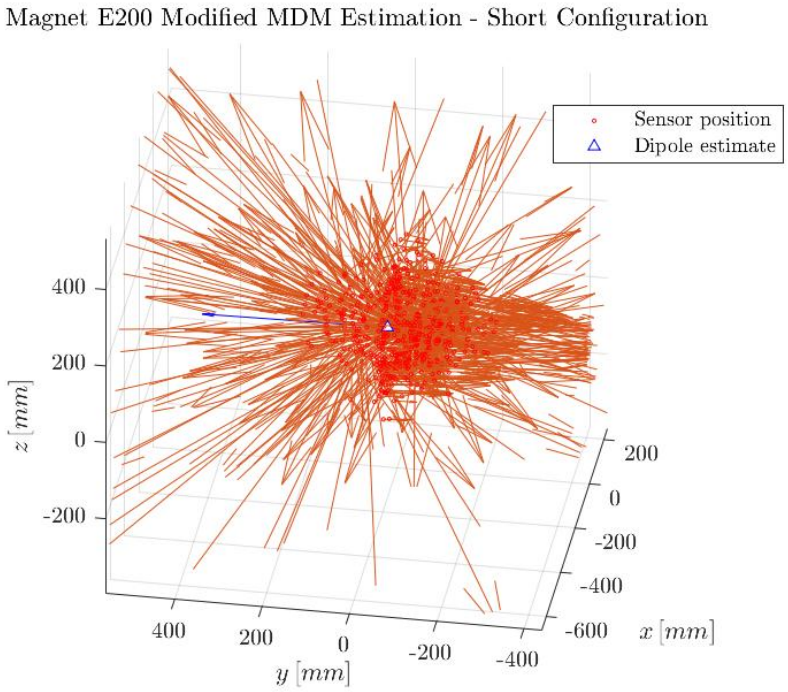

Figure 60: Close-up modified MDM estimation of Figure 59

Characteristic	**Actual**	**Non-modified**	**Modified**	**Unit**
fGBest	-	0.6524	1.3580	
Position x-axis	0.0000	0.0000	−0.0008	m
Position y-axis	0.0195	0.0211	0.0182	
Position z-axis	−0.0250	−0.0269	−0.0334	
MDM x-axis	0.0000	0.0019	0.0162	$A \cdot m^2$
MDM y-axis	±0.5093	−0.4564	−0.3872	
MDM z-axis	0.0000	0.0064	−0.0126	
MDM magnitude	0.5093	0.4565	0.3877	

Table 14: Magnet E200 comparison results for long-configuration setup

Characteristic	**Actual**	**Non-modified**	**Modified**	**Unit**
fGBest	-	0.6075	0.4231	
Position x-axis	0.0000	0.0041	−0.0018	m
Position y-axis	0.0195	0.0152	0.0219	
Position z-axis	−0.0250	−0.0263	−0.0282	
MDM x-axis	0.0000	0.0627	0.0079	$A \cdot m^2$
MDM y-axis	±0.5093	0.3986	0.4258	
MDM z-axis	0.0000	−0.0210	−0.0103	
MDM magnitude	0.5093	0.4041	0.4260	

Table 15: Magnet E200 comparison results for short-configuration setup

In the case of the short configuration, similar calculations can be done, the percentages errors for the non-modified and modified measurements. A 19.25 % in dipole position and a 20.663 % in MDM magnitude estimation are calculated for the non-modified measurement. Likewise, a 13.700 % in dipole position and a 16.363 % in MDM magnitude estimation are obtained for the modified measurement.

Note that the modified version of the short configuration and the non-modified measurement of the long configuration seem to have the best results. For this magnet's measurements, the four measurements described in this section and Section 4.2 were not enough to cross check the estimation results, but several additional measurements were required. This could be caused by the magnet itself which could be out of specification, explaining the non-expected behaviour from the results in most of the additional measurements. The dimensions and strength of the magnet E200 used were checked before taking any of the measurements. The magnet E200 was the same during all magnetic measurements. Concluding, the results can be considered correct for this case, however, a different magnet E200 should be use in order to cross-check the results for its future validation.

6.1.4 Summary: permanent magnets measurements

After presenting the comparison between the results of different measurements and configurations, some trends regarding the modifications and the type of configuration

can be seen. In this subsection, some key aspects and overall analysis is carried out in order to have a wider understanding of the system's behaviour based on the performed measurements.

In terms of configurations, it can be observed that the long configuration provides a more accurate overall results. However, in dipole position and MDM, as it has been stated, the specification values of each of the magnets are closer to each other in the short configuration. Regarding the modification of the script, in general the difference between the different positions estimated in each of the non-modified measurements is quite similar. However, it can be said that the modified script provides better results when it comes to MDM estimation characteristics.

In order to see the improvement in the estimation results clearer, the average percentage error for both configurations based on the last three measurements using the modifications are calculated: avg. of 20.4 % in dipole position and 17.9 % in dipole moment, for the long configuration; and avg. of 10.6 % in dipole position 25.2 % in dipole moment, for the short configuration. Compared to the non-modified ones, the modification of the weighting method has improved 2 % the estimation results in general.

Using these last results, it can be said that the system has an overall percentage error of the MDM position and moment estimation results of 13 % and 23 %, respectively. Also, the absolute mean errors can be also calculated based on this study, which are $0.004 \pm 9 \cdot 10^{-7}$ m for the position estimation; and $0.007 \pm 1 \cdot 10^{-4}$ A $\cdot$ m^2 for the estimation of the MDM. For the absolute error calculation, the procedure presented in Algorithm 3 can be applied.

6.2 Foresail-1 components: magnetic dipole moment

In this subsection, the Foresail-1 components analysed are the four solar panels with the magnetorquer attached in each one of them. In this case, a voltage is provided to the coil in order to generate a current loop, producing the MF of the magnetic torquer for being able to analyse its MDM by using the OMTB presented in this thesis.

In order to analyse these components, the panel's design with its magnetorquer coil is displayed in the following figures, Figure 61 (a) and Figure 61 (b). The four panels are referred as x- and y- with plus or minus depending on its location in Foresail-1 satellite. Note that all panels except for y-minus have the same design as shown in Figure 61 (a). Y-minus panel is also displayed, the difference in the design is small but it can be seen in Figure 61. This figure also displays the location of the magnetorquer coil for each panel. The dimensions of the panels are: width of 82 mm, depth of 1.6 mm, and height of 324.5 mm.

(a) X-plus panel (b) Y-minus panel

Figure 61: Foresail-1 EQM panels configuration at Aalto University Space Laboratory

Taking into account the dimensions of the panel and its magnetorquer coil, a harness has been in designed in OpenSCAD in order to protect the panel and cover it with several markers all around. The markers cover all faces of the panel's harness, 14 in total. In this case, these markers are bigger, providing a more accurate result since the VA at the same distance as the PLA cube would be bigger. The location and orientation of the markers on the harness for the EQM panels can be seen in Figure 63. The origin of the DUT harness is the marker 7, which is the closest one to the camera, with x = 0, y = 0 and z = 0. The rest of the markers' origin are defined based on the distances to marker 7; which location is in the middle of the harness' width and depth, and at the end of its height. Harness dimension in width, depth and height are 120, 60, and 362.5 mm respectively. These component values defined are described in a coordinate frame where the origin is place one of its bottom corners when the harness bottom is the smallest face area, and the z axis of this coordinate frame corresponds to the largest side of the harness.

Regarding the magnetometer, a harness has been also designed so it can have markers in three more faces, seven in total. This is important for the measurements, since the DUT can cover some of the magnetometer's markers. In the permanent magnet measurements, only the marker 0 was used for the magnetometer but for the

new analysis more markers are visible from the magnetometer. This enables the system to take readings from DUT poses which before covered the only magnetometer's marker, and now at least other markers from the magnetometer are detected and the measurement can be smoother. In Figure 62, the location and orientation of the markers for the harness of the magnetometer are illustrated. The origin (0, 0, 0) of the magnetometer harness is defined where the magnetometer is placed. Therefore, based on the marker 0 location in the permanent magnet measurements which is (0.5, 8, 40.1) mm, the rest of the markers for the new measurements can be defined. Note that these harnesses also protect the devices from possible accidents during the measurement.

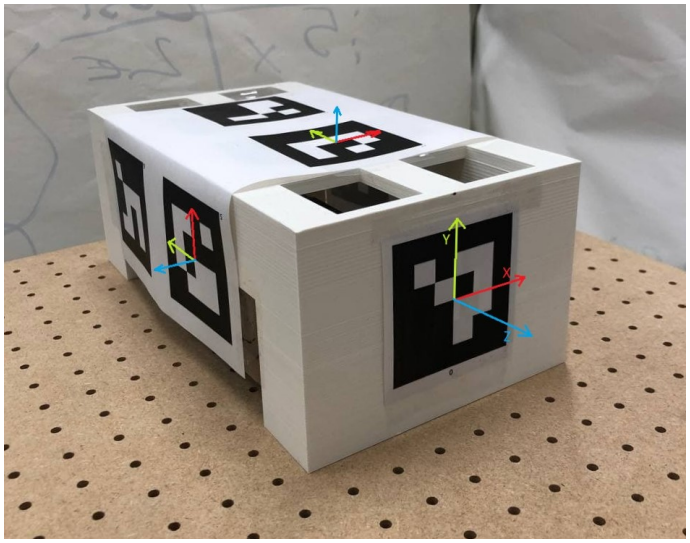

Figure 62: Magnetometer harness orientation and axes

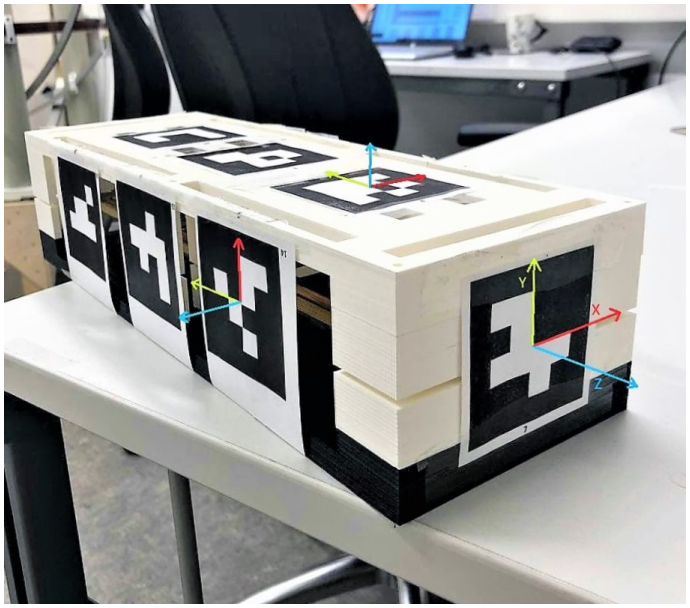

Figure 63: Magnetorquer panel's harness orientation and origin

As it has been stated earlier, a voltage is applied to the coil so it can generate a current loop, producing a MF. This will enable the system to estimate the MDMs of the four panels. The voltage is applied through two pins, P and N, which can be seen in Figure 61 at the inner part of the coil, middle-left side of the board. Therefore, 3.6 volts are input by the power supply in these two pins, which a current loop of 55 mA can be observed directly in Figure 64. The voltage chosen is simulating the maximum voltage that the coil of the magnetic torquer would receive during Foresail-1 space mission. All four panels have been measured with the same voltage and current by soldering a curled cable on those pins before introducing them inside the harness.

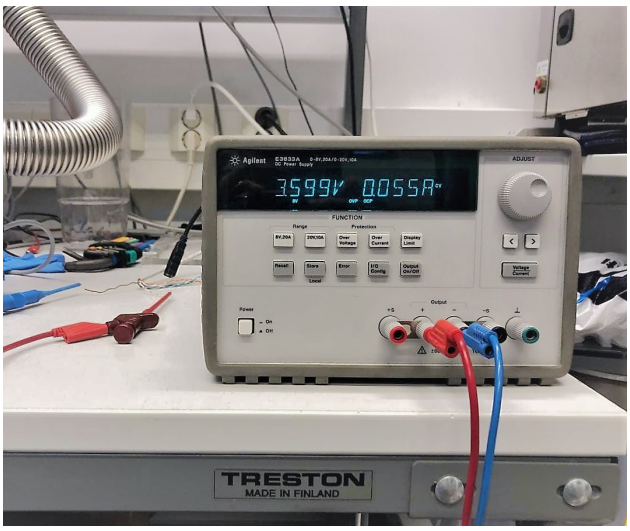

Figure 64: Magnetorquer panel's voltage and current source

Once the panels are prepared inside their harness, each one of the panels has been measured using the the OMTB, one at a time using the same marker definition in the MATLAB script and procedure for all of the measurements. The DUT, the panel harness in this case, is placed in different configurations while the system reads the MF at that position and orientation based on the detection of the markers and readings from the magnetometer. For their post-processing, the number of dipoles for the estimation is an unknown but required variable for the generation of the magnetic dipole vectors. As the panel is not a single permanent magnet, a certain number of dipoles needs to be assumed for the estimation analysis. Therefore, the fGBest value has been evaluated from one dipole to four dipoles estimation. This value describes how well the estimated MF fits the measured one. More details of this term can be found in [2].

Assuming number of dipoles from one to four, when three dipoles were assumed the value targeted was less than for the rest of other number of dipoles. The fBGest for each number of dipoles obtained by the estimation algorithm for the four measurements can be seen in Table 16, where biased and unbiased data sets are shown for each of the measurements. The unbiased set includes the measurement before removing the ambient MF, read by the magnetometer inside the cage, and the biased one refers to the removed ambient MF data set results. In both cases,

and for all the measurements, the fGBest values are not affected considerably by this residual MF; since they are quite small. Note that, for the following study of these measurements, the unbiased data set is displayed.

As it has been mentioned earlier, three dipoles are assumed for the estimation. The tables below show the values of their MDMs characteristics, the position of the dipoles are described based on their distance to the marker 7. Estimation plots for the panels x-minus and -plus, followed by y-minus and -plus, are presented from Figure 65 to Figure 68. As well as the features of the MDMs for each magnetorquer from Table 17 to Table 20.

Magnetorquer panel		**1 Dipole**	**2 Dipoles**	**3 Dipoles**	**4 Dipoles**
X-minus	**biased**	1.918817	0.664322	0.490935	0.509607
	unbiased	1.920083	0.663691	0.503688	0.566326
X-plus	**biased**	2.171727	0.546372	0.444017	0.455221
	unbiased	2.174578	0.544587	0.442409	0.573077
Y-minus	**biased**	2.936402	0.744647	0.480160	0.480198
	unbiased	2.940946	0.743665	0.489300	0.498814
Y-plus	**biased**	1.900145	0.437905	0.342077	0.356239
	unbiased	1.897539	0.439767	0.336551	0.432593

Table 16: Values of fGBest for different number of dipoles for each magnetorquer

As it can be seen in Tables 17 - 20, the MDMs magnitude of the three dipoles for all four panels is similar. It can be found that for the pair of x panels the values are even more similar, and also for the other pair of y panels between themselves. In general, the MDM magnitudes of the three dipoles are around 0.0364, 0.0409, and 0.0432 $A \cdot m^2$ in all four panels. Note as well that for the dipole with a similar MDM magnitude corresponding another panel, the position estimated is also close in their relative panel between those dipoles. Except for the panel y-minus, where the position of its magnetorquer coil is lower compared to the others. Therefore, it can be said that the panels and measurements show a strong correlation between each other, given the same design parameters and voltage applied. The small difference between the values is affected by the external factors in a real environment, or by the specifications of each panel, which is impossible to have all four panels with the exact same copy in all aspects.

Considering the plots where the MDMs are shown in the DUT frame, it can be seen that the orientation, location and strength are consistent for all four panels. The figures for each of the pairs show opposite direction of the MDM vectors, as expected. Note also that the measured MF vectors are logically related with the panel configuration and magnettorquer coil in all four measurements. In addition, the measured MF observed in the estimation plots behaves as expected in all four panels.

Estimated feature	Magnetorquer estimated dipoles			
	Dipole 1	**Dipole 2**	**Dipole 3**	**Unit**
Position x-axis	0.0093	-0.0061	-0.0092	m
Position y-axis	-0.0031	-0.0005	0.0058	
Position z-axis	-0.1919	-0.1107	-0.2847	
MDM x-axis	-0.0018	-0.0004	0.0042	$A \cdot m^2$
MDM y-axis	0.0330	0.0440	0.0407	
MDM z-axis	-0.0010	0.0006	0.0001	
MDM magnitude	0.0330	0.0440	0.0409	

Table 17: Estimated values for position and MDM for x-minus magnetorquer

Estimated feature	Magnetorquer estimated dipoles			
	Dipole 1	**Dipole 2**	**Dipole 3**	**Unit**
Position x-axis	-0.0029	0.0048	-0.0021	m
Position y-axis	0.0000	-0.0024	0.0002	
Position z-axis	-0.1045	-0.1874	-0.2701	
MDM x-axis	-0.0005	0.0002	-0.0006	$A \cdot m^2$
MDM y-axis	-0.0437	-0.0361	-0.0418	
MDM z-axis	-0.0003	0.0002	0.0000	
MDM magnitude	0.0437	0.0361	0.0418	

Table 18: Estimated values for position and MDM for x-plus magnetorquer

Estimated feature	Magnetorquer estimated dipoles			
	Dipole 1	**Dipole 2**	**Dipole 3**	**Unit**
Position x-axis	0.0040	0.0022	-0.0019	m
Position y-axis	0.0032	0.0013	0.0027	
Position z-axis	-0.2858	-0.1199	-0.1953	
MDM x-axis	0.0007	0.0002	-0.0006	$A \cdot m^2$
MDM y-axis	0.0365	0.0404	0.0425	
MDM z-axis	0.0008	-0.0021	-0.0008	
MDM magnitude	0.0365	0.0405	0.0425	

Table 19: Estimated values for position and MDM for y-minus magnetorquer

Estimated feature	Magnetorquer estimated dipoles			
	Dipole 1	Dipole 2	Dipole 3	Unit
Position x-axis	-0.0057	0.0033	-0.0007	m
Position y-axis	0.0031	-0.0014	-0.0010	
Position z-axis	-0.2782	-0.1929	-0.1027	
MDM x-axis	-0.0005	0.0023	-0.0014	$A \cdot m^2$
MDM y-axis	-0.0403	-0.0426	-0.0399	
MDM z-axis	0.0007	-0.0002	-0.0011	
MDM magnitude	0.0403	0.0426	0.0399	

Table 20: Estimated values for position and MDM for y-plus magnetorquer

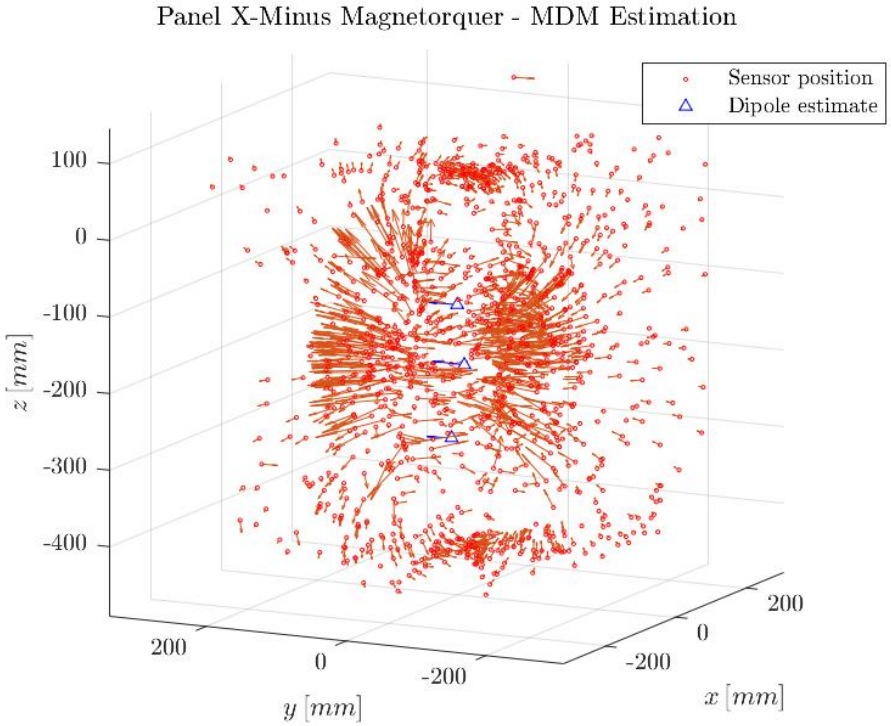

Figure 65: MDM estimation - magnetorquer in x-minus panel measurement

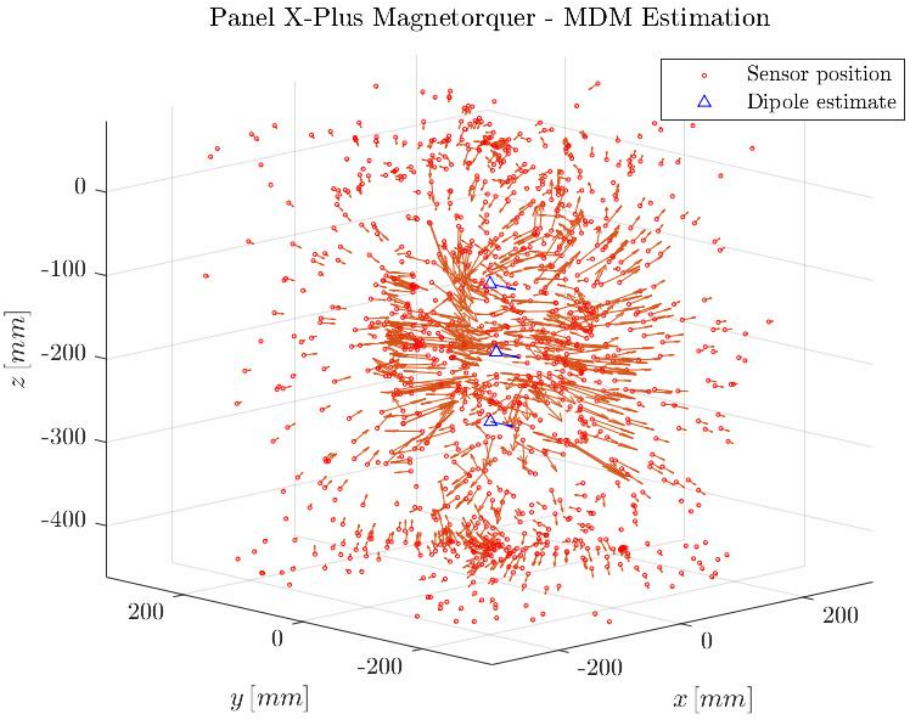

Figure 66: MDM estimation - magnetorquer in x-plus panel measurement

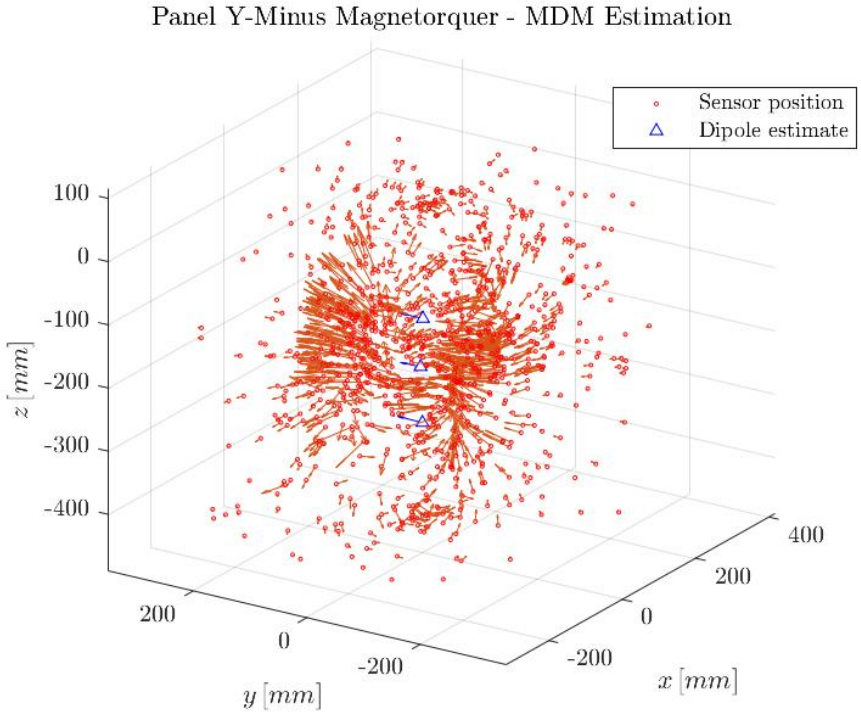

Figure 67: MDM estimation - magnetorquer in y-minus panel measurement

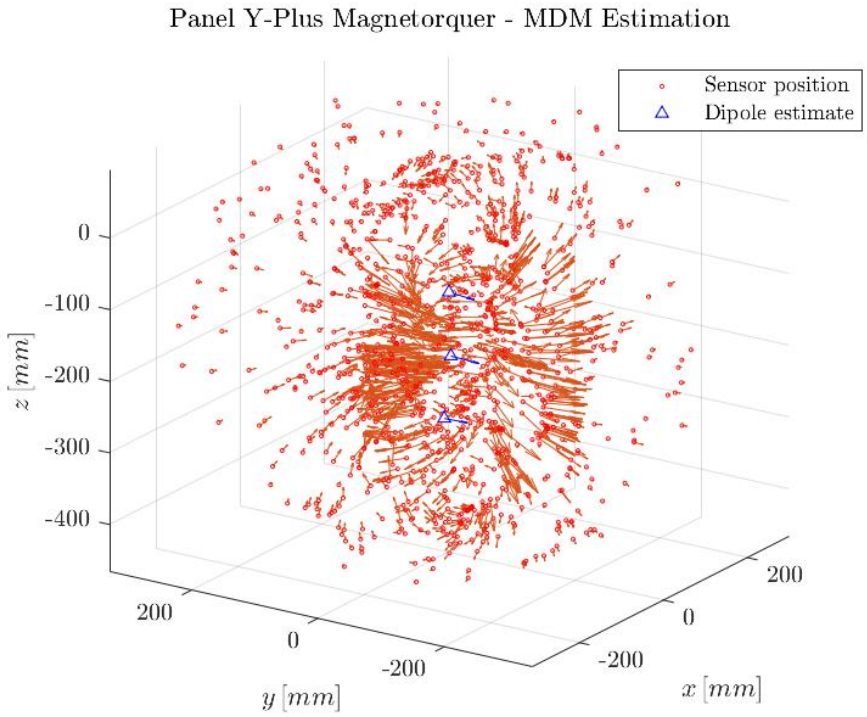

Figure 68: MDM estimation - magnetorquer in y-plus panel measurement

7 Conclusions

This thesis focuses on the optical test bed used at Aalto University Space Laboratory, which data acquisition process is automated using machine vision. The purpose of this thesis is to asses this optical test bed, improve its performance if possible, and characterize the magnetic dipole moment of Foresail-1's components.

In Sections 1 - 3, the key concepts of the test bed and its components, followed by the process of taking a magnetic measurement, are explained. The Helmholtz cage generates a magnetic field-free region in which the device for testing and the magnetometer are placed in order to start the measurement. The data acquisition is performed by a smart camera which recognises the markers inside the cage, providing the poses of both the device under test and the magnetometer. Then, the measuring MATLAB scripts provide the data acquired with a plot of the measured magnetic field in the DUT coordinates. Finally, an optimization algorithm is used to estimate the pose and characteristics of the dipole moments of the tested device based on the measured magnetic field.

In order to assess this optical test bed, the first set of measurements is performed using three different permanent magnets for which the dipole moment characteristics and dimensions are known, along with the location of the magnets on a 3D-printed cube. Three pairs of measurements in a short and long configuration are then taken in order to see if the distance between the camera and the cube affects the estimation results. After evaluating the results in Section 4, the short configuration is found to be faster in the data acquisition process than the long one. However, the long configuration was more accurate with an average error of approximately 10 % in the dipole position estimation and 20 % for the dipole magnetic moment estimation. It has been also observed that the magnetic field inside the cage is not exactly zero, and can vary throughout the measurement depending on the external conditions in the laboratory. In some poses of the printed cube markers are not detected at all, or the detection is not stable and blinks, or the orientation detected is not stable and flips.

Based on the observations after the first measurements, the ambient magnetic region is subtracted from the data points. The poses of the markers were analysed thoroughly in Section 5.1 by placing different markers in a flat surface with a known pose. The mean absolute error in the detection with different poses is calculated and evaluated based on different combinations of view areas and pointing angles for two marker sizes, 37.7 mm x 37.7 mm and 58 mm x 58 mm. The difference in size does not affect the behaviour since the above-mentioned variables are independent from the size of the markers. The mean absolute error and deviation in the position and the mean absolute error in the orientation of the markers are 0.05 ± 0.005 m and 5 degrees, respectively. The detection is more accurate for poses where the marker is closer to the camera and does not face fully the camera. Heat maps for all the errors are generated, showing a consistent pattern where the detection is more accurate based on the combination of the view area and pointing angle of the detected marker. Using these error results, the weighting method of the measuring MATLAB script has been changed, as described Section 5.2, when detecting several markers at the

same time. A function that extracts the view area and the pointing angle of the marker has been implemented in the weighting method, giving a higher weight to the marker poses which show higher accuracy in the heat maps. Thus, prioritizing the markers that are detected more accurately.

To evaluate any improvements in the optical test bed, the modification of the weighting method is used in another set of measurements with the same three permanent magnets, and the same two camera configurations (long and short). Thereafter, the estimation results of three pairs of measurements are analysed in Section 6.1 by using the modified script and compared to the earlier magnetic measurements without the modification. For the modified measurements in the long configuration, the average percentage error in dipole position estimation approximately 20 % and, in dipole moment estimation it is 18 %. In the case of the short configuration, a 10 % in dipole position estimation and 25 % in dipole moment estimation are obtained. Based on these results, all the aspects have not been improved. However, it can be concluded that the modification has improved the estimation results of the test bed by a 2 %. In addition, this test bed estimates the dipole position and moment with an overall percentage error of 13 % and 23 %, respectively. The overall mean absolute errors for the dipole position and estimation are also calculated, and they are $0.004 \pm 9 \cdot 10^{-7}$ m and $0.007 \pm 1 \cdot 10^{-4}$ A $\cdot$ m^2, respectively.

To characterize the dipole moment, an estimation of the magnetic moment properties of the four panels of the Foresail-1 engineering qualification model is performed with the improved data acquisition method. Two harnesses are designed and 3D printed for the magnetometer and the panel to be measured. The harnesses provide more available surfaces to place the markers in all faces, and protect both components from accidents. In these four measurements, the markers used are bigger than in the permanent magnet measurements, since higher view angles are detected more accurately. After evaluating the results in Section 6.2, the optical test bed estimates consistently a three dipole configuration for all the panels' magnetorquers. The position estimation and dipole moment estimation are also coherent with the engineering model display and voltage input. The voltage input is 3.6 V for all four panels, giving a current of 55 mA through the magnetorquer. The positions of the three dipoles in each magnetic torque are displayed at the center of the magnetorquer along the z axis, as expected. In all four panels, the estimated magnitudes of the three dipoles are approximately 0.0364, 0.0409, and 0.0432 A $\cdot$ m^2.

To summarize, this thesis has assessed the optical magnetic test bed of Aalto University by performing several measurements on different permanent magnets. In addition, the estimation results of these measurements and specification values of the three permanent magnets are verified. Based on the measurements, the accuracy of the different poses of the device under test has been studied which made possible to change the weighting method of the system. This modification was evaluated in new measurements using the same magnets, which show an improvement on the overall estimation results. The improved setup is then used to characterize the magnetic dipoles of the four engineering qualification model panels of Foresail-1 satellite. The estimation results of the panels' magnetorquers are coherent, and the test bed is able to characterize accurately the magnetic dipole moments of small satellites.

Further work

After evaluating the optical test bed, there are some aspects and considerations that could be worked in the future in order to further improve the estimation results:

1. When performing the measurements, an automated method for cancelling the ambient magnetic field inside the Helmholtz cage would save time of the measurement. Considering external factors, the laboratory can be magnetically cleaner so that the ambient magnetic field is not affected by the surroundings, since this magnetic field can modify the data and generate wrong measured points (outliers).

2. For the detection of the markers, a better filtering for the outliers due to blinking or flipping problems in the detection would provide a more accurate magnetic dipole moment characterization. The possibility of using more smart cameras in different angles and positions, or use other visual detection systems on the device under test or the magnetometer, shall be considered for future measurements.

3. Regarding the manipulation of the device that is tested, or the magnetometer, the process can be automated in order to have more stable poses when measuring and reducing the overall time of a measurement. In this way, the camera could detect the markers more accurately, hence, improving the estimation results of the magnetic dipoles.

References

[1] T. Villela, C. A. Costa , A. M. Brandão, F. T. Bueno, and R. Leonardi. Towards the thousandth CubeSat: a statistical overview. Review Article. *International Journal of Aerospace Engineering*, Vol. 2019, Article ID 5063145. DOI: https://doi.org/10.1155/2019/5063145

[2] B. A. Riwanto Calibration and testing techniques for nanosatellite attitude system development in magnetic environment. Doctoral thesis. *Aalto University. School of Electrical Engineering.* Year 2021, Accessed online on Jun. 2021, URL: http://urn.fi/URN:ISBN:978-952-64-0460-8

[3] A. Lassakeur, C. Underwood, B. Taylor, and R. Duke . Magnetic cleanliness program on CubeSats and nanosatellites for improved attitude stability. *Journal of Aeronautics and Space Technologies*, Vol. 13, No. 1, pp. 25-41, Jan. 2020. (ISSN : 1304-0448)

[4] T. Inamori, N. Sako, S. Nakasuka. Magnetic dipole moment estimation and compensation for an accurate attitude control in nano-satellite missions. *Acta Astronautica. ELSEVIER*, Dec. 2010, DOI: 10.1016/j.actaastro.2010.10.022

[5] NASA. Spacecraft magnetic torques. *NASA Space Vehile Design Criteria (Guidance and Control)*, 3510 NASA SP-8018, Mar. 1969, Appendix B: Techniques for measuring spacecraft magnetic properties. Accessed online on Jun. 2021, URL: http://www.dept.aoe.vt.edu/ cdhall/courses/aoe4065/NASADesignSPs/sp8018.pdf

[6] M. S. Farissi, S. Carletta, A. Nascetti and P. Teofilatto, Implementation and hardware-in-the-loop simulation of a magnetic detumbling and pointing control based on three-axis magnetometer data. Article. *MDPI, Aerospace*, Year 2019, 6, 133; DOI:10.3390/aerospace6120133

[7] M. Boghosian, P. Narvaez, R. Herman. Magnetic testing, and modeling, simulation and analysis for space applications. *27th Aerospace Testing Seminar*, Oct. 2012, Accessed online on Jun. 2021, URL: https://trs.jpl.nasa.gov/bitstream/handle/2014/43197/12-5590_A1b.pdf?sequence=1isAllowed=y

[8] I. Turer and L. Sevgi DC magnetic compatibility of satellites. *IEEE.* Accessed online on Aug. 2021, URL: http://www.emcturkiye.org/papers/Session8_Talk3.pdf

[9] A. Nicolai, Magnetic field mitigation strategies towards a magnetically clean reaction wheel. Doctoral Thesis. *Berlin University of Technology (Technische Universität Berlin).* Year 2021. DOI: http://dx.doi.org/10.14279/depositonce-12030

[10] J. C. Springmann, J. W. Cutler and H. Bahcivan. Magnetic sensor calibration and residual dipole characterization for application to nanosatellites. *AIAA/AAS Astrodynamics Specialist Conference. American Institute of Aeronautics and Astronautics*, Aug. 2016, Accessed online on Aug. 2021, URL: http://arc.aiaa.org , DOI: 10.2514/6.2010-7518

[11] M. de Soria-Santacruz, M. Soriano, O. Quintero, F. Wong, S. Hart, M. Kokorowski, B. Bone, B. Solish, D. Trofimov, E. Bradford, C. Raymond, P. Narvaez, R. Oran, B. P. Weiss, K. Ascrizzi, C. Keys, P. Lord, C. Russell, and L. Elkins-Tanton. An approach to magnetic cleanliness for the psyche mission. *Jet Propulsion Laboratory. IEEE Xplore*, Oct. 2020, Accessed online on Jun. 2021, URL: https://static1.squarespace.com/static/56d74e9c4c2f85996d16a562/t/5f8052ab86feca1a363b91b8/1602245293942/deSoria-Santacruz_2020_IEEE.pdf

[12] S. Belyayev, N. Ivchenko, F. Dudkin3 and V. Pronenko. Practical analysis and implementation of a low magnetic contamination CubeSat platform. Conference Paper, T*he 4S Symposium 2016 – S. Belyayev*. Accessed online on Aug. 2021, URL: https://www.researchgate.net/publication/330933960

[13] S. Weikert, K. Mehlem and A. Wiegand. Spacecrat magnetic cleanliness prediction and control. *ESA Workshop on Aerospace EMC*, Italy, ESA SP-702, May 2012, Accessed online on Jun. 2021, URL: http://articles.adsabs.harvard.edu/pdf/2012ESASP.702E..44W

[14] D. Modenini, A. Bahu, A. Curzi and A. Togni, A dynamic testbed for nanosatellites attitude verification. Article. *MDPI, Aerospace*. Year 2020, Vol. 7, Issue 3; DOI:10.3390/aerospace7030031

[15] M. Palmroth, J. Praks, R. Vainio, P. Janhunen, E. K. J. Kilpua, N. Yu. Ganushkina, A. Afanasiev, M. Ala-Lahti, A. Alho, T. Asikainen, E. Asvestari, M. Battarbee, A. Binios, A. Bosser, T. Brito, J. Envall, U. Ganse, H. George, J. Gieseler, S. Good, M. Grandin, S. Haslam, H.-P. Hedman, H. Hietala, N. Jovanovic, S. Kakakhel, M. Kalliokoski, V. V. Kettunen, T. Koskela, E. Lumme, M. Meskanen, D. Morosan, M. Rizwan Mughal, P. Niemelä, S. Nyman, P. Oleynik, A. Osmane, E. Palmerio, Y. Pfau-Kempf, J. Peltonen, J. Plosila, J. Polkko, S. Poluianov, J. Pomoell, D. Price, A. Punkkinen, R. Punkkinen, B. Riwanto, L. Salomaa, A. Slavinskis, T. Säntti, J. Tammi, H. Tenhunen, P. Toivanen, J. Tuominen, L. Turc, E. Valtonen, P. Virtanen, T. Westerlund, FORESAIL-1 cubesat mission to measure radiation belt losses and demonstrate de-orbiting Foresail-1. *Journal of Geophysical Research - Space Physics*, May 2019. Accessed online on Jun. 2021, URL: https://arxiv.org/abs/1905.09600

[16] Virtuelle Experimente. Magnetic field of two Helmholtz coils. *from www.virtuelle-experimente.de*. Accessed online on Aug. 2021. URL: https://virtuelle-experimente.de/en/b-feld/b-feld/helmholtzspulenpaar.php

[17] Bartington Instruments, Mag-13 Three-Axis Magnetic Field Sensors. Specification & Information PDF, *from www.bartington.com, Innovation in magnetics*. Accessed online on Sept. 2021, x DS3143/12.

[18] L. Itti, Demo ArUco. Simple demo of ArUco augmented reality markers detection and decoding. *Jevois.org Official Website*. Accessed online in Sep. 2021, URL: http://jevois.org/moddoc/DemoArUco/modinfo.html#: :text=ArUco %20markers%20are%20small%202D,the%20camera's%20field%20of%20view.

[19] P. Corke, Robotics, Vision and Control. Fundamental Algorithms in MATLAB. Second Edition. Chapter 2. *Springer Tracts in Advanced Robotics*. ISSN 1610-7438. DOI: 10.1007/978-3-319-54413-7

[20] F. L. Markley and J. L. Crassidis, Fundamentals of spacecraft attitude determination and control. *Published jointly by Microcosm Press and Springer. Springer New York Heidelberg Dordrecht London*. ISBN 978-1-4939-0802-8 (eBook). DOI: 10.1007/978-1-4939-0802-8

[21] H. Travis, Introduction to satellite attitude control, in book *Advances in Spacecraft Attitude Control*, Jan. 2020, DOI: 10.5772/intechopen.89658

[22] E. A. Bassett, Test and verification of a CubeSat attitude determination and control system in variable magnetic fields. Theses and Dissertations. *Air Force Institute of Technology AFIT Scholar*. Year 2016. URL https://scholar.afit.edu/etd/478

[23] P. West, Fundamentals of machine vision. *Automated Vision Systems, Inc.*, Year 2021. Accessed online on Sept. 2021, URL: https://www.autovis.com/images/pdf/resources/fundamentals-of-machine-vision.pdf

[24] K. Kwon, S. Ready. Practical Guide to Machine Vision Software: An Introduction with LabVIEW. *Wiley-VCH, Verlag GmbH & Co.* Year 2015, Print ISBN: 978-3-527-33756-9.

[25] M. Sonka, V. Hlavac, R. Boyle. Image Processing, Analysis, and Machine Vision. Fourth Edition. *CENGAGE Learning*. WCN:02-200-208. ISBN-13: 978-1-133-59360-7. ISBN-10: 1-133-59360-7.

[26] B. V. K. V. Kumar, A. Mahalanobis and R. D. Juday. Correlation Pattern Recognition. *Cambridge University Press*. Year 2005. Accessed online Aug. 2021, ISBN-13: 978-0-511-13320-6. ISBN-10: 0-511-13320-0. URL: https://www.cambridge.org/9780521571036

[27] NASA CubeSat Launch Initiative. CubeSat 101: basic concepts and processes for first-time CubeSat developers. *National Aeronautics and Space Administration*, Oct. 2017, Accessed online on Sept. 2021, URL: https://www.nasa.gov/sites/default/files/atoms/files/nasa_csli_cubesat_101_508.pdf

[28] J. Elfving. Attitude and orbit control for small satellites. Thesis. *Linköping University (Tekniska Högskolan i Linköping).* Year 2002. Accessed online on Aug. 2021, Reg No: LiTH-ISY-EX-3295-2003 | URL: https://www.diva-portal.org/smash/get/diva2:18731/FULL
TEXT01.pdf

[29] A. Lassakeur. Investigation of the magnetic characteristics of CubeSats and on-orbit determination and mitigation of their dynamic magnetic moment disturbances. Doctoral Thesis. *Surrey Space Centre, Department of Electronic Engineering, Faculty of Engineering and Physical Sciences*, Oct. 2019, DOI: https://doi.org/10.15126/thesis.00853107

[30] B. A. Riwanto, T. tikka, A. Kestilä and J. Praks. Particle swarm optimization with rotation axis fitting for magnetometer calibration. *IEEE Transactions on Aerospace and Electronic Systems.* Apr. 201, Vol. 53, No. 2, School of Electrical Engineering, Aalto University, Espoo. DOI: 10.1109/TAES.2017.2667458

[31] Jevois Inc. Hardware of Jevois-A33 smart camera. Jevois Smart Machine Vision. Powerful Open-Source Machine Vision for Everyone. *from www.jevoisinc.com.* Accessed online on Sep. 2021. URL: https://www.jevoisinc.com/pages/hardware

[32] AVA. ArUco: a minimal library for Augmented Reality applications based on OpenCV. *Aplicaciones de la visión articial.* Accessed online Sept. 2021, URL: http://www.uco.es/investiga/grupos/ava/node/26